

**FACTORS INFLUENCING ELECTROCHEMICAL  
PROPERTIES AND PERFORMANCE OF HYDROCARBON  
BASED IONOMER PEMFC CATALYST LAYERS**

by

Toby Duncan Astill  
B.Sc. (Hons), University of Victoria, 2003

THESIS SUBMITTED IN PARTIAL FULFILLMENT OF  
THE REQUIREMENTS FOR THE DEGREE OF

DOCTOR OF PHILOSOPHY

In the  
Department  
of  
Chemistry

© Toby Astill 2008

SIMON FRASER UNIVERSITY

Fall 2008

All rights reserved. This work may not be  
reproduced in whole or in part, by photocopy  
or other means, without permission of the author.

# APPROVAL

**Name:** Toby Duncan Astill  
**Degree:** Doctor of Philosophy  
**Title of Dissertation:** Factors Influencing Electrochemical Properties of Hydrocarbon-Based PEMFC Catalyst Layers

**Examining Committee:**

**Chair:** Dr. D. J. Voadlo (Associate Professor)

---

**Dr. S. Holdcroft (Professor)**  
Senior Supervisor

---

**Dr. M. Eikerling (Assistant Professor)**  
Committee Member

---

**Dr. G. Leach (Associate Professor)**  
Committee Member

---

**Dr. G. Agnes (Professor)**  
Internal Examiner

---

**Dr. S. Mukerjee (Professor)**  
External Examiner  
Department of Chemistry  
Northeastern University

**Date Defended/Approved:** \_\_\_\_\_

## **ABSTRACT**

This work investigated the properties of catalyst layers for proton exchange membrane fuel cells (PEMFC) that contained sulfonated poly(ether ether ketone) (SPEEK). A series of SPEEK polymers were prepared with varying ion exchange capacity (IEC) to test their oxygen mass transport properties, electrochemical kinetic parameters, proton conductivity, and water sorption characteristics. A simple method to fabricate catalyst layers containing SPEEK and polytetrafluoroethylene (PTFE) was developed. Catalyst layers were analyzed using scanning electron microscopy (SEM), mercury porosimetry and contact angle determination. Electrochemical characterization in an operating fuel cell was performed using current-potential polarization, cyclic voltammetry, and electrochemical impedance spectroscopy.

Electrochemical oxygen reduction in SPEEK membranes was examined in a solid-state electrochemical cell, which allowed determination of oxygen mass transport properties and kinetic parameters. The oxygen diffusion coefficient and permeability was found to increase with increasing ion exchange capacity (IEC), while the solubility of oxygen correspondingly decreased, these trends are due to an increase in water content with increasing IEC. In comparison to perfluorinated electrolytes, such as Nafion<sup>®</sup>, SPEEK exhibited a lower permeability of oxygen due to a considerably lower solubility of oxygen.

A decrease in fuel cell performance was observed when SPEEK was employed in the cathode catalyst layer as the proton conducting medium. The fuel cell current density showed a strong dependence on the method of fabrication of the catalyst layer and the content of SPEEK. Compared to Nafion<sup>®</sup>-based catalyst layers, SPEEK catalyst layers were found to suffer from low electrochemically active surface area (ESA) and low ionic conductivity. The weight content of SPEEK electrolyte was found to strongly influence the mass transport limited current density.

## DEDICATION

This is for my family.

Who were always there for guidance and support.

Invaluable components towards completion of this degree.

And for them, I am truly grateful.

## **ACKNOWLEDGEMENTS**

I would like to thank my senior supervisor Prof. S. Holdcroft for supervision, support, and guidance at Simon Fraser University. I also extend my thanks and gratitude to my supervisory committee members, Prof. G. Leach and Prof. M. Eikerling for supervising and reviewing this thesis.

My gratitude and appreciation are extended to the following people for their support:

Members of the MEA team of the Institute for Fuel Cell Innovation, National Research Council, Drs. Z. Xie, T. Navessin, K. Shi, J. Peron, M. Secanell, and Mr. Jonathan Martin, for technical guidance and friendship during this joint SFU-NRC collaborative research project.

My proof readers Miss. M. Cavallin, Dr. J. Schmeisser and Dr. J. Peron for their timely and constructive criticisms.

Past and present members of the Holdcroft group for their valuable friendship, useful discussions and support throughout my time at SFU.

The Institute for Fuel Cell Innovation, National Research Council and Simon Fraser University for financial support.

# TABLE OF CONTENTS

<b>Approval</b> .....	<b>ii</b>
<b>Abstract</b> .....	<b>iii</b>
<b>Dedication</b> .....	<b>v</b>
<b>Acknowledgements</b> .....	<b>vi</b>
<b>Table of Contents</b> .....	<b>vii</b>
<b>List of Figures</b> .....	<b>x</b>
<b>List of Tables</b> .....	<b>xv</b>
<b>List of Abbreviations</b> .....	<b>xvi</b>
<b>List of symbols</b> .....	<b>xviii</b>
<b>Chapter 1: Introduction</b> .....	<b>1</b>
1.1 Fuel Cell Technology.....	1
1.2 The Oxygen Reduction Reaction.....	8
1.2.1 Introduction .....	8
1.2.2 The Mechanism of Oxygen Reduction on Pt.....	9
1.3 Proton Exchange Membrane Fuel Cells.....	10
1.3.1 Proton Exchange Membranes.....	10
1.3.2 Hydrocarbon-Based Proton Exchange Membranes.....	16
1.4 Catalyst Layers for Proton Exchange Membrane Fuel Cells .....	20
1.4.1 Activity Benchmarks for Pt and Pt-Alloy Catalysts .....	22
1.4.2 Non-Nafion <sup>®</sup> -Based Catalyst Layers .....	23
1.5 Physical Experimental and Electrochemical Theory Relevant to Fuel Cell Catalyst Layer Analysis.....	26
1.5.1 Physical Experimental Techniques .....	26
1.5.2 Electrochemical Techniques .....	30
1.6 Thesis Structure .....	38
<b>Chapter 2: Electrochemical Reduction of Oxygen at Pt   Nafion<sup>®</sup> 117 and SPEEK Interfaces</b> .....	<b>42</b>
2.1 Introduction.....	42
2.2 Experimental .....	45
2.2.1 Materials .....	45
2.2.2 Sulfonation of Poly(Ether Ether Ketone) .....	46
2.2.3 Preparation of Sulfonated Poly(Ether Ether Ketone) Membranes.....	47
2.2.4 Determination of Ion Exchange Capacity .....	47
2.2.5 Water Content of SPEEK Membranes .....	48

2.2.6 Proton Conductivity .....	49
2.2.7 Solid-State Electrochemistry .....	51
2.3 Results and Discussion .....	55
2.3.1 Preparation and Physical Characterization of SPEEK .....	55
2.3.2 Cyclic Voltammetry at the Pt   Ionomer Interface under N <sub>2</sub> and O <sub>2</sub> Environments .....	58
2.3.3 O <sub>2</sub> Mass Transport Parameters for Nafion <sup>®</sup> 117 and SPEEK possessing different IECs .....	63
2.3.4 O <sub>2</sub> Mass Transport Parameters for Nafion <sup>®</sup> 117 and SPEEK 1.88 as a Function of Temperature .....	70
2.3.5 Evaluation of ORR Kinetics at Pt   Nafion <sup>®</sup> 117 and Pt   SPEEK 1.88 interfaces as a Function of Temperature .....	74
2.4 Conclusion.....	83
<b>Chapter 3: Microstructural Analysis of Nafion<sup>®</sup>- and SPEEK-based Catalyst Layers .....</b>	<b>85</b>
3.1 Introduction.....	85
3.2 Experimental .....	88
3.2.1 Materials .....	88
3.2.2 Scanning Electron Microscopy .....	88
3.2.3 Mercury Porosimetry .....	89
3.2.4 Contact Angle Measurements.....	89
3.2.5 Fabrication of Nafion <sup>®</sup> - and SPEEK-based Catalyst Layers.....	90
3.3 Results and Discussion .....	95
3.3.1 Scanning Electron Microscopy (SEM).....	95
3.3.2 Mercury Porosimetry .....	99
3.3.3 Hydrophobic/Hydrophilic Character of SPEEK-based Catalyst Layers .....	104
3.4 Conclusion.....	105
<b>Chapter 4: Electrochemical Characterization of SPEEK-Based Catalyst Layers .....</b>	<b>107</b>
4.1 Introduction.....	107
4.2 Experimental .....	108
4.2.1 Materials .....	108
4.2.2 Fabrication of Membrane Electrode Assemblies.....	108
4.2.3 Fuel Cell Single Cell Operating Conditions .....	108
4.2.4 Fuel Cell Electrochemical Experiments.....	109
4.3 Results and Discussion .....	111
4.3.1 Electrochemical Characterization of SPEEK-based Catalyst Layers .....	111
4.3.2 Electrochemical Surface Area of SPEEK-based Catalyst Layers .....	113
4.3.3 Electrochemical Influence from PTFE in Catalyst Layer .....	118
4.3.4 Influence of Solvents/Dispersion Media on ESA .....	119
4.3.5 Influence of Cathode Operating Environment.....	123
4.3.6 Proton Conductivity of Nafion <sup>®</sup> - and SPEEK-based Catalyst Layers .....	126

4.3.7 Electrochemical Characterization of Varying Content SPEEK- based Catalyst Layers .....	129
4.4 Conclusion.....	141
<b>Chapter 5: Conclusion and Future Work.....</b>	<b>143</b>
<b>References .....</b>	<b>148</b>

## LIST OF FIGURES

Figure 1.1: Schematic of a proton exchange membrane fuel cell (PEMFC). .....	2
Figure 1.2: Graph showing typical sources of voltage loss (polarization) for a H <sub>2</sub> /O <sub>2</sub> fuel cell. ....	6
Figure 1.3: Chemical structure of Nafion <sup>®</sup> : x = 6-10; y = 1.(4) .....	12
Figure 1.4: Phase separated morphology of hydrated Nafion <sup>®</sup> membrane. Reprinted from ref. (30). Copyright (2001), with permission from Elsevier.....	13
Figure 1.5: Mechanism of proton transport in PEMs: (A) the vehicle mechanism, (B) the Grotthuss mechanism. Reprinted from ref. (33). Copyright (2006), with permission from Elsevier. ....	14
Figure 1.6: Examples of hydrocarbon solid polymer electrolyte membranes. (A) SPEEK(39) (B) SPSS(42) (C) SPES(42, 43) (D) PBI(44). ....	17
Figure 1.7: Chemical structure of Poly(arylene ether) ionomer containing sulfofluorenyl groups.(49) .....	19
Figure 1.8: Schematic diagram of a PEM cathode catalyst layer.....	20
Figure 1.9: Force balance at the three-phase contact point according to Young.(76).....	29
Figure 1.10: Transition to spherical diffusion to semi-infinite, linear diffusion for electrolysis at a Pt microelectrode.(7) .....	32
Figure 1.11: Cyclic voltammogram showing adsorption and desorption of protons on Pt in acidic media. Reprinted from ref. (8). Copyright (2007), with permission from Scribner Associates Inc. ....	34
Figure 1.12: Randles equivalent circuit with mixed kinetic and charge transfer control in a fuel cell.(7) .....	37
Figure 1.13: A one-dimensional transmission line equivalent circuit. The elementary unit comprising protonic resistivity R <sub>p</sub> , charge transfer resistivity R <sub>CT</sub> , double layer capacitance C <sub>dl</sub> , and electronic resistivity R <sub>el</sub> is highlighted. Reprinted from ref. (85). Copyright (1999), with permission from Elsevier. ....	37
Figure 2.1: Synthetic scheme for sulfonated poly(ether ether ketone) polymer.....	46

Figure 2.2: Sulfonated poly(ether ether ketone) in solid (A), solution (DMAc) (B) and MEA (C) form.....	47
Figure 2.3: Schematic drawing of the two-probe cell used for measuring proton conductivity.(100) .....	50
Figure 2.4: A typical Nyquist impedance plot from which proton conductivity data is calculated. Inset: Equivalent circuit used for fitting. $R_m$ , $C_M$ represent the protonic resistance and capacitance of the membrane, respectively.(101) .....	50
Figure 2.5: Schematic diagram (A) and apparatus (B) of the solid-state cell constructed for electrochemical characterization of proton exchange membranes. Working, counter and reference electrodes are denoted: W.E., C.E. and R.E., respectively.(77) .....	52
Figure 2.6: Cyclic voltammogram of Pt   SPEEK in solid-state cell under nitrogen, 100 % relative humidity, 303 K and 30 psi.....	59
Figure 2.7: Cyclic voltammograms for oxygen reduction at a Pt   SPEEK 1.88 membrane interface at 303 K, 100% RH and 30 psi oxygen at 50 mV s <sup>-1</sup> (solid) and 5 mV s <sup>-1</sup> scan rate (dashed).....	62
Figure 2.8: Slow-Sweep voltammetry of Nafion <sup>®</sup> 117 and SPEEK at 303 K, 30 psi oxygen and 100% RH. Nafion 117 (○), SPEEK 1.02 (▲), SPEEK 1.55 (■), and SPEEK 1.88 (●).....	64
Figure 2.9: Chronoamperograms for O <sub>2</sub> reduction at a Pt   SPEEK membrane interface for SPEEK 1.02 (solid), SPEEK 1.55(dashed), and SPEEK 1.88 (dotted) at 303 K, 30 psi oxygen and 100% RH. ....	65
Figure 2.10: Plots of $I$ vs. $t^{-1/2}$ for a chronoamperometric step from 1.2 to 0.4 V for SPEEK 1.02 (solid), SPEEK 1.55 (dashed), and SPEEK 1.88 (dotted) at 303 K, 30 psi oxygen and 100% RH.....	65
Figure 2.11: Oxygen diffusion coefficient for Nafion <sup>®</sup> and SPEEK membranes as a function of IEC at 303 K, 30 psi oxygen and 100% RH. ....	67
Figure 2.12: Oxygen solubility for Nafion <sup>®</sup> and SPEEK membranes as a function of IEC at 303 K, 30 psi oxygen and 100% RH. ....	68
Figure 2.13: Oxygen permeability for Nafion <sup>®</sup> and SPEEK membranes as a function of IEC at 303 K, 30 psi oxygen and 100 % RH. ....	68
Figure 2.14: Linear plots of $I$ vs. $t^{-1/2}$ for a chronoamperometric step from 1.2 to 0.4 V for Pt   Nafion <sup>®</sup> 117 between 0.5 and 5 s at different temperatures (303 – 323 K), 30 psi oxygen and 100% RH. ....	71
Figure 2.15: Linear plots of $I$ vs. $t^{-1/2}$ for a chronoamperometric step from 1.2 to 0.4 V for Pt   SPEEK 1.88 between 0.5 and 5 s at different temperatures (303 – 323 K), 30 psi oxygen and 100% RH. ....	72

Figure 2.16: Slow-sweep voltammograms for O <sub>2</sub> reduction at the Pt Nafion <sup>®</sup> 117 for the temperature range 303–323 K, 30 psi O <sub>2</sub> , and a scan rate of 5 mV s <sup>-1</sup> .....	75
Figure 2.17: Slow-sweep voltammograms for O <sub>2</sub> reduction at the Pt SPEEK 1.88 for the temperature range 303–323 K, 30 psi O <sub>2</sub> , and a scan rate of 5 mV s <sup>-1</sup> .....	75
Figure 2.18: Mass-transport corrected Tafel plots for Nafion <sup>®</sup> 117 for the temperature range 303 – 323 K. 30 psi O <sub>2</sub> pressure and 100% RH. ....	77
Figure 2.19: Mass-transport corrected Tafel plots for SPEEK 1.88 for the temperature range 303 – 323 K. 30 psi O <sub>2</sub> pressure and 100% RH. ....	77
Figure 3.1: Outline for Method 1 (A) and Method 2 (B) SPEEK-based catalyst layer fabrication techniques and expected resulting microstructure.....	94
Figure 3.2: SEM image of catalyst layer surface for Nafion_CL (1:1 IPA: H <sub>2</sub> O). Loadings of 0.25 mg cm <sup>-2</sup> Pt/C and 30 wt% ionomer.....	96
Figure 3.3: SEM image of catalyst layer surface for SPEEK_CL1 (100 % DMAc). Loadings of 0.25 mg cm <sup>-2</sup> Pt/C, 10 wt% PTFE and 10 wt% ionomer.....	96
Figure 3.4: SEM image of catalyst layer surface for SPEEK_CL2 (100 % DMAc). Loadings of 0.25 mg cm <sup>-2</sup> Pt/C, 10 wt% PTFE and 10 wt% ionomer.....	97
Figure 3.5: SEM image of catalyst layer surface for SPEEK_CL1 (DMAc:IPA:H <sub>2</sub> O (1:5:5)). Loadings of 0.25 mg cm <sup>-2</sup> Pt/C, 10 wt% PTFE and 10 wt% ionomer.....	98
Figure 3.6: SEM image of catalyst layer surface for SPEEK_CL2 (DMAc:IPA:H <sub>2</sub> O (1:5:5)). Loadings of 0.25 mg cm <sup>-2</sup> Pt/C, 10 wt% PTFE and 10 wt% ionomer.....	99
Figure 3.7: Catalyst layer pore size distribution, normalized to catalyst layer mass content for Nafion_CL (-▲-)(1:1 IPA: H <sub>2</sub> O), SPEEK_CL1(-○-), and SPEEK_CL2(-●-) (1:5:5 DMAc:IPA:H <sub>2</sub> O). ....	100
Figure 3.8: Catalyst layer pore size distribution, normalized to catalyst layer content, for SPEEK_CL1. 100 % DMAc (-●-) and 1:5:5 DMAc: IPA: H <sub>2</sub> O(-□-) solvent system.....	101
Figure 3.9: Contact angle of D.I. water droplet on SPEEK_CL1 (A) and SPEEK_CL2 (B) surfaces.....	105
Figure 4.1: Teledyne Technologies Inc. 5cm <sup>2</sup> single cell fixture used for fuel cell experiments.....	109

Figure 4.2: Polarization performance (closed) and high frequency resistance (HFR) (open) for Nafion_CL, SPEEK_CL1 and SPEEK_CL2 MEAs. 50 °C cell, 0.2 L/min H <sub>2</sub> /O <sub>2</sub> humidified gases, and atmospheric pressure.....	112
Figure 4.3: Typical EIS Nyquist response for SPEEK_CL1 cathode at increasing current density: 0.50 A, 1.0 A, 1.5 A, and 2.0 A. H <sub>2</sub> /O <sub>2</sub> , 100 % RH, 0.2 L min <sup>-1</sup> and 50 °C cell temperature. ....	112
Figure 4.4: Cyclic voltammograms for Nafion_CL (dash), SPEEK_CL1 (short dash) and SPEEK_CL2 (solid). 50 °C, N <sub>2</sub> /H <sub>2</sub> 0/0.2 L min <sup>-1</sup> , and potential window of 0.04 – 0.9 V at scan rate of 20 mV s <sup>-1</sup> .....	114
4.5: Polarization performance for Nafion_CL, SPEEK_CL1 and SPEEK_CL2 MEAs normalized by the electronically active surface area for each catalyst layer. 50 °C cell, 0.2 L/min H <sub>2</sub> /O <sub>2</sub> humidified gases, and atmospheric pressure. ....	116
Figure 4.6: Cyclic voltammograms of Nafion_CL with 0 wt% (solid), 15 wt% (dashed), and 30 wt% (dotted) SPEEK. 50 °C, N <sub>2</sub> /H <sub>2</sub> gases, 100 % RH, scan rate 20 mV s <sup>-1</sup> , and Potential window 0.04 – 0.9 V. The Nafion <sup>®</sup> content was 30 wt%. ....	117
Figure 4.7: Cyclic voltammograms of SPEEK_CL2 with PTFE (dashed) and without PTFE (solid). 50 °C cell temperature, N <sub>2</sub> /H <sub>2</sub> 0/0.2 L min <sup>-1</sup> , 100 % RH, scan rate 20 mV s <sup>-1</sup> , and potential window 0.04 – 0.9 V. ....	119
Figure 4.8: Cyclic voltammograms of Nafion_CL prepared with (solid) without DMAc solvent (dashed) . 50 °C cell temperature, N <sub>2</sub> /H <sub>2</sub> stream, scan rate 20 mV s <sup>-1</sup> , and potential window 0.04 – 0.9 V. ....	120
Figure 4.9: Cyclic voltammograms of a 100 μm Pt electrode in 1.0 M H <sub>2</sub> SO <sub>4</sub> electrolyte containing DMAc concentrations of 1% (solid), 10% (short dash) and 30% (long dash), scan rate of 50 mV s <sup>-1</sup> . ....	122
Figure 4.10: Cyclic voltammograms of 100 μm Pt bare electrode bare (dashed) and SPEEK covered (solid). 1.0M H <sub>2</sub> SO <sub>4</sub> electrolyte, scan rate of 50 mV s <sup>-1</sup> .....	123
Figure 4.11: Cyclic voltammograms of Nafion_CL cathode under humidified N <sub>2</sub> (solid) and H <sub>2</sub> O (dashed) environments. 50 °C cell temperature, potential window 0.04 – 0.9 V, scan rate, 50 mV s <sup>-1</sup> .....	124
Figure 4.12: Cyclic voltammograms of SPEEK_CL1 cathode in humidified N <sub>2</sub> (solid) and H <sub>2</sub> O (dashed) environments. 50 °C cell temperature, potential window 0.04 – 0.9 V, scan rate, 50 mV s <sup>-1</sup> .....	124
Figure 4.13: Nyquist EIS Response from 10 KHz - 0.1 Hz for Nafion_CL, SPEEK_CL1, and SPEEK_CL2 at 0.45 V under N <sub>2</sub> . High frequency intercept region shown in inset. 50°C cell, H <sub>2</sub> /N <sub>2</sub> 100 % RH, and ambient pressure.....	126

Figure 4.14: Modulus of the impedance vs. $\omega^{-1/2}$ , taken from high frequency (10 K – 1 K Hz), for Nafion_CL, SPEEK_CL1 and SPEEK_CL2.....	127
Figure 4.15: 5 cm <sup>2</sup> polarization performance for SPEEK_CL1 cathodes with ionomer content of 10 (●), 20 (▲), 30 (■) and 40 (▼) wt%. 50 °C cell, 0.2 L/min H <sub>2</sub> /O <sub>2</sub> 100 % RH, and atmospheric pressure. ....	130
Figure 4.16: Cyclic voltammograms of SPEEK_CL1 with electrolyte content of 10 (short dash), 20 (dotted), 30 (long dash) and 40 (solid) wt% SPEEK. 50 °C cell temperature, N <sub>2</sub> /H <sub>2</sub> 0/ 0.2 L min <sup>-1</sup> 100 % RH, scan rate 50 mV s <sup>-1</sup> , and a potential window 0.04 – 0.9 V vs. SHE. ....	131
Figure 4.17: Compositional analysis for Nafion_CL and increasing ionomer content SPEEK_CL1. ....	136
Figure 4.18: EIS Nyquist response for SPEEK_CL1 catalyst layer 10 wt% SPEEK, at increasing cell current (A). H <sub>2</sub> /O <sub>2</sub> at 0.2 L min <sup>-1</sup> and 50 °C cell temperature. ....	139
Figure 4.19: Variance of total ionic and electronic resistance in the cathode determined from EIS data for SPEEK_CL1 with 10 (■), 20 (▲), 30 (▼), and 40 (●) weight percent SPEEK. ....	140

## LIST OF TABLES

Table 1.1: Impedance relationships of ideal electrical circuit elements commonly used to describe the impedance responses of fuel cells.(7, 8) .....	36
Table 2.1: Ion exchange capacity, water content, and proton conductivity for Nafion <sup>®</sup> and SPEEK membranes. ....	57
Table 2.2: Geometric area, real area and roughness factor for the solid-state Pt microelectrode   Ionomer interface.....	61
Table 2.3: Oxygen mass transport parameters for Nafion <sup>®</sup> 117 and SPEEK ionomers of varying IEC from chronoamperometry at 303 K, 100 % RH and 30 psi oxygen.....	66
Table 2.4: Mass transport parameters for Nafion <sup>®</sup> 117 and SPEEK 1.88 for the temperature range 303–323 K, 100 % RH and 30 psi oxygen.....	73
Table 2.5: Electrode kinetic parameters for Nafion <sup>®</sup> 117 and SPEEK 1.88 interfaces as a function of temperature 303–323 K, 100 % RH, and 30 psi O <sub>2</sub> .....	81
Table 3.1: Solvent/Dispersion medium, electrolyte content, and peak pore size for Nafion_CL, SPEEK_CL1 and SPEEK_CL2. ....	102
Table 4.1: Electrochemical surface area for Nafion_CL, SPEEK_CL1 and SPEEK_CL2. 50 °C cell temperature, 0.2 L min <sup>-1</sup> H <sub>2</sub> /N <sub>2</sub> , 100 % RH, and atmospheric pressure. ....	114
Table 4.2: Electrochemical Surface Area for 30 wt% Nafion <sup>®</sup> catalyst layer containing varying content of SPEEK. 50 °C cell temperature, 0.2 L min <sup>-1</sup> H <sub>2</sub> /N <sub>2</sub> , and ambient pressure. ....	118
Table 4.3: Double layer capacitance, proton resistance and ionic conductivity for Nafion_CL, SPEEK_CL1 and SPEEK_CL2 catalyst layers.....	128
Table 4.4: Double layer capacitance charge, ESA, CL proton resistance, and CL conductivity for SPEEK_CL1 containing increasing SPEEK weight content. ....	132
Table 4.5: CL conductivity normalized to volume fraction of electrolyte in each SPEEK_CL1, and comparison to bulk SPEEK electrolyte conductivity.....	133

## LIST OF ABBREVIATIONS

AC	Alternating Current
CL	Catalyst Layer
CV	Cyclic Voltammetry
D.I.	De-Ionized Water
DMAc	Dimethyl Acetamide
DMFC	Direct Methanol Fuel Cell
DS	Degree of Sulfonation
$E^{\circ}_{\text{theor}}$	Theoretical Cell Voltage at standard conditions
$E^{\circ}$	Equilibrium Cell Potential
ETFE	Ethylene Tetrafluoroethylene
EMF	Electromotive Force
ESA	Electrochemically Active Surface Area
EIS	Electrochemical Impedance Spectroscopy
EW	Equivalent Weight
GDE	Gas Diffusion Electrode
GDL	Gas Diffusion Layer
IV	Current-Voltage Polarization
IEC	Ion Exchange Capacity
IPA	Isopropyl Alcohol

MEA	Membrane Electrode Assembly
N117, N115	Nafion <sup>®</sup> 117, Nafion <sup>®</sup> 115
ORR	Oxygen Reduction Reaction
PE	Polyethylene
PBI	Polybenzimidazole
PEM	Proton Exchange Membrane
PEMFC	Proton Exchange Membrane Fuel Cell
PTFE	Polytetrafluoroethylene
RH	Relative Humidity
RDS	Rate Determining Step
SEM	Scanning Electron Microscopy
SPAES	Sulfonated Poly(Arylene Ether Sulfone)
SPES	Sulfonated Poly(Ether Sulfone)
SPEEK	Sulfonated Poly(Ether Ether Ketone)
SPEKK	Sulfonated Poly(Ether Ketone Ketone)
SPSU	Sulfonated Polysulfone
SPSS	Sulfonated Polysulfide Sulfone

## LIST OF SYMBOLS

### Symbols

$c_b$	Oxygen solubility, mol l <sup>-1</sup>
$C_o, C_R$	Concentration of oxidized and reduced species
$D_b$	Diffusion coefficient of oxygen
$D$	Pore diameter
$i_o$	Exchange current, A
$H$	Henry's constant for O <sub>2</sub>
$F$	Faraday's constant, 96,485 C mole <sup>-1</sup>
$k_o$	Standard intrinsic rate constant
$L$	Thickness
$j_o$	Exchange current density, A cm <sup>-2</sup>
$r$	radius
$R$	Gas constant, 8.3145 J mol <sup>-1</sup> K <sup>-1</sup>
$T$	Temperature
$V$	Volume fraction

### Greek

$\alpha$	Transfer coefficient
$\eta$	overpotential

$p_{H_2}, p_{H_2O}, p_{O_2}$	Partial pressure: H <sub>2</sub> , H <sub>2</sub> O and O <sub>2</sub>
$\sigma_{H^+}$	Proton conductivity, S cm <sup>-1</sup>
$\sigma_{lv}$	Liquid interfacial tension
$\sigma_{Hg}$	Surface tension
$\delta$	Thickness of the mass transport boundary layer
$\Theta$	Contact angle
$\theta_{Hg}$	Contact angle between the mercury and the sample
$\varnothing$	Diameter

# CHAPTER 1: INTRODUCTION

## 1.1 Fuel Cell Technology

Fuel cells are electrochemical energy conversion devices that produce electricity from the chemical energy of fuels, with water and heat as by-products. Unlike a battery, a fuel cell will continue to operate as long as fuel is fed to the cell. Fuel cells offer advantages of high power density, low environmental impact, low noise pollution and low operating temperature, while still being configurable for many applications.(1, 2)

Sir William Robert Grove pioneered studies in fuel cells in the middle of the 19th century by combining hydrogen and oxygen to produce electricity and water. Fuel cells however, did not find their first application until the 1960s when an alkaline fuel cell was used to power the electrical system of NASA's Gemini second human spaceflight.(3) Since then, the study of fuel cells has undergone several cycles of intense activity.

Fuel cells are distinguished by the electrolyte incorporated, and include alkaline, proton exchange membrane, phosphoric acid, solid oxide, and molten carbonate media. During the last two decades, a confluence of driving forces have created a sustained and significant worldwide effort to develop fuel cell materials and fuel cell systems. These systems are intended for transport, stationary and portable energy applications. In transportation applications, for example, the demand for efficient energy systems with reduced CO<sub>2</sub> emissions

and high energy density have led to rapid development of proton exchange membrane fuel cells (PEMFCs).(3, 4) **Figure 1.1** illustrates the operation of a proton exchange membrane fuel cell, fuelled with hydrogen. PEMFCs capitalize on the essential simplicity of the system, and use a solid polymer to allow the transport of protons from anode to cathode. PEMFCs operate at low temperature (below 100 °C) and generate a specific power ( $\text{W kg}^{-1}$ ) and power density ( $\text{W cm}^{-2}$ ) higher than any other type of fuel cell.(5)

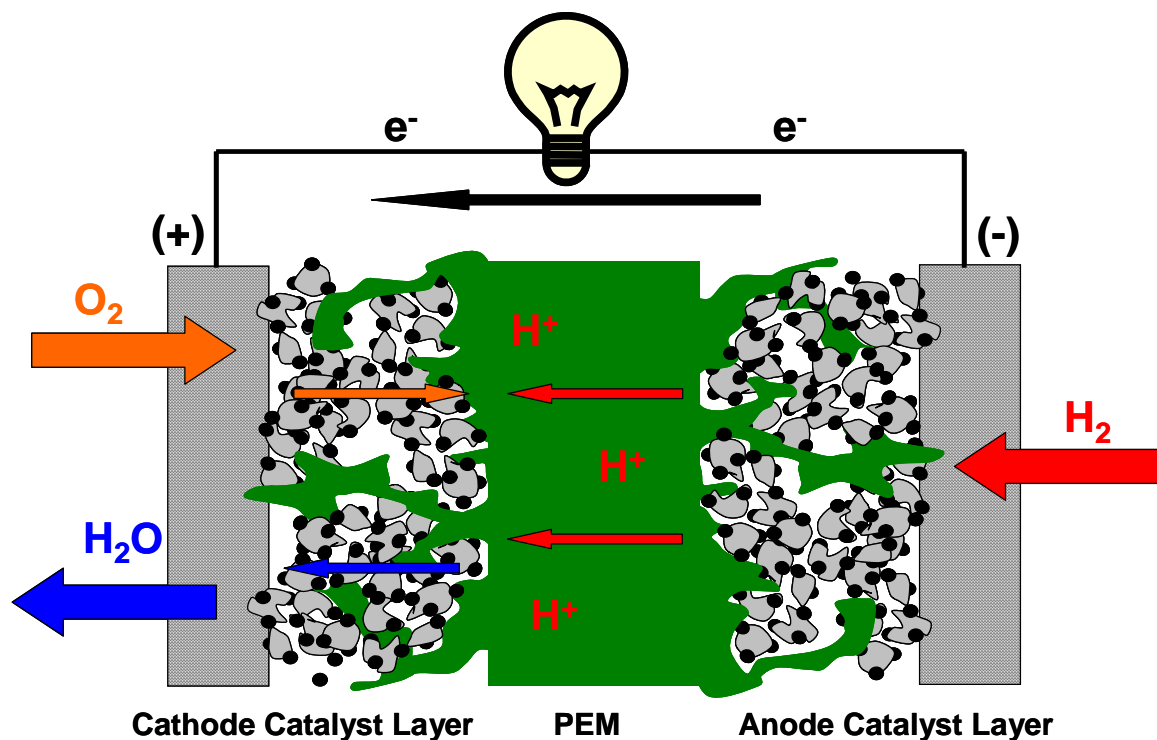


Figure 1.1: Schematic of a proton exchange membrane fuel cell (PEMFC).

Inside the PEMFC, the functionality of each component differs but is tailored to maximize the combined effect of electronic conductivity, protonic conductivity and reactant transport. The proton exchange membrane (PEM) and

the anode and cathode, make up the membrane electrode assembly (MEA). The PEM allows proton transport across the fuel cell and minimizes fuel crossover from anode to cathode. Hydrogen is oxidized at the anode, where protons,  $H^+$ , and electrons,  $e^-$ , are liberated in the hydrogen oxidation reaction (HOR) according to equation 1.1,



At the cathode, oxygen molecules dissociate into atoms. Oxygen atoms combine with protons that have migrated through the PEM electrolyte from the anode and electrons from the external circuit to form water and heat in the oxygen reduction reaction (ORR) shown below in equation 1.2,



The electrochemical oxidation and reduction reactions shown above result in the following overall reaction for a fuel cell.



The theoretical efficiency for the conversion of chemical energy to electrical energy in a hydrogen-oxygen fuel cell depends on the Gibbs free energy of formation,  $\Delta G_f$ , for the reaction. Since the change in Gibbs free energy ( $-237 \text{ kJ mol}^{-1}$ , liq. water,  $25^\circ \text{C}$  (6)) for the above reaction is known, the standard theoretical potential ( $E^\circ$ ) for the  $H_2/O_2$  cell reaction can be calculated from equation 1.4,

$$E^\circ = -\frac{\Delta G_o}{nF}, \quad (1.4)$$

where  $n$  is the number of electrons required to complete the reaction ( $n = 2$  equivalent/ mole  $H_2$ ) and  $F$  is Faraday's constant. Assuming unit activity of all reactants and products, and a temperature of  $25\text{ }^\circ\text{C}$ , the corresponding electromotive force, or  $E^\circ$ , value is  $1.23\text{ V}$ . However, fuel cell operating conditions often employ activities of reactants and/or products that differ from unity. Under these conditions, the Nernst equation can be used to account for the reduced activity of reactants and/or products. The electromotive force for the  $H_2/O_2$  reaction under non-standard conditions, is determined using equation 1.5 below,(7)

$$E_{\text{theor}} = E^\circ_{\text{theor}} + \left(\frac{RT}{nF}\right) \ln\left(\frac{(p_{H_2})(p_{O_2})^{1/2}}{(p_{H_2O})}\right), \quad (1.5)$$

where  $E_{\text{theor}}$  is the equilibrium cell voltage for non-standard concentrations at a temperature  $T$ ,  $E^\circ_{\text{theor}}$  is the equilibrium voltage for standard concentrations as determined from equation 1.4.  $R$  is the gas constant.  $T$  is temperature in degrees Kelvin and  $p_{H_2}$ ,  $p_{O_2}$ ,  $p_{H_2O}$  are the partial pressures of  $H_2$ ,  $O_2$ , and  $H_2O$ , respectively, in units of atmospheres.(8)

When an external resistance or "load" is applied to a fuel cell, non-equilibrium conditions exist and a net current flows through the external load, polarizing the fuel cell. The net rate of the electrochemical reactions occurring is proportional to the current density,  $j$ , which is the current,  $i$ , of the electrochemical system divided by the geometric active area of the MEA. The cell voltage becomes smaller as the current density increases because of irreversible voltage losses. The extent of these losses, or overall polarization, is measured by the

overpotential ( $\eta$ ) shown in equation 1.6 below which is the deviation from the equilibrium potential value,  $E^\circ$ .

$$\eta = E - E^\circ. \quad (1.6)$$

When there are no mass-transfer effects, or the currents are kept low so that the surface concentrations do not differ appreciably from the bulk values, the current-overpotential equation can be expressed by equation 1.7 below,

$$i = i_o [e^{-\alpha f \eta} - e^{(1-\alpha) f \eta}] \quad (1.7)$$

which is historically known as the Butler-Volmer equation, where  $i$  is the current,  $i_o$  is the exchange current,  $\alpha$  is the transfer coefficient,  $f$  is  $F/RT$ , and  $\eta$  is the overpotential.

The current density-voltage curve, or polarization curve, for an operating fuel cell and the factors associated with the irreversible voltage losses when operated with  $H_2/O_2$  is shown in **Figure 1.2**. These irreversible voltage losses are dictated by the cells' geometry, the characteristics of the anode and cathode, the electrolyte/membrane properties and the operating conditions (gas concentration, flow rate, back pressure, temperature, and relative humidity). These losses combine to make up the kinetic activation resistance, Ohmic resistance, and mass transport resistance.

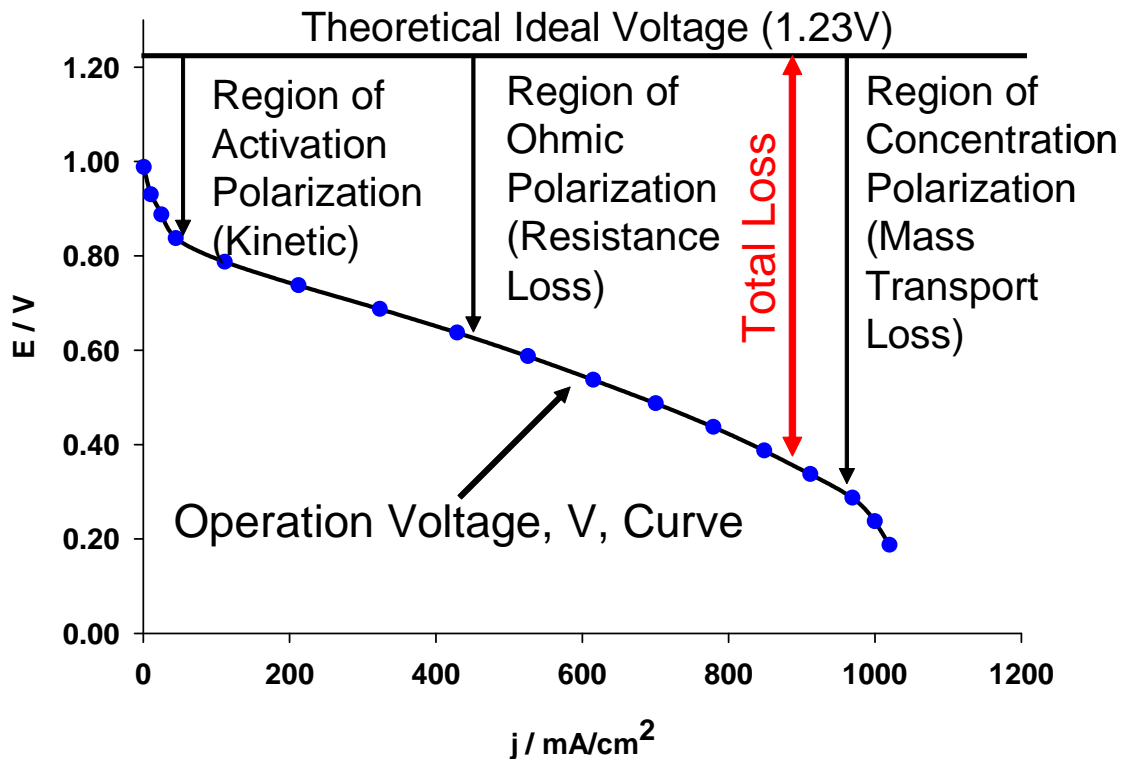


Figure 1.2: Graph showing typical sources of voltage loss (polarization) for a  $\text{H}_2/\text{O}_2$  fuel cell.

At low current densities ( $< 100 \text{ mA cm}^{-2}$ ), activation polarization losses,  $\eta_{\text{act}}$ , dominate the overpotential. Activation losses are caused by the sluggishness of the electrochemical reactions on the electrodes where the overpotential is required to drive the chemical reaction. Kinetic losses can be evaluated by measuring the exchange current,  $i_o$ . The exchange current is determined at equilibrium potential where the net current flow is zero and is described by equation 1.8,(7)

$$i_o = nFAk^o C_O^{(1-\alpha)} C_R^\alpha. \quad (1.8)$$

where  $A$  is the geometric area of the electrode ( $\text{cm}^2$ ),  $k^\circ$  ( $\text{cm s}^{-1}$ ) is the standard intrinsic heterogeneous rate constant when  $C_O = C_R$ .  $C_O$  and  $C_R$  are the concentration of the oxidized and reduced species, and  $\alpha$  is the transfer coefficient ranging between 0 and 1. The transfer coefficient parameter is dimensionless and represents the measure of symmetry of the free-energy barrier for a single step electrochemical process. It is an experimental parameter obtained from the current-potential relationship. If the intersection of the energy profiles is symmetrical,  $\alpha = 1/2$ . In most electrochemical reactions,  $\alpha$  lies between 0.3 and 0.7, but is usually approximated to be 0.5 in the absence of an actual measurement. The exchange current is typically normalized to unit area to provide the exchange current density:  $j_o = i_o/A$ .(7) As will be demonstrated, the activation losses,  $\eta_{\text{act,c}}$ , at the cathode due to the sluggish oxygen reduction reaction (ORR) are much larger than the activation losses found at the anode,  $\eta_{\text{act,a}}$ , where the more facile hydrogen oxidation reaction occurs.(8) Ohmic losses,  $\eta_{\text{ohmic}}$ , observed at moderate current densities in **Figure 1.2** exhibit a linear relationship with current density, and correspond to the resistance of electron and proton flow through the MEA. Finally, mass transport, or concentration losses,  $\eta_{\text{conc}}$ , occur at high current densities and result from depletion of the reactant at the electrode surface. The difference in reactant concentration at the surface produces an irreversible voltage loss. When the concentration reaches zero at the electrode surface, no further increase in current is possible, this is called the limiting current density,  $j_{\text{lim}}$ . The actual cell voltage,  $V_{\text{cell}}$ , at any current density can be quantified by the standard theoretical

potential minus the kinetic activation, Ohmic and mass transport losses, expressed by equation 1.9,(8)

$$V_{\text{cell}} = E_{\text{theor}} - (|\eta_{\text{act,c}}| + |\eta_{\text{act,a}}|) - \eta_{\text{ohmic}} - (|\eta_{\text{conc,c}}| + |\eta_{\text{conc,a}}|). \quad (1.9)$$

## 1.2 The Oxygen Reduction Reaction

### 1.2.1 Introduction

The electrochemical oxygen reduction reaction (ORR) is of great interest in fuel cell research as it is the rate determining reaction in an operating fuel cell. The ORR reaction is sluggish compared to the hydrogen oxidation reaction (HOR). The exchange current densities for the ORR is typically in the range of  $10^{-10}$  A cm<sup>-2</sup>; whereas the HOR is  $10^{-3}$  A cm<sup>-2</sup>. The major contribution to the voltage loss in a fuel cell is the kinetically-limited oxygen reduction reaction.(9-11)

Two physiochemical properties that affect the rate of the oxygen reduction reaction, particularly in the mass-transport limited region, are the solubility and diffusivity of oxygen. These parameters are strongly dependent on temperature, pressure, and electrolyte composition. The magnitude of the solubility and diffusivity of oxygen play a significant role in the limiting current density for ORR, as is evident from Fick's first law shown in equation 1.10,

$$\frac{i_l}{nF} = \frac{Dc_b}{\delta}, \quad (1.10)$$

where  $i_l$  is the limiting current density,  $n$  is the number of electrons transferred per mole,  $F$  is Faraday's constant,  $D$  is the oxygen diffusion coefficient,  $c_b$  is the

solubility of oxygen in the electrolyte, and  $\delta$  is the thickness of the mass transfer boundary layer.

### 1.2.2 The Mechanism of Oxygen Reduction on Pt

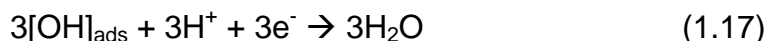
The mechanism of the oxygen reduction reaction is still not fully understood.(9, 10, 12) ORR may occur via one of two pathways: a “direct” 4-electron reduction (equation 1.11) and a “peroxide” pathway (equation 1.12, 1.13 and 1.14), which involves  $\text{H}_2\text{O}_2$  as an intermediate.(11)



Oxygen reduction on noble metal catalysts (Pt, Pd), such as those used in fuel cells predominately occurs *via* the “direct” 4-electron pathway.(13). Hoare *et al.*(10), Conway *et al.*(14) and Hsueh *et al.*(15) have published extensive surveys on the mechanism of ORR. The multi-electron process is believed to include a number of elementary steps involving various series and parallel pathways. A model proposed by Damjanovic *et al.*(16-18) is consistent with experimental results by Hsueh *et al.*(15). In this model, the first electrochemical step is considered to be a fast, chemical  $\text{O}_2$ -adsorption step providing a partial coverage of the surface. The next step is protonation of adsorbed  $\text{O}_2$  (equation 1.15), and is believed to be the rate-determining step (RDS).(19) The rate limiting step is thus first order with respect to  $\text{O}_2$  pressure.



Following the RDS, Antoine *et al.*(19) proposes a mechanism consistent with Damjanovic that involves a chemical step (equation 1.16) and a final electrochemical step (equation 1.17) illustrated below.



This mechanism can be labeled as an ECE mechanism, “E” representing an electron transfer at the electrode surface and “C” representing a homogeneous chemical reaction. In this mechanism, the product of the chemical reaction (equation 1.15) is electroactive and a second electron-transfer reaction (equation 1.15) takes place after the initial RDS electron-transfer reaction.

## 1.3 Proton Exchange Membrane Fuel Cells

### 1.3.1 Proton Exchange Membranes

Since their use in Gemini space missions, proton exchange membrane fuel cells (PEMFC) have piqued considerable research interest within academic and industry environments, and are prominent in the public eye as an attractive eco-friendly energy converter. PEM fuel cells are being developed for three main applications: automotive, stationary, and portable power. While each of these applications requires unique operating conditions and material requirements, all use a solid electrolyte membrane. Additionally, common characteristics critical to all high performance PEMs include: high proton conductivity that allows high current densities without resistive losses; low electronic conductivity to prevent

short circuiting the cell; low permeability to fuel and oxidant to prevent mixed potentials; low water transport through diffusion and electro-osmosis to prevent drying of the anode and flooding of the cathode; oxidative and hydrolytic stability for useful operating lifetimes; good mechanical properties to combat the constantly changing hydration state of the cell and costs suitable for commercialization.(1, 3, 20)

### 1.3.1.1 Perfluorinated Ionomer Membranes

Since the mid-1960s, the material of choice for the proton exchange membrane has been the perfluorosulfonic acid (PFSA) electrolyte, such as that developed by E.I Dupont de Nemours trademarked Nafion<sup>®</sup>.(21) This PEM is based on a solid, hydrated sulfonic acid-containing perfluoropolymer with the general formula shown in **Figure 1.3**. Nafion<sup>®</sup> is a copolymer comprising of a crystallisable hydrophobic tetrafluoroethylene (PTFE) backbone (~87 mol % at 1100 equivalent weight) copolymerized with a monomer bearing a pendant side chain of perfluorinated vinyl ether, terminated by a perfluorosulfonic acid group. The values x and y in the main chain of Nafion<sup>®</sup> can be varied to produce membranes of different equivalent weight (EW), where EW is defined as grams of dry polymer per mole of fixed SO<sub>3</sub><sup>-</sup> sites. Typically, Nafion<sup>®</sup> (used as 1100 EW) provides high protonic conductivity with little swelling in water, with available thicknesses of 2, 5, 7 and 10 mil (*i.e.*, Nafion<sup>®</sup> 112, 115, 117 and 1110).(4) Recently, new variations have become commercially available, labeled as Nafion<sup>®</sup> NRE-211 (1 mil) and NRE-212 (2 mil), respectively, which maintain the

same properties as Nafion<sup>®</sup> 1100 EW but offer enhanced chemical stability with substantially lower fluoride ion release.

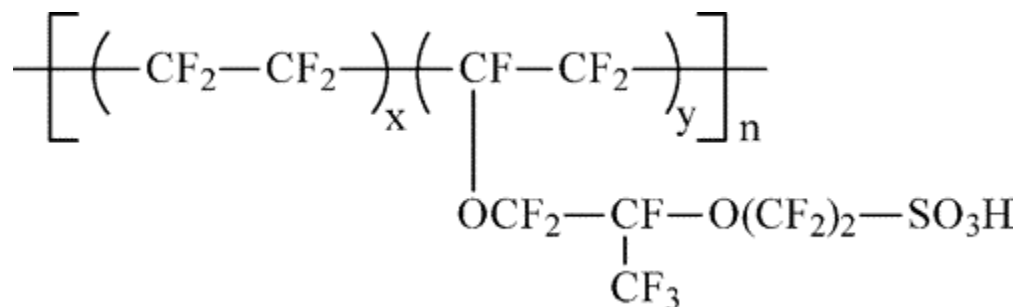


**Figure 1.3: Chemical structure of Nafion<sup>®</sup>: x = 6-10; y = 1.(4)**

Nafion<sup>®</sup> is considered the “industry standard”, and makes up the largest body of literature of all PEMs.(22) Nafion<sup>®</sup> has been shown to have operating lifetimes in excess of 57,000 hours,(23) with proton conductivities in the order of 0.1 S cm<sup>-1</sup> at temperatures below 100 °C.(24) The hydrophobic backbone comprised of strong bonds between carbon and fluorine, resembling polytetrafluoroethylene (PTFE), makes Nafion<sup>®</sup> highly durable and resistant to chemical attack. This chemical structure also provides the hydrophobic character required for effective water management in reducing mass transport limitations and dehydration in fuel cells. Additionally, the sulfonated pendant side chains endow Nafion<sup>®</sup> with electrolytically conductive properties. The presence of a terminal hydrophilic sulfonic acid group, -SO<sub>3</sub>H, provides a source of SO<sub>3</sub><sup>-</sup> and H<sup>+</sup> ions. The strong mutual attraction between positive and negative charges causes the side chains to cluster within the structure of Nafion<sup>®</sup>. The hydrophilic regions around the sulfonated side chains lead to the sorption of

water molecules (up to 50 % of the dry weight of the material). A nano-phase separated morphology results, as shown in **Figure 1.4**, which forms an interpenetrating hydrophobic and hydrophilic network. The hydrophobic region gives the membrane its morphological stability, whereas the hydrated hydrophilic region facilitates the conduction of protons. (22, 25-29)

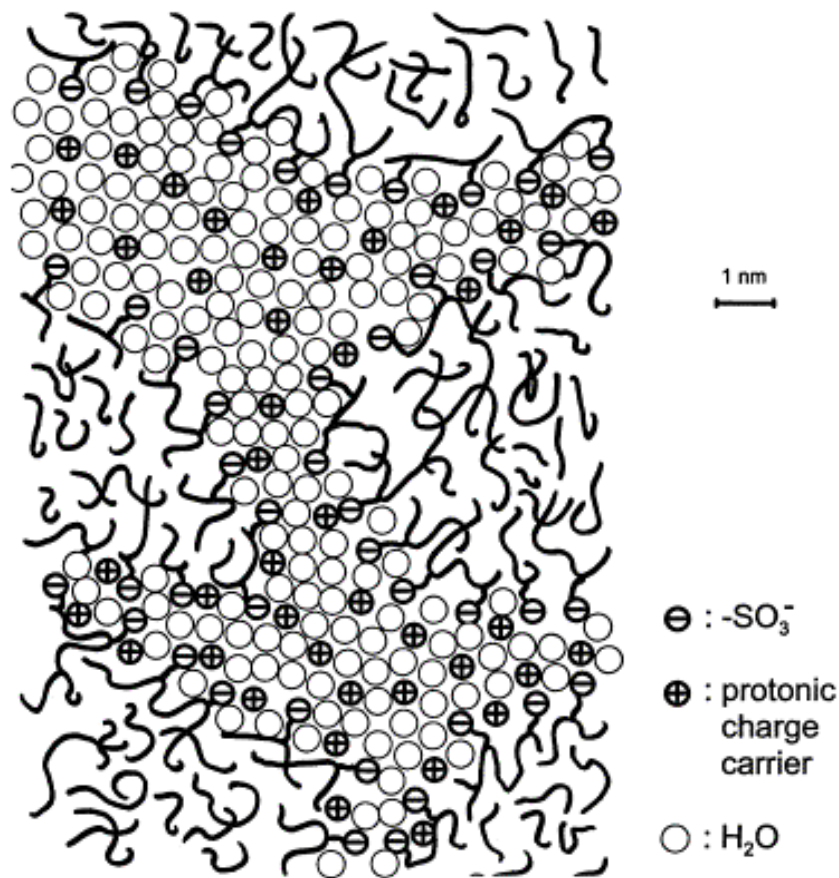


**Figure 1.4:** Phase separated morphology of hydrated Nafion<sup>®</sup> membrane. Reprinted from ref. (30). Copyright (2001), with permission from Elsevier.

### 1.3.1.2 Ionic Conductivity in Proton Exchange Membranes

Within the hydrated hydrophilic regions of Nafion<sup>®</sup>, the pKa of the acid is ~ -6, which facilitates dissociation of H<sup>+</sup> from the SO<sub>3</sub><sup>-</sup> ions and enhances the mobility of the proton.(20, 30, 31) When hydrated, the sulfonic acid groups form a continuous hydrophilic domain, that enable protons to be transported.(25) When an electric field is applied across the membrane, protons migrate due to electromotive forces. Although the mechanism by which the proton is transported is still somewhat controversial, the two mechanisms commonly proposed in the literature are: the vehicular mechanism and the Grotthuss 'hopping' mechanism.(20, 24, 25, 31-33) The difference between the two mechanisms is illustrated in the cartoon below (**Figure 1.5**).

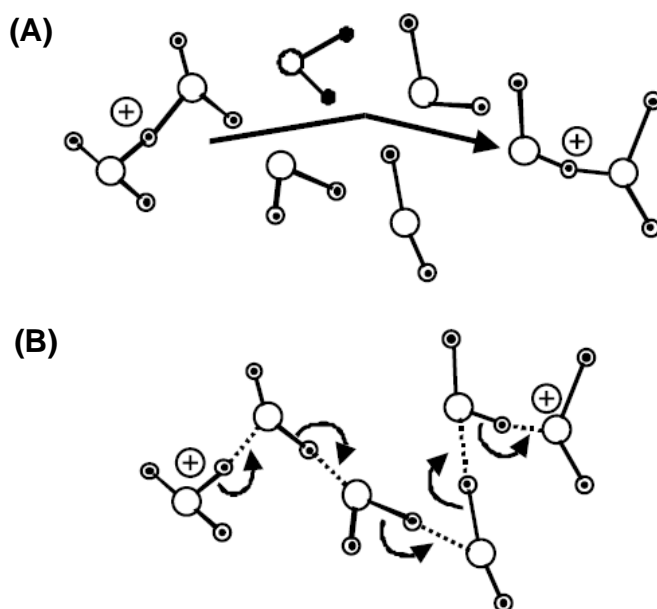


**Figure 1.5: Mechanism of proton transport in PEMs: (A) the vehicle mechanism, (B) the Grotthuss mechanism. Reprinted from ref. (33). Copyright (2006), with permission from Elsevier.**

The vehicular mechanism involved is the movement of the proton with its solvation shell, in a process similar to molecular diffusion.(33) This process can be interpreted as a diffusion process in which the hydrated proton travels through the hydrophilic domain as a single entity. The Grotthus mechanism can be described as proton diffusion or hopping through the hydrogen bonded network of water molecules via the formation and cleavage of H-bonds. These bonds are formed because protons are strongly associated with aggregates of water, idealized by two forms,  $\text{H}_5\text{O}_2^+$  (the Zundel cation) and  $\text{H}_9\text{O}_4^+$  (the Eigen cation).(31)

#### **1.3.1.3 Limitations of Perfluorinated Ionomers**

Although perfluorosulfonic acid membranes show superior performance in fuel cells operating at moderate temperature (<90 °C) and high relative humidity with pure hydrogen as a fuel, their properties are ill-suited at higher temperatures. Currently, the use of hydrogen produced by reforming methanol and gasoline is receiving increasing interest. This is problematic as reformed gases contain trace impurities, particularly CO, which reduce the activity of the Pt catalyst.(25) The CO tolerance, however, increases with increasing temperature, and therefore, fuel cell operation at higher temperature ( > 100 °C) is desirable.(20) Nafion<sup>®</sup> has been shown to suffer from reduced conductivity at higher temperatures and low relative humidity.(30, 34) In the case of direct methanol fuel cells (DMFC), in which hydrogen is replaced with methanol, fuel crossover through the membrane is a significant issue which decreases the performance, reduces fuel efficiency and requires additional water management.

Perfluorosulfonic acid membranes such as Nafion<sup>®</sup> serve as poor barriers to methanol permeation.(20, 35) While Nafion<sup>®</sup> remains the most commonly employed PEM, limitations on operation temperature, methanol cross-over, and its high cost are significant barriers to their use.(30) Alternative PEMs are therefore under intense study, and are discussed in the following sections.

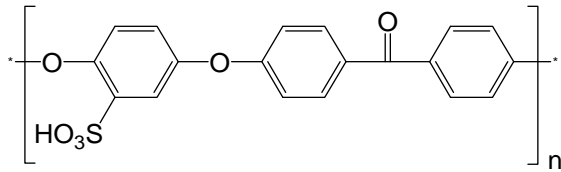
### 1.3.2 Hydrocarbon-Based Proton Exchange Membranes

Work within this class has grown considerably in the last decade. New design approaches undertaken to find alternatives for perfluorosulfonic ionomers employ PEMs based on hydrocarbon membranes. This area of research provides the context for the choice of solid electrolyte studied in this thesis. Previous studies demonstrate that the initial drive by researchers was to produce analogues that mimic the beneficial properties of Nafion<sup>®</sup>; however, it is clear that the distinct chemical and microstructural properties of these hydrocarbon polymers create both varied limitations, and new perspectives.(4, 36, 37)

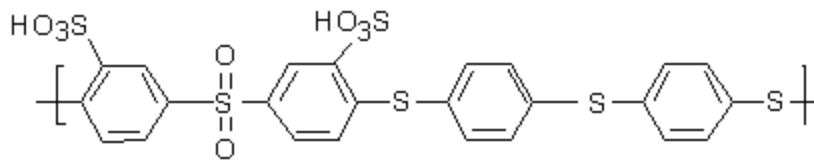
Within this class of solid polymer electrolyte, polyarylene analogues such as sulfonated poly(ether ether ketone) (SPEEK), sulfonated polyether sulfone (SPES), sulfonated polysulfone (sPSU), sulfonated polysulfide sulfone (SPSS), and polybenzimidazole (PBI) have been extensively studied. Examples are shown in **Figure 1.6**.(4, 37-42). Some of these may be suitable for fuel cell PEM applications, with diverse mechanical and electrical properties, long-term stability, high efficiency and potentially lower cost.(20) Evaluation of their stability under oxidizing and reducing conditions at various temperatures (up to 200 °C)

have shown that certain classes of membranes may have suitable durability during fuel cell operation.(36)

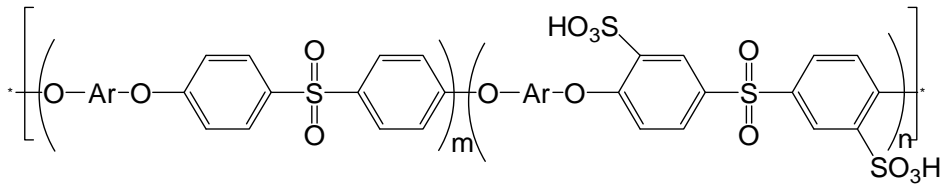
A.



B.



C.



D.

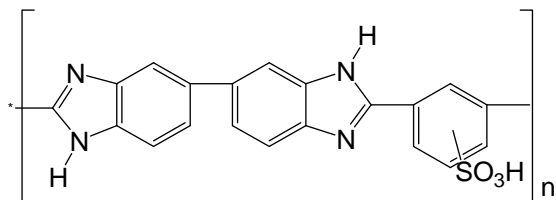


**Figure 1.6: Examples of hydrocarbon solid polymer electrolyte membranes. (A) SPEEK(39) (B) SPSS(42) (C) SPES(42, 43) (D) PBI(44).**

Sulfonated poly (ether ether ketone), SPEEK, depicted in **Figure 1.6A** has been studied extensively, and shown to possess a proton conductivity similar to Nafion<sup>®</sup> ( $0.1 \text{ S cm}^{-2}$ ) when the degree of sulfonation is  $> 50 \%$ .(4, 30, 45, 46) Fuel cell performances comparable to, or exceeding that of Nafion<sup>®</sup>, have been demonstrated for DMFC applications, due to their lower rate of methanol crossover.(47) In addition, SPEEK has been blended with other components, with the goal of improving the mechanical properties, increasing the proton conductivity, and optimizing the swelling of hydrated membranes. Work with polymer blend membranes fabricated with sulfonated poly(ether ether ketone) and poly(sulfone) bearing benzimidazole side groups are reported to exhibit higher proton conductivity and better performance in PEMFCs at  $90 \text{ }^\circ\text{C}$  and  $100 \text{ }^\circ\text{C}$  than SPEEK or Nafion<sup>®</sup> membranes, thus, highlighting the potential benefits of combining differing hydrocarbon ionomers.(38-40, 48)

Sulfonated polysulfone, (sPSU), sulfonated polyether sulfone (SPES), and sulfonated polysulfide sulfone (SPSS), membranes have been studied extensively.(4, 37, 41) The introduction of hydrophilic sites on rigid aryl backbones appears to produce promising electrolyte membranes for fuel cell applications, however, extensive sulfonation leads to disproportional increases in water uptake, ultimately leading to their dissolution.

Sulfonated polybenzimidazole (PBI) membranes have been shown by Jones *et al.*(44) to act as a suitable proton exchange membrane candidate, especially given the success of unmodified PBI/phosphoric acid membranes in high temperature fuel cells. However, these systems display lower degrees of

microphase separation than Nafion<sup>®</sup> as well as a loss of mechanical stability for polymers with high degrees of sulfonation limiting their practicality in hydrated fuel cells.

Typically, polyarylenes display less phase separation and have narrower ionic channels than Nafion<sup>®</sup>.(38, 39, 48) Nevertheless, selected hydrocarbon-based membranes have been examined in fuel cells. For example Fu *et al.*(48) reported current/voltage characteristics comparable to Nafion<sup>®</sup> for a sulfonated poly(ether ether ketone) and also a polysulfone bearing benzimidazole side groups. Aoki *et al.*(49) investigated the operational durability of polyarylene ionomers containing sulfofluorenyl groups, illustrated below in **Figure 1.7**, in single cell tests at 80 °C and at a constant current density of 0.2 A cm<sup>-2</sup>. Under 90 % RH operation, polyarylene ionomers containing sulfofluorenyl groups exhibit good hydrolytic stability even after 5000 h of operation with no noticeable degradation in cell performances, ion exchange capacity, thickness, or molecular weight.

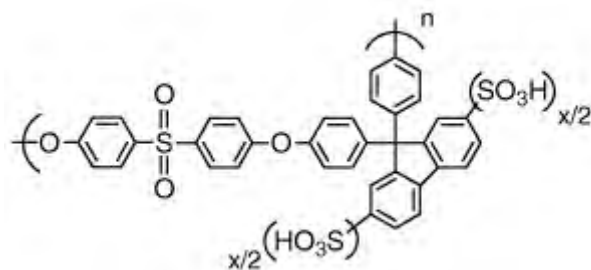


**Figure 1.7: Chemical structure of Poly(arylene ether) ionomer containing sulfofluorenyl groups.(49)**

## 1.4 Catalyst Layers for Proton Exchange Membrane Fuel Cells

The gas diffusion electrodes (GDEs) situated on each side of the proton exchange membrane support the catalyst layer (CL) where electrochemical conversion of the fuel and oxidant takes place. A schematic diagram of the cathode is shown in **Figure 1.8**, depicting the microstructure of the CL that is optimized to maximize the active Pt surface area, minimize barriers to reactant transport and help maintain consistent performance over time under varying fuel cell operating conditions.(21)

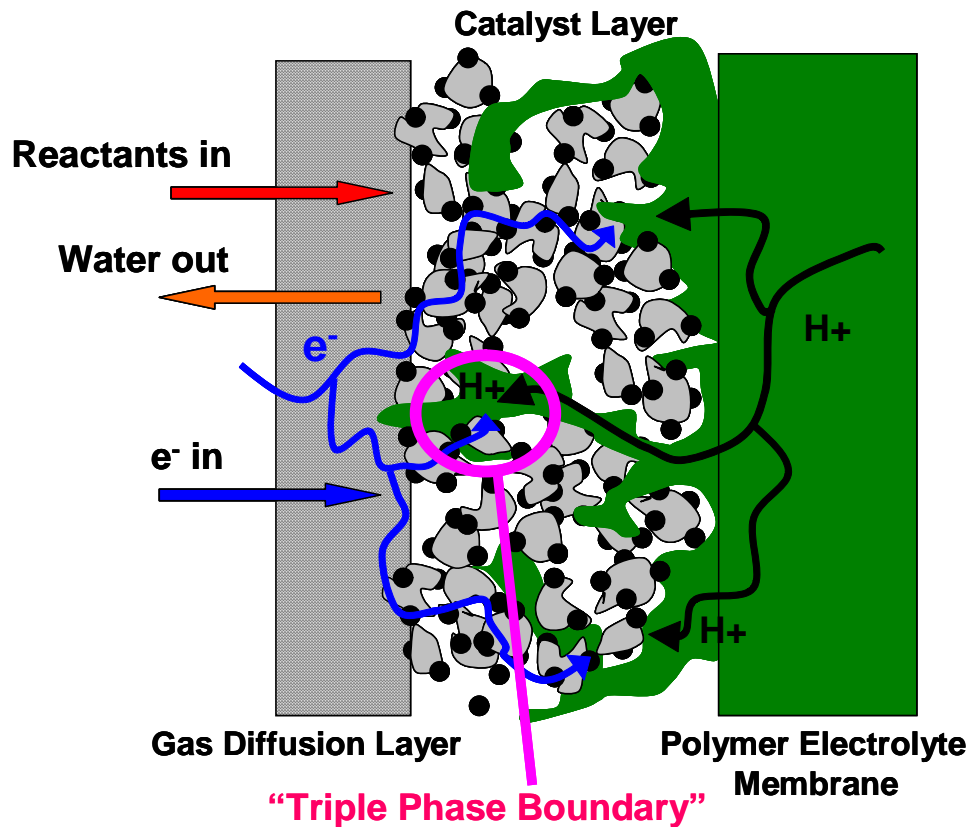


Figure 1.8: Schematic diagram of a PEM cathode catalyst layer.

The complexity of the catalyst layer has been noted by several groups, with specific properties required of each component to ensure maximum performance.(5, 50-52) The following properties are advantageous for an effective catalyst layer:

- an ionic pathway for protons that also presents a low barrier for O<sub>2</sub> permeability
- electronic connectivity throughout the catalyst layer
- an electrode structure that has hydrophobic gas passages to allow distribution of reactants to the catalyst particles and suitable for removal of liquid water
- a gas diffusion electrode substrate that provides mechanical support and electrical contact(20)

As depicted in **Figure 1.8**, inside the catalyst layer is a “triple phase boundary” for the ORR in which protons, oxygen and electrons combine electrochemically on Pt. Satisfying the above requirements and maximizing the “triple phase boundary” is imperative for high performance fuel cells.

Substantial research towards increasing the performance, utilization and durability of PEMFC cathode catalyst layers has taken place over the past 40 years.(53) Initially, Pt black (10 - 20 mg cm<sup>-2</sup> Pt loading) was used in conjunction with polytetrafluoroethylene (PTFE), which served as a binder and a hydrophobic agent. However, spurred by the increasing cost of Pt and the focus on commercial applications of fuel cells, significant progress in catalyst layer design

using Pt supported on high surface area carbon has reduced the Pt content to < 0.4 mg cm<sup>-2</sup>.(5)

Impregnation of a proton conducting polymer (e.g., Nafion<sup>®</sup> ionomer) into a carbon-supported Pt catalyst layer resulted in an increased utilization of the catalyst layer due to an increase in number of triple phase boundary locations, and a reduction in thickness of the CL, which in turn reduced their Ohmic resistance of the electrodes and improved mass transport of gases.(50, 51) The hydrophobic nature of Nafion<sup>®</sup>'s perfluorinated backbone also removed the requirement for incorporating PTFE into the CL.(54) Further improvements established that Nafion<sup>®</sup> contents of 30 - 35 wt% were optimized for minimal ohmic resistance and mass transport.(51, 52, 55)

#### **1.4.1 Activity Benchmarks for Pt and Pt-Alloy Catalysts**

The choice of the electrocatalyst has generated much interest over the last half century. PEMFCs commonly use Pt, as studies have shown that it is the best catalyst for both hydrogen and oxygen fuel cell reactions.(5, 56, 57) However, Pt suffers from a low tolerance to trace CO mixing with the anodic fuel (H<sub>2</sub>). Substantial attention has been directed at replacing Pt with alternative catalysts possessing a higher tolerance to CO poisoning, enhanced durability and higher catalyst activity. Recent work by Qi *et al.*(54) and Stamenkovic *et al.*(58) illustrates the potential of developing Pt-alloy catalysts for fuel cells. Stamenkovic reports that Pt<sub>3</sub>Ni(111) is 90-times more active than the current state-of-the-art Pt/C catalysts. A recent review by Gasteiger *et al.*(59) outlines of the strategies for increasing Pt catalyst activity *via* alloying with other metals. Pt

alloys are reported to have superior activity over Pt, enhancing the ORR specific activity ( $\mu\text{A cm}^{-2} \text{ Pt}$ ) by a factor of 2 - 10. A corresponding increase in mass activity ( $\text{A mg}^{-1}$ ) may be achieved if the electrochemical surface area is maintained at the same values of current Pt/C catalysts ( $70 - 90 \text{ m}^2 \text{ g}^{-1}$ ).<sup>(59)</sup> However, these studies have yet to make an impact on commercial PEMFCs.

#### **1.4.2 Non-Nafion<sup>®</sup>-Based Catalyst Layers**

A search of the peer-reviewed literature reveals that the proton conducting medium used in fuel cell catalyst layers is almost exclusively Nafion<sup>®</sup>. However several shortcomings such as decreased membrane electrode interfacial compatibility with non-PFSI membranes, poor mechanical stability at temperatures  $>100 \text{ }^\circ\text{C}$  and low protonic conductivity under reduced relative humidity and elevated temperature are observed for these materials.<sup>(60, 61)</sup> Given that extensive research is underway to replace Nafion as the proton exchange membrane with hydrocarbon ionomers, it seems pertinent to understand and develop catalyst layers in which Nafion is also replaced with hydrocarbon proton conducting media.

Literature addressing the incorporation of non-Nafion<sup>®</sup> ionomers into the catalyst layers is limited. However, recent work in this area was emphasized by the groups of Holdcroft<sup>(60)</sup>, Lindbergh<sup>(62)</sup>, Mukerjee<sup>(42)</sup>, Pivovar<sup>(61)</sup>, Watanabe<sup>(63)</sup>, Ramani<sup>(64)</sup>, Fenton<sup>(65)</sup> and Park<sup>(66, 67)</sup>. These authors highlight the importance of designing the MEA using the same electrolyte throughout the MEA. The novel polymer electrolytes used above are based on hydrocarbon polyarylene ionomers similar to those previously outlined in section

1.3.2, namely, polyarylene sulfonated poly(ether ether ketone) (SPEEK), sulfonated polysulfone (sPSU), sulfonated polysulfide sulfone (SPSS), sulfonated poly(arylene ether sulfone) (sPAES), and poly(ether ketone ketone) (SPEKK). It should be noted that these published works have appeared within the past 5 years, emphasizing the infancy of this area of fuel cell research.

These reports demonstrate the importance of the relationship between the ion exchange capacity (IEC) of the hydrocarbon ionomer, the electrochemistry of the catalyst layer, and fuel cell performance. Easton *et al.*(60) establishes the dependence of the IEC on the interfacial resistance of the PEM| cathode interface and the electrochemical surface area (ESA). The importance of reducing the interfacial resistance of the MEA by bonding the membrane to a catalyst layer containing a solid polymer electrolyte of similar chemical structure to the PEM is illustrated. Additionally, the effect of adding a hydrophobic binder, PTFE, to the SPEEK ionomer catalyst layer is also shown. The presence of PTFE aids water management within the catalyst layer due to its hydrophobic, perfluorinated backbone and also because it creates a more porous CL microstructure that facilitates water transport. A further benefit due to the presence of PTFE in the SPEEK-based CL is that it increases the oxygen solubility within the electrode, as it is well known that oxygen is more soluble in a perfluorinated material than a hydrocarbon material. Zhang *et al.*(43) confirm the higher oxygen solubility in perfluorinated materials by comparing the O<sub>2</sub> transport properties at the Pt| membrane interface for Nafion<sup>®</sup> and sulfonated poly(arylene ether sulfone) membranes. They also confirm that the oxygen permeability of

Nafion<sup>®</sup> is 1.5 to 3 times larger than that for sulfonated polyether sulfone membranes depending on the operational temperature, largely because of differences in oxygen solubility.

Von Kraemer *et al.*(62) published work that supports the need for reducing the resistance at the CL/PEM interface by studying MEAs based on sulfonated polysulfone (sPSU). A lower Ohmic resistance was observed for MEAs incorporating the same proton conducting medium in the membrane and CL. However, current densities in sPSU-based MEAs were limited by O<sub>2</sub> mass transport in the range of 600 – 800 mA cm<sup>-2</sup>, most likely attributed to the accumulation of water in the cathode.

Ma *et al.*(42) stress that using a different ionomer in the CL is deleterious to the fuel cells performance, due to the possibility of a junction potential between the CL and the membrane. The fuel cell performance of sulfonated polyarylene ether sulfone- and Nafion<sup>®</sup>-based MEAs indicate that catalyst layers based on the sulfonated polysulfone exhibit significantly poorer kinetics for the oxygen reduction reaction compared to Nafion<sup>®</sup>-based electrodes.

Electrochemical analysis of MEAs prepared from slightly different solid polymer electrolyte, sulfonated poly(ether ketone ketone) (SPEKK), was reported by Ramani *et al.*(65). SPEKK-based MEAs gave inferior performance to Nafion<sup>®</sup>-based MEAs, as the lower activity of the SPEKK-based cathodes observed was attributed to a lower electrochemically active surface area (ESA), in addition to lower oxygen permeability, when compared to Nafion<sup>®</sup>-based systems.

Additionally, the ESA was found to increase when the IEC of SPEKK in the cathode catalyst layer was increased from 1.4 to 2.1 mequiv g<sup>-1</sup>.

Jorrisen *et al.*(35) and Scott *et al.*(68) report that dissimilarities in the solid polymer electrolyte used in the CL and PEM affects the durability of the MEA. In these studies, blends of sulfonated polyarylenes polymers and radiation-grafted proton exchange membranes, based on PE and ETFE were investigated. The interface between the membrane and the catalyst layer suffered from poor stability and delamination when different solid polymer electrolytes were used. With required lifetimes of fuel cell being in excess of 10,000 h, the importance of understanding the role of new solid polymer electrolytes in both PEMs and CLs takes on added significance.(20)

## **1.5 Physical Experimental and Electrochemical Theory Relevant to Fuel Cell Catalyst Layer Analysis**

### **1.5.1 Physical Experimental Techniques**

#### **1.5.1.1: Scanning Electron Microscopy**

Scanning electron microscopy (SEM) permits the observation and characterization of heterogeneous materials on a nanometer (nm) to micrometer ( $\mu\text{m}$ ) scale. Full image and structure analysis capabilities and the theory of SEM are reviewed by Goldstein *et al.*(69), and are discussed briefly here. In SEM, the area to be examined is irradiated with a finely focused electron beam that is swept across the sample to form images. The types of signals produced from the interaction of the electron beam with the sample include secondary electrons, backscattered electrons, characteristic x-rays, and other photons of various

energies. These signals are obtained from specific emission volumes within the sample, and are collected by detectors to form images of the sample displayed on a cathode ray tube screen. The signals of greatest use are the secondary and backscattered electrons because these vary primarily as a result of differences in surface topography. The secondary electron emission, confined to a very small volume near the beam impact area on the sample, permits images to be obtained at a resolution of the size of the electron beam. Three dimensional images are attainable in SEM due to the large depth of field, with a useful magnification of up to 100,000 times.(69) With SEM samples not needing to be transparent to electrons, the technique can be applied to characterization of fuel cell catalyst layers comprised of Pt/C, PTFE and ionomer deposited on to a carbon paper substrate. Visualization of the catalyst layer surface and the associated differences due to ionomer, fabrication method and solvent choice can be observed for both Nafion<sup>®</sup> and SPEEK catalyst layers.

#### **1.5.1.2: Porosimetric Analysis of the Catalyst Layer**

Mercury porosimetric analysis of the catalyst layer allows quantification of the pore size and pore size distribution. This technique applies varying pressures to a sample immersed in mercury, with the pressure required to intrude mercury into the sample's pores being inversely proportional to the size of the pores.(20) The measurement principle is based on the law of capillary pressure governing liquid penetration into small pores. In the case of a non-wetting liquid (contact angle,  $\theta > 90^\circ$ ), such as mercury, and assuming pores of

cylindrical shape, this law can be expressed by the Washburn equation, shown in equation 1.18,(70, 71)

$$d = \frac{-4\sigma_{Hg} \cos \theta_{Hg}}{P}, \quad (1.18)$$

where  $d$  is the pore diameter,  $P$  the applied pressure,  $\sigma_{Hg}$  the surface tension,  $\theta_{HG}$  the contact angle. The values of  $\sigma_{Hg}$  and  $\theta_{Hg}$  used in this thesis are 485 dyn  $\text{cm}^{-1}$  and  $130^\circ$ , respectively. The volume of mercury penetrating the pores is measured directly as a function of the applied pressure, with it the pore volume is known for a certain pore radius. This pressure-volume information serves as a unique characterization of the pore structure. Since the range of the pressure and the pore radius extend over three orders of magnitude, the pore size is indicated in a logarithmic scale.(72)

### 1.5.1.3: Contact Angle Measurements

The hydrophobicity, or wettability, of a surface is dependent on two factors: the intrinsic property of the material (surface tension) and surface roughness.(73) The contact angle of a water drop placed on a surface has been commonly used to gauge surface wettability, while measurement of the contact angle made by a drop of water on a catalyst layer allows information on the hydrophobicity of the catalyst layer to be obtained.(74) The liquid-vapor interfacial tension  $\sigma_{lv}$  and the contact angle  $\theta$  are two important properties of a system and differ with changes in material or processing conditions. The interfacial tension,  $\sigma_{lv}$ , determines the interfacial behaviour of a liquid in contact

with a vapour. If a solid surface is included, then the degree of wetting can be calculated. The degree of wetting itself is related to the contact angle,  $\theta$ . Both of these properties are correlated in the Young equation, shown below,(75, 76)

$$\sigma_{sv} = \sigma_{sl} + \sigma_{lv} \cos \theta, \quad (1.19)$$

where  $\sigma_{sv}$ ,  $\sigma_{sl}$  and  $\sigma_{lv}$  are the interfacial free energies per unit area of the solid-gas, solid-liquid and liquid-gas interfaces, respectively. This correlation can be understood by considering the horizontal force balance at the three-phase contact point for a drop of water on a surface as shown in **Figure 1.9**.

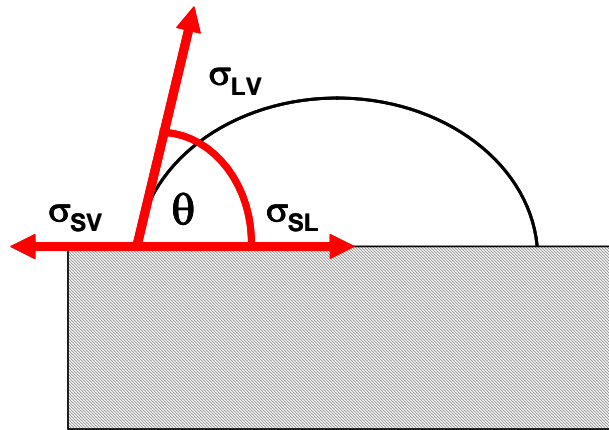


**Figure 1.9: Force balance at the three-phase contact point according to Young.(76)**

The meeting point of the three phases: the drop, the continuous phase, and the supporting phase, is called the three-phase contact point. Here, the magnitude of the three force vectors, the solid-gas,  $\sigma_{sv}$ , the liquid-gas,  $\sigma_{lv}$ , and the solid-liquid interfacial tension,  $\sigma_{sl}$ , determines the contact angle,  $\theta$ .(75, 76)

## 1.5.2 Electrochemical Techniques

Potentiostatic and galvanostatic electrochemical experimental techniques are essential tools for quantifying electrochemical characteristics of fuel cells. The following section outlines the techniques used within this thesis.

### 1.5.2.1 Evaluation of Electrode Kinetics of O<sub>2</sub> Reduction from Slow-Sweep Voltammetry

Slow-sweep cyclic voltammetry (CV) is a technique whereby the voltage at a working electrode is swept between two potentials and is characterized by a slow potential sweep rate (*i.e.*, 2 - 5 mV s<sup>-1</sup>). At slow sweep rates, the current rises to a limiting value proportional to the concentration of the active species in the electrolyte.(20) The diffusion limited current,  $I_d$ , due to electrochemical reduction or oxidation of an electroactive species dissolved in the electrolyte is given by equation 1.20,(7, 77)

$$I_d = \pi n F D_b C_b r, \quad (1.20)$$

where  $n$  is the number of electrons transferred in the overall reaction ( $n = 4$  for ORR),  $A$  is the geometric area of the electrode,  $F$  is Faraday's constant,  $D_b$  is the diffusion coefficient of the electroactive component,  $c_b$  is the solubility, and  $r$  is the radius of the microelectrode. Electrode kinetic parameters including exchange current densities,  $j_d$ , Tafel slopes, and transfer coefficients can be extracted from slow sweep voltammetry data using a mass transfer corrected Tafel equation, shown below in equation 1.21, (78, 79)

$$\eta = \frac{2.303RT}{\alpha n F} \log j_o + \frac{-2.303RT}{\alpha n F} \log \left[ \frac{j_d j}{j_d - j} \right], \quad (1.21)$$

where  $\eta$  is the overpotential ( $E - E^\circ$ ),  $R$  is the gas constant,  $T$  is the absolute temperature in Kelvin,  $\alpha$  is the transfer coefficient,  $j_o$  is the exchange current density,  $j$  is the current density, and  $j_d$  is the diffusion-limited current density.

### 1.5.2.2 Chronoamperometry using Microelectrodes

Chronoamperometry is an electrochemical technique whereby the potential of a working electrode is stepped from a value where no reaction occurs to one where the electroactive species is oxidized or reduced at a diffusion controlled rate, and the resulting current from the Faradic process is monitored as a function of time. A microelectrode electrochemical setup is used to determine oxygen mass transport parameters of PEMs. Because of their size ( $\sim 100 \mu\text{m}$ ), microelectrodes operate in different mass-transfer regimes depending on the experimental conditions employed. The change at a microelectrode from essentially linear diffusion (Cottrell-like behaviour) at short times to spherical diffusion at long times is shown in **Figure 1.10**.(7, 80)

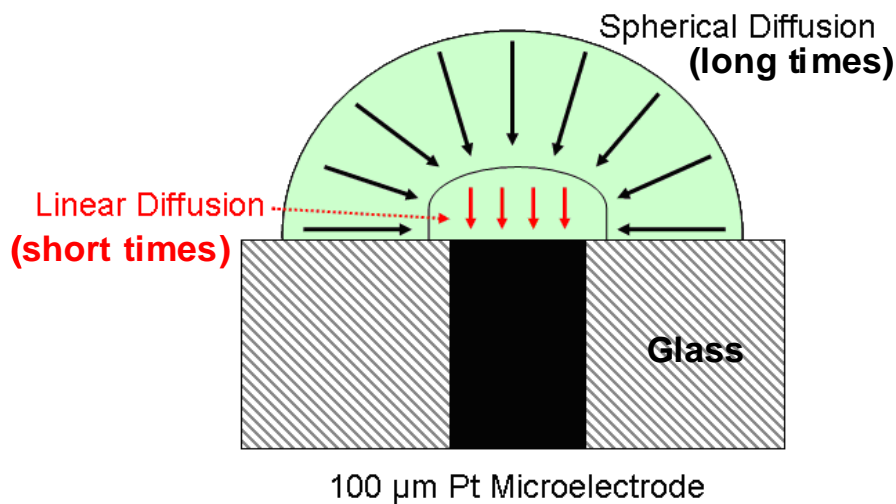


**Figure 1.10: Transition to spherical diffusion to semi-infinite, linear diffusion for electrolysis at a Pt microelectrode.(7)**

With careful consideration, experiments can be performed in either regime; with short times allowing oxygen mass transport parameters to be determined due to linear diffusion to the electrode surface. The diffusion coefficient, solubility, and permeability of the electroactive species in an electrolyte, or in this case a solid polymer electrolyte membrane, can be determined. The relationship between these parameters is described by the Cottrell equation as shown in equation 1.22, where at short times the current flowing at the microelectrode interface resembles that of a linear diffusion field,(7, 81)

$$I(t) = \frac{nFAD_b^{1/2}c_b}{\pi^{1/2}t^{1/2}} + \pi nFD_c c_b r, \quad (1.22)$$

where A is the geometric area, F is Faraday's constant,  $D_b$  is the diffusion coefficient of the electroactive component,  $c_b$  is the solubility, r is the radius of the microelectrode and all other symbols have their usual meaning. Thus, the diffusion coefficient,  $D_b$ , and solubility,  $c_b$ , values can be obtained from the slope and intercept (int) of a plot of I vs.  $t^{-1/2}$ . Permeability is the product  $D_b c_b$ .

$$D_b = \frac{r^2(\text{int})^2}{\pi(\text{slope})^2} \quad (1.23)$$

$$c_b = \frac{(\text{slope})^2}{nFr^3(\text{int})} \quad (1.24)$$

### 1.5.2.3 Electrochemically Active Surface Area (ESA) Determined by Cyclic Voltammetry

Determination of the Pt specific surface area in the catalyst layer, defined as the effective area per unit of Pt mass, is an essential property for comparing fuel cell electrodes. Cyclic voltammetry of hydrogen adsorption/desorption is a well established technique to measure the electrochemically active surface area (ESA) of Pt, and is suitable for evaluating and characterizing Nafion<sup>®</sup>- and SPEEK-based catalyst layers.(82) The specific reaction of interest, shown below, is the electrochemical reduction of protons (H<sup>+</sup>) and the subsequent deposition of atomic hydrogen on the Pt surface.(8, 83)



The charge density ( $Q_{\text{H}}$  in C cm<sup>-2</sup>) due to the adsorption of atomic hydrogen in a voltammetric measurement is shown in **Figure 1.11**.

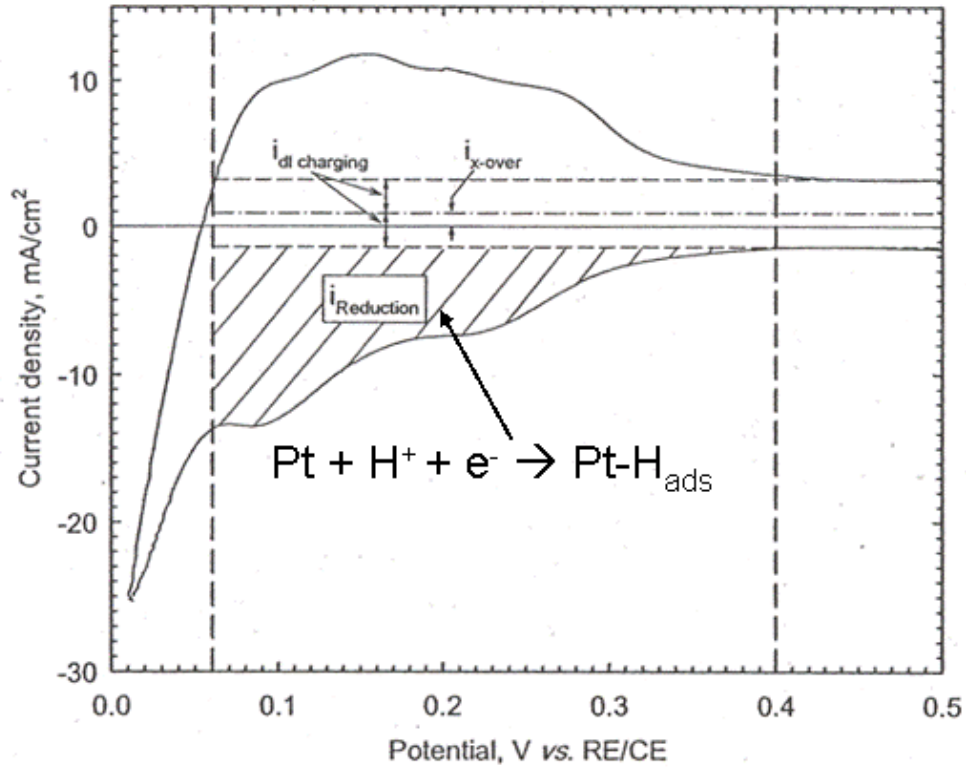


Figure 1.11: Cyclic voltammogram showing adsorption and desorption of protons on Pt in acidic media. Reprinted from ref. (8). Copyright (2007), with permission from Scribner Associates Inc.

The electrochemically active surface area (ESA) of the Pt catalyst is calculated using equation 1.26, which uses the charge accumulated due to the formation of Pt-H<sub>ads</sub> ( $\Gamma = 210\mu\text{C cm}^{-2}$ ), and the Pt content in the electrode (mg Pt cm<sup>-2</sup>). (8, 20) In order to account only for the active fraction of catalyst, the charge arising from the growth of the double layer ( $i_{dl}$  charging region in **Figure 1.11**) must be accounted for prior to determining the charge due to Pt-H<sub>ads</sub>.

$$\text{ESA} = Q_H / ([\text{Pt}] \times 0.21) \quad (1.26)$$

#### **1.5.2.4 Electrochemical Impedance Spectroscopy**

Electrochemical impedance spectroscopy (EIS) is a non-invasive technique for evaluating fuel cell properties such as membrane and electrode resistance, reaction kinetics, and mass transport. EIS allows for deconvolution of competing processes occurring in the fuel cell as processes respond over a wide range of frequencies. For example, diffusional processes occur on the time scale of milli-seconds to seconds, whereas charge transfer processes occur over much shorter time scales (sub-milliseconds). Because time constants differ for different processes, their effects are revealed at different frequencies.(7, 8) Moreover, EIS experiments allow studying the intrinsic properties that affect the conductivity of the catalyst layer, and also allow separation of the parameters that contribute to the response into two categories. In order to extract meaningful values from the different electrochemical responses, an equivalent circuit model is employed to fit EIS experimental data. The use of an equivalent circuit often comprises resistors, capacitors, and various distributed circuit elements corresponding to physical phenomenon such as a diffusion or mass transport limiting process.(84) Table 1.1 lists common circuit elements, the IV relationship, and their impedance.(7)

**Table 1.1: Impedance relationships of ideal electrical circuit elements commonly used to describe the impedance responses of fuel cells.(7, 8)**

<b>Element</b>	<b>Defining Relationship</b>	<b>Impedance</b>
<b>Resistor</b>	$V = IR$	$Z_R = R$
<b>Capacitor</b>	$I = C^*(dV/dt)$	$Z_C = 1/(j\omega C)$
<b>Inductor</b>	$V = L (dI/dt)$	$Z_L = j\omega L$

A frequently used circuit, the Randles equivalent circuit, is shown in **Figure 1.12.(7)** Parallel elements are introduced because the total current through the working interface is the sum of distinct contributions from the Faradic process and double layer charging. The double-layer capacitance in the electrode is, ideally, a pure capacitance and is represented by the element  $C_{dl}$ . The Faradic process cannot be represented by simple linear circuit elements such  $R$  and  $C$ , whose values are independent of frequency, but must be considered as a general impedance, separated into a pure resistance,  $R_{CT}$  (the charge transfer resistance), and a general impedance,  $Z_w$  (the Warburg impedance), which represents a resistance to mass transfer at the electrode. Additionally, all current is subject to cell and hardware resistances; therefore  $R_s$  is introduced as a series resistive element to represent their effect.(7, 8)

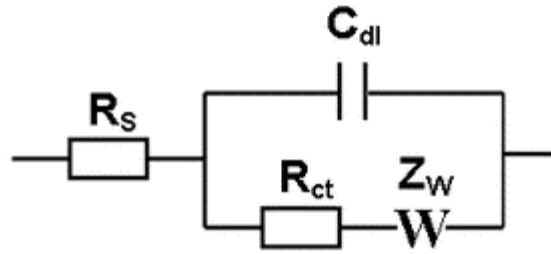


**Figure 1.12: Randles equivalent circuit with mixed kinetic and charge transfer control in a fuel cell.(7)**

For measurements of ionic resistance in the catalyst layer, the theory present by Eikerling *et al.*(85), based on a one-dimensional transmission line equivalent circuit depicted in **Figure 1.13**, can be employed to determine the ionic conductivity/resistivity of the ionomer in the catalyst layer.

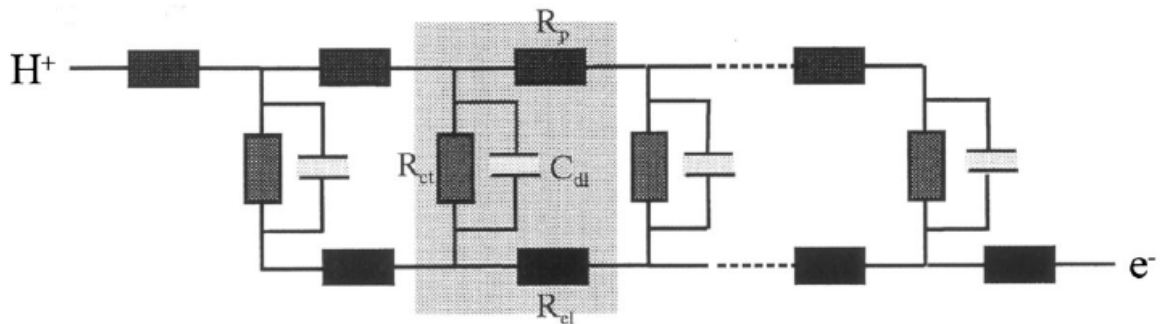


**Figure 1.13: A one-dimensional transmission line equivalent circuit. The elementary unit comprising protonic resistivity  $R_p$ , charge transfer resistivity  $R_{CT}$ , double layer capacitance  $C_{dl}$ , and electronic resistivity  $R_{el}$  is highlighted. Reprinted from ref. (85). Copyright (1999), with permission from Elsevier.**

From this theory, a discretized transmission line with  $m$  elements can be used to mimic the continuous electrical network of carbon and Pt particles in the catalyst layer. Each element in the transmission line consists of a proton resistance ( $R_p$ ), a charge transfer resistance ( $R_{CT}$ ) and an electronic resistance

( $R_{el}$ ).  $R_{el}$  can be neglected due to its small magnitude in comparison to other resistances. Double layer charging effects are represented by double layer capacitances  $C_{dl}$  in parallel to  $R_{CT}$ .(85) Using EIS, the protonic resistance of the catalyst layer can be quantified using theory developed by Eikerling *et al.*(85) and Havranek *et al.*(86). Briefly, ionic transport and double layer charging of the electrode dominate the high frequency region (>1K Hz) of Nyquist plots for porous media. A straight line with 45° slope is observed in the high-frequency limit when operating the cell under nitrogen. The linear feature corresponds to an electrode operating under a limiting proton transport case. The linear slope of the electrodes EIS spectrum ( $10^4$ –  $10^3$  Hz), representing the contribution from the protonic resistance and double layer charging capacitance of the catalyst layer, can be expressed by equation 1.27,

$$|Z| = \sqrt{R_p / C_{dl}} \times \omega^{-1/2} \rightarrow K = \sqrt{R_p / C_{dl}} , \quad (1.27)$$

where  $|Z|$  is the magnitude of the impedance,  $C_{dl}$  is the double layer capacitance of the electrode and  $\omega$  is the frequency of harmonic signal equal to  $2\pi f$ .(86) By means of equation (1.26), plotting  $|Z|$  vs.  $\omega^{-1/2}$  allows the slope,  $K$ , to be calculated, which yields the ratio of the proton resistance and the pseudo-double layer capacitance.

## 1.6 Thesis Structure

As outlined above, the need to understand the role of the solid polymer electrolyte in the catalyst layers is paramount to the development of membrane electrode assemblies that incorporate alternative proton exchange electrolytes.

Investigating the role of novel solid polymer electrolytes based on sulfonated hydrocarbon polymers on the electrochemical activity of catalyst layers, particularly cathode catalyst layers, is a logical step in the evolution of PEMFCs. Without this scientific understanding, progress in this developing area will be significantly impeded, and limited to trial-and-error approaches. The basis of this thesis work, therefore, is to develop a methodology and rational approach to study, interpret and understand the physical and electrochemical relationships resulting from incorporation of a non-Nafion<sup>®</sup> electrolytes in PEMFC catalyst layers, specifically sulfonated hydrocarbon polymers.

Sulfonated poly(ether ether ketone) (SPEEK) was chosen as the model proton conducting electrolyte for this work as it has been shown to possess many of the desired properties, including reasonable thermal stability, chemical inertness, high proton conductivity, and reduced methanol crossover when used in DMFC applications, for fuel cell applications.(38, 39, 60, 87) SPEEK is used as the proton conducting medium in both the catalyst layer and the PEM in this work. This thesis probes the relationship between parameters such as intrinsic properties of the proton conducting polymer, protonic conductivity of the catalyst layer, electrochemically active surface area (ESA), catalyst layer microstructure, and oxygen permeability, allowing a broader understanding of the complex relation between the proton conducting polymer, catalyst layer, and the PEM. The knowledge gained from using this model system not only allows the present material to be evaluated, but also provides direction towards the design of alternative hydrocarbon polymer electrolytes for catalyst layers.

**Chapter 2** of this thesis describes studies performed to gain a further understanding of the kinetics and mass transport properties of electrochemical oxygen reduction in SPEEK and Nafion<sup>®</sup>. A series of sulfonated poly(ether ether ketone) polymers were synthesized to provide membranes with varying ion exchange capacities (IEC). Solid state electrochemical measurements were performed at varying temperatures using a solid-state electrochemical cell built in-house. The cell mimics a fuel cell environment by allowing control of temperature and pressure. ORR electrochemical kinetics, and oxygen diffusion coefficients, oxygen solubility and oxygen permeability were determined using slow sweep voltammetry and chronoamperometry. These data are important because the performance of fuel cells is strongly influenced by the kinetic and mass transport properties related to ORR.

**Chapter 3** describes the preparation of SPEEK-based catalyst layers and their physical analysis. Two fabrication methods are described. The first is based on a traditional method for incorporating novel ionomers, which results in a graded distribution of the polymer electrolyte. The second is based on a modified fabrication method that results in a homogenous distribution of the polymer electrolyte. Analytical techniques, including scanning electron microscopy (SEM), mercury porosimetry, and contact angle determination, are employed to quantify the physical differences between Nafion<sup>®</sup>- and SPEEK-containing catalyst layers.

**Chapter 4** focuses on the electrochemical properties of catalyst layers, and membrane electrode assemblies prepared from SPEEK electrolyte. MEAs

of varying structure are fabricated and characterized by current-voltage polarization (IV), cyclic voltammetry (CV), and electrochemical impedance spectroscopy (EIS). The ionic resistance, electrochemically active area, polarization performance and mass transport resistances associated with the catalyst layers are quantified.

**Chapter 5** summarizes the thesis research, proposes future work in the study of solid polymer electrolytes for catalyst layer layers, and discusses the properties of the electrolyte that better suit the requirements of fuel cell catalyst layers.

## CHAPTER 2: ELECTROCHEMICAL REDUCTION OF OXYGEN AT PT | NAFION<sup>®</sup> 117 AND SPEEK INTERFACES

### 2.1 Introduction

New polymer electrolytes, such as sulfonated poly(ether ether ketone) (SPEEK), sulfonated polysulfone (sPSU), sulfonated polysulfide sulfone (SPSS), and polybenzimidazole (PBI) for use in catalyst layers in a PEM fuel cell require not only sufficient proton conduction, but also sufficient mass transport of O<sub>2</sub> within the electrolyte.(39, 42, 44, 88-90) This is because for an electrochemical charge transfer to occur, dissolved reactant in the electrolyte must diffuse to catalyst sites. Reactant transport, or permeation, is comprised of two parameters: the oxygen solubility ( $c_b$ ), and oxygen diffusion coefficient ( $D_b$ ). Jointly, they determine the availability of the oxygen species for ORR at the electrocatalyst| electrolyte interface within the cathode catalyst layer.(90)

Pioneering studies undertaken by Parthasarathy *et al.*(78, 79, 91, 92), Srinivasan *et al.*(93) and Mukerjee *et al.*(56) have contributed significantly to the understanding of mass transport properties and kinetic parameters associated with ORR in perfluorosulfonic membranes such as Nafion<sup>®</sup>. These studies used an electrochemical cell designed to perform solid-state electrochemistry under conditions of controlled temperature, pressure, and relative humidity (RH). By studying the membrane in a solid-state cell, a supporting aqueous electrolyte is

not necessary, allowing mass transport properties and kinetic parameters within the membrane to be studied exclusively.

Continuing work by Holdcroft and co-workers (77, 94, 95) expanded upon the relationship between chemical composition and the mass transport properties by studying a series of  $\alpha,\beta,\beta$ -trifluorostyrene-co-substituted- $\alpha,\beta,\beta$ -trifluorostyrene (BAM<sup>®</sup>) (EW 407-735 g mol<sup>-1</sup>) and sulfonated styrene-(ethylene-butylene)-styrene copolymer (DAIS-Analytical) (EW 585–1062 g mol<sup>-1</sup>) membranes. Trends in mass transport properties for BAM<sup>®</sup> and DAIS PEMs supported the initial results obtained for perfluorosulfonic membranes.(56, 78, 79, 93) Both PEMs showed the same dependence to pressure and temperature as Nafion<sup>®</sup>. Membranes obeyed Henry's 1<sup>st</sup> Law of higher oxygen solubility with increased pressure. Diffusion coefficients were found to increase and O<sub>2</sub> solubility decreased with increasing temperature.

Studies by Zhang *et al.*(43, 90, 96) on sulfonated poly(arylene ether sulfone) and sulfonated poly(sulfide sulfone) membranes showed that the diffusion coefficient ( $D_b$ ) increased with IEC, while solubility ( $c_b$ ) decreased. These results were discussed in the context of water content and membrane microstructure. The water-filled channels connecting the hydrophilic ionic clusters within the sulfonated poly(arylene ether sulfone) membranes and sulfonated poly(sulfide sulfone) membranes appear to make important contributions to O<sub>2</sub> diffusion.(90)

Mitsushima *et al.*(97) studied the oxygen reduction reaction on Pt microelectrodes for Nafion<sup>®</sup> 117 (DuPont), Aciplex<sup>®</sup> S-1104 (Asahi Chemical

Industry Co., Ltd.), Aciplex<sup>®</sup> S-1004 (Asahi Chemical Industry Co., Ltd.) and Flemion<sup>®</sup> HR (Asahi Glass Co., Ltd.), membranes possessing equivalent weights of 1100, 1050, 950, and 900, respectively. Collectively, it was found that diffusion coefficients increased with temperature and ion exchange capacity. O<sub>2</sub> solubility increased with a decrease in temperature and ion exchange capacity. The dependence of the diffusion coefficient on temperature and equivalent weight were larger than those of the solubility. As a result, oxygen permeability increased with increasing temperature and decreased with increasing equivalent weight.

Lee *et al.*(98) investigated the effect of the temperature used for recasting membranes on the diffusion coefficient and solubility of oxygen. The diffusion coefficient was found to increase with decreasing recasting temperature, while oxygen solubility had the opposite tendency. XRD studies showed that the changes in the mass-transport parameters for different recast temperatures were due to changes in the ionomer morphology. Ionomers recast at low temperature were shown to offer high oxygen diffusivity, permeability and higher conductivity due to a higher water uptake.

Literature pertaining to the mass transport limitations of the hydrogen oxidation reaction (HOR) is limited due to the facile kinetics of the reaction and the overwhelming interest in the ORR. However, Ota *et al.*(99) investigated both the oxygen reduction reaction and hydrogen oxidation reaction at a Pt microelectrode interface with Nafion<sup>®</sup> of different equivalent weights (EW) at temperatures between 30 to 70 °C. The solubility of hydrogen increased with

increasing hydrophobicity of the membrane, *i.e.*, membranes with increasing high EW (lower IEC), while the diffusion coefficient was observed to decrease.

In this chapter, the oxygen transport properties and interfacial kinetics of the ORR in SPEEK membranes are studied under conditions that mimic the practical operating conditions of a PEM fuel cell. This is achieved using a solid-state electrochemical cell fabricated in-house. The effects of temperature on the kinetics of the oxygen reduction reaction (ORR) and oxygen mass transport parameters are investigated in the temperature range 303 – 323 K. Limiting current, oxygen diffusion, oxygen solubility and oxygen permeability, and kinetic parameters, such as Tafel slopes and exchange current densities ( $i_0$ ) are determined.

## **2.2 Experimental**

### **2.2.1 Materials**

Dimethylacetamide (DMAc), potassium hexachloroplatinate ( $K_2PtCl_6$ ) and concentrated sulfuric acid ( $H_2SO_4$ , 95 vol. %) were purchased from Alfa-Aesar and used as received. PEEK was supplied by Victrex USA Inc. De-ionized (D.I.) water (Millipore Co.) was used in washing and hydrating membranes. Hydrogen peroxide ( $H_2O_2$ ) and Nafion 117<sup>®</sup> extruded membrane were purchased from Sigma Aldrich. Nafion 117<sup>®</sup> possessed a thickness of 175  $\mu m$  and an IEC of 0.91 meq  $g^{-1}$ .

### 2.2.2 Sulfonation of Poly(Ether Ether Ketone)

Sulfonated poly(ether ether ketone), SPEEK, was prepared using a similar procedure to that reported by Easton *et al.*(60). 20.5 g of PEEK (Victrex 450 PF) was dissolved in 1L of concentrated sulfuric acid in a 3L round bottom flask and stirred vigorously at room temperature for 12 - 54 hours. SPEEK was precipitated as yellowish/white spheres by dropwise addition into 5 L of ice-cold de-ionized water with vigorous stirring. The sample was allowed to precipitate over ~8 hours before collection via vacuum filtration and thorough rinsing with D.I. water. Washing continued until the pH was neutral. The yellowish/white solid was dried overnight at 100 °C in air to give a yellow solid that was soluble in N,N-dimethylacetamide (DMAc). The synthetic route and sulfonated poly(ether ether ketone) in the solid, solution, and film/MEA form can be seen in **Figure 2.1** and **Figure 2.2**.

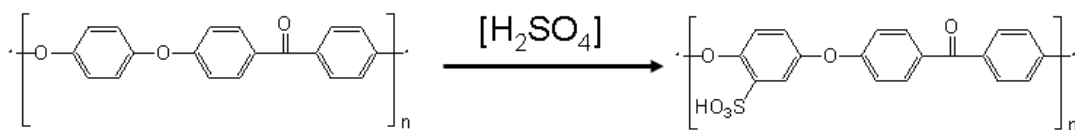


**Figure 2.1: Synthetic scheme for sulfonated poly(ether ether ketone) polymer.**

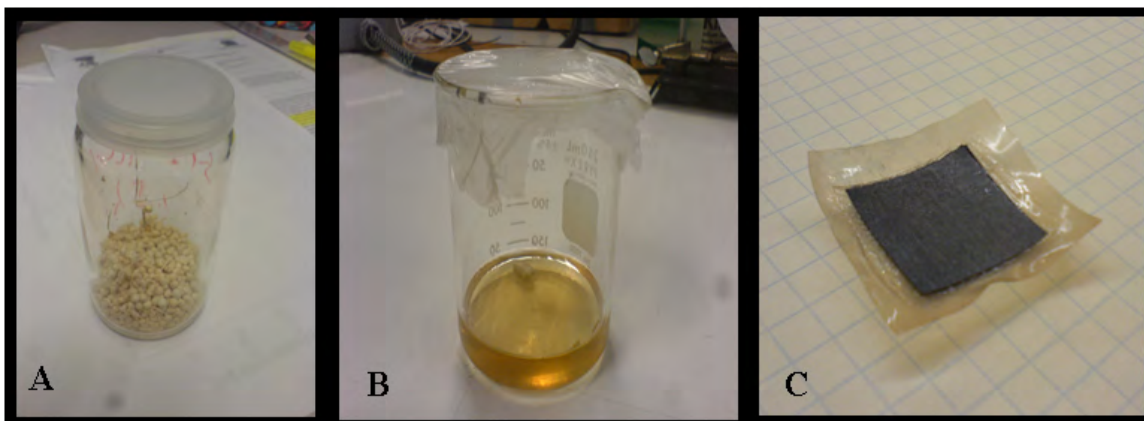


**Figure 2.2: Sulfonated poly(ether ether ketone) in solid (A), solution (DMAc) (B) and MEA (C) form.**

### **2.2.3 Preparation of Sulfonated Poly(Ether Ether Ketone) Membranes**

SPEEK membranes were prepared by solution casting from a 5 wt% solution in DMAc. The solution was cast onto a glass plate (15 x 15 cm) and dried at 70 °C under vacuum for 24 h. A uniform, semi-transparent, yellowish film was removed from the glass plate by soaking in D.I. water. Membranes were cast with a thickness of ~150  $\mu\text{m}$ . Membranes were soaked in 0.5 M  $\text{H}_2\text{SO}_4$  for 48 hours to ensure full protonation and to remove any residual DMAc. Membranes were rinsed and stored in D.I. water before use.

### **2.2.4 Determination of Ion Exchange Capacity**

The ion exchange capacity (IEC) is defined as the millimolar equivalents of reactive  $-\text{SO}_3\text{H}$  sites per gram of polymer and has units of  $\text{meq g}^{-1}$ . The ion exchange capacity of the SPEEK membranes were experimentally determined for each sample. Firstly, acidified SPEEK membranes were dried overnight at ~80 °C under vacuum before being weighed. The films were soaked in 2 M NaCl solution for ~5 h to exchange all the protons with  $\text{Na}^+$ . The electrolyte solution

was then titrated using a dilute NaOH solution of known concentration. The endpoint was detected using phenolphthalein (faint pink color appearance for ~20 s). The IEC was calculated from the moles of NaOH used, divided by the mass of the dry sample,  $M_{\text{dry}}$ , as given by equation 2.1.

$$\text{IEC}_{\text{Experimental}} = \frac{V_{\text{NaOH}}[\text{NaOH}]}{M_{\text{dry}}} \quad (2.1)$$

where  $V_{\text{NaOH}}$  and  $[\text{NaOH}]$  are the volume of NaOH used and its concentration, respectively. The reported experimentally-determined IECs are the average of at least five separate titrated samples. The standard deviation was calculated for each sample set with a confidence interval of 0.95.

### 2.2.5 Water Content of SPEEK Membranes

Water uptake was measured gravimetrically by determining the difference in mass of hydrated and dry membranes. SPEEK membranes were first dried under vacuum at 80 °C for at least 24 h and then weighed on an analytical balance. The membranes were then soaked for 24 hours in D.I. water. The samples were blotted dry with a kimwipe and weighed shortly after. Water uptake is defined as the amount of water per gram of dry membrane and can be calculated using equation 2.2,(20)

$$\text{Water Uptake} = \frac{M_{\text{wet}} - M_{\text{dry}}}{M_{\text{dry}}} \times 100 \quad (2.2)$$

where  $M_{\text{wet}}$  is the mass of the saturated membrane and  $M_{\text{dry}}$  is the mass of the dry membrane. At least five measurements were made for each sample. Water

content is defined as the percent of water that is contained in the membrane and can be calculated using equation 2.3.

$$\text{Water Content} = \frac{M_{\text{wet}} - M_{\text{dry}}}{M_{\text{wet}}} \times 100 \quad (2.3)$$

### 2.2.6 Proton Conductivity

A Solatron 1260 (Solartron Analytical) frequency response analyzer (FRA) was used to determine the conductivity of membranes. The perturbation amplitude of the ac signal was 100 mV rms over a frequency range 10 MHz to 100 Hz. All measurements were performed at ambient temperature ( $22 \pm 2$  °C) using a two-probe cell, which is shown schematically in **Figure 2.3**. The measurements were made on fully hydrated samples. Proton conductivity was calculated using equation 2.4.(20)

$$\sigma = \frac{L}{R_m \times A} . \quad (2.4)$$

where L is the distance between two Pt foil electrodes (~1 cm),  $R_m$  is the membrane resistance determined from AC impedance spectra, and A is the cross-sectional area of the membrane. The thickness of the membranes was measured using a 227-digimatic micrometer (Mitutoyo, U.S.A) and the width and length was measured using a digital caliper (Mitutoyo, U.S.A). The resistivity of the membranes were calculated using Zplot 2.8 software (Scribner Associates, Inc.).(100)

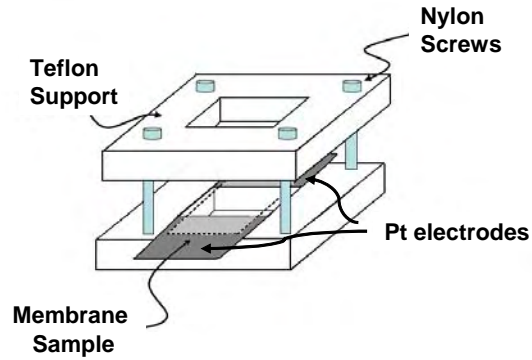


Figure 2.3: Schematic drawing of the two-probe cell used for measuring proton conductivity.(100)

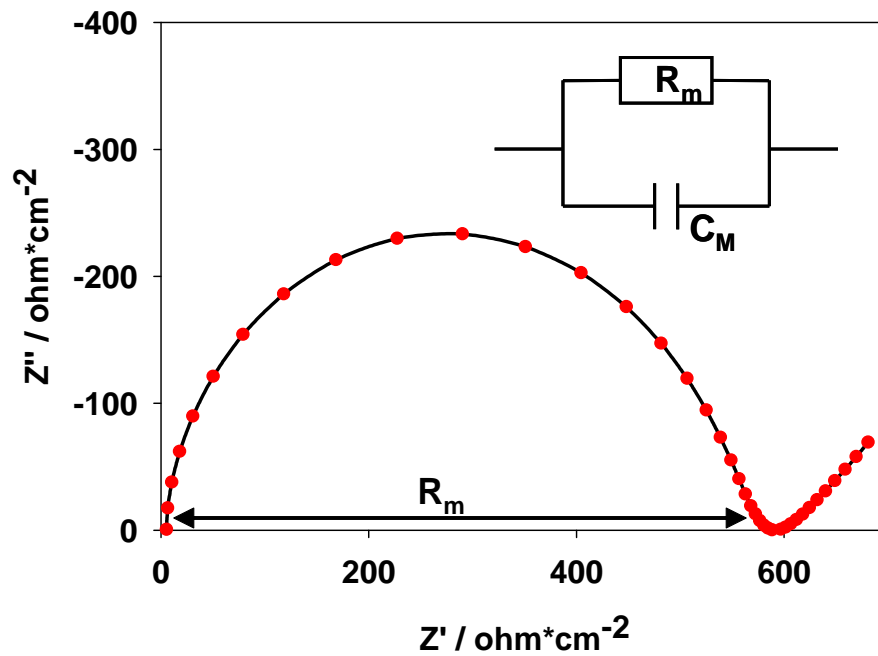


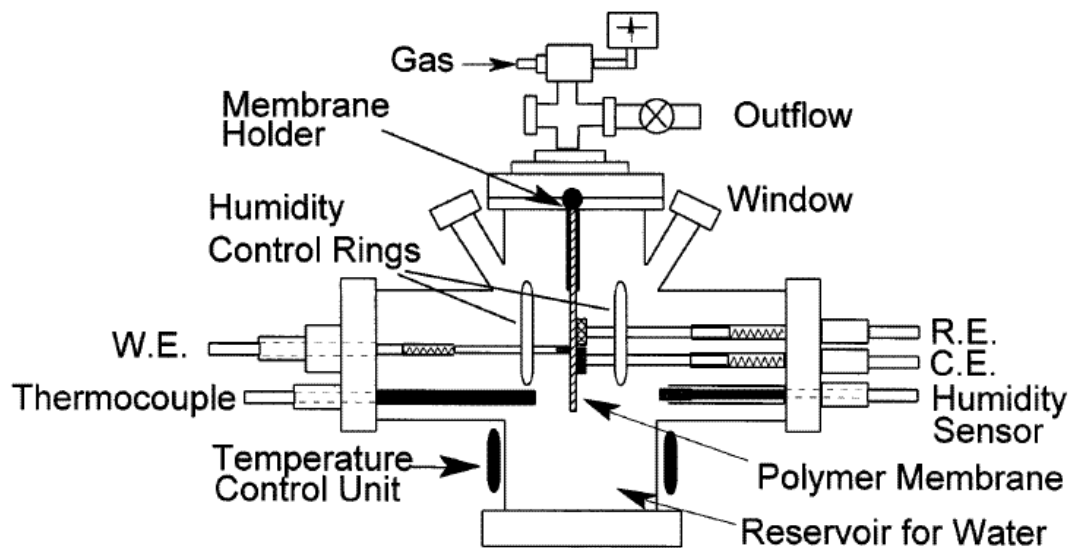
Figure 2.4: A typical Nyquist impedance plot from which proton conductivity data is calculated. Inset: Equivalent circuit used for fitting.  $R_m$ ,  $C_M$  represent the protonic resistance and capacitance of the membrane, respectively.(101)

The system used in this work can be represented as an equivalent circuit (inset **Figure 2.4**) with  $R_M$  (membrane resistance) and  $C_M$  (bulk membrane capacitance) being the main components. The relationship between the applied

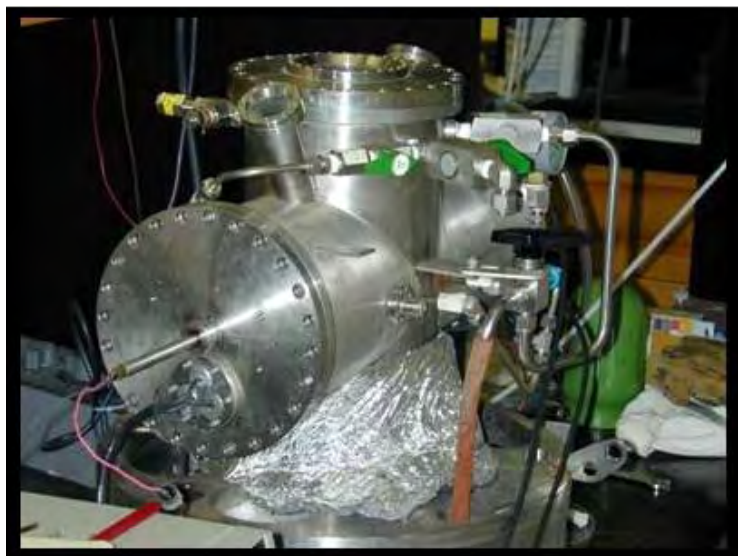
potential and the current flow is given by the impedance, which is the AC analog to the resistance-current-potential relationship of a DC circuit. The impedance ( $Z$ ) has a magnitude ( $\Delta E/\Delta i$ ) and phase ( $\phi$ ) and is thus a vector quantity. **Figure 2.4** shows a typical result obtained for a hydrated PEM. The important feature is the diameter of the semi-circle which is equal to  $R_M$ . At high frequency, where the curve intersects the  $Z'$  axis, the system is considered to be a pure Ohmic resistor. When the frequency decreases, the membrane capacitance dominates the impedance. The combination of the capacitance and resistance leads to the semi-circle. The impedance data is fitted to an equivalent circuit (inset in **Figure 2.4**) using the supplied software (Zplot 2.8), allowing the membrane resistance ( $R_M$ ) to be extracted when the dimensions of the sample are known.(101, 102) Additional EIS theory and equivalent circuit models are discussed in section 1.5.2.4 for further interpretation of the current-potential performance of fuel cells.

### 2.2.7 Solid-State Electrochemistry

The solid-state electrochemical cell (**Figure 2.5**) was designed in-house, and used to perform experiments at 100 % relative humidity, 30 psi  $O_2$  pressure, and different temperatures. The cell was adapted from work described by Beattie *et al.*(94) and Basura *et al.*(77, 95).



(A)



(B)

Figure 2.5: Schematic diagram (A) and apparatus (B) of the solid-state cell constructed for electrochemical characterization of proton exchange membranes. Working, counter and reference electrodes are denoted: W.E., C.E. and R.E., respectively.(77)

In the solid-state cell there is no aqueous electrolyte. Rather, the humidified PEM provides the medium for protonic transport. The PEM is sandwiched between the working electrode (WE) and the reference electrode (RE). Microelectrodes (100  $\mu\text{m}$  diameter ( $\varnothing$ )) are used to minimize the uncompensated electrolyte resistance when using a solid electrolyte. The use of microelectrodes allows very little current to pass, minimizing the contributions of the  $IR_{\text{electrolyte}}$  uncompensated resistance. The small size of microelectrodes also makes them suitable for measurements on very small volumes.

The schematic drawing in **Figure 2.5(A)** shows the solid-state cell with a 100  $\mu\text{m}$  Pt working electrode (Bioanalytical Systems Inc., (BAS)), horizontally opposed to a dynamic hydrogen reference electrode (DHE) and Pt gauze counter electrode. The electrodes are kept at constant contact pressure via stainless steel springs (3/16 compression Springs, Lawson Inc., USA) and Teflon holders. The membrane of interest is sandwiched between the WE and a Nafion<sup>®</sup> 117 (~5 cm  $\varnothing$ ) backing membrane that completes the connectivity between the RE and CE, both supported in an electronically-isolated Teflon<sup>®</sup> holder. The backing Nafion<sup>®</sup> 117 membrane was pre-treated by boiling (~90 °C for 30 min) in 3 % H<sub>2</sub>O<sub>2</sub>, D.I. H<sub>2</sub>O, 1 M H<sub>2</sub>SO<sub>4</sub> and finally an additional D.I. H<sub>2</sub>O treatment. To ensure complete hydration of the membranes, a filter paper wick was suspended into a beaker of D.I. water below the holder throughout the experiment. The cell was heated with external wrap elements controlled by a K-type thermocouple inside the cell and an external J-Kem Scientific Inc. temperature control unit. Additional insulating wrap was utilized to maintain a steady state temperature of

the cell, especially at the highest operating temperature (60 °C). Reagent grade oxygen or nitrogen humidified gases were supplied to the cell at 30 psi total pressure.

The DHE electrode was fabricated from two 0.25 mm Pt wire tipped glass electrodes (Sand Fire Scientific Inc).(103) Two simultaneous reactions, hydrogen evolution and oxygen evolution, occur at the DHE when it is in contact with the Nafion<sup>®</sup> backing membrane, which serves as the protic medium, and a 100 mA cm<sup>-2</sup> current density is passed through the circuit driven by a 9V battery and resistor load bank. H<sub>2</sub> and O<sub>2</sub> are generated by maintaining a constant voltage of 2 V between the two electrodes, with the typical resistance set at 120 kΩ. The hydrogen evolving electrode was used as the reference electrode. Prior to cell assembly, Pt electrodes were platinized for three hours at -0.2 V vs. the saturated calomel electrode (SCE) in a potassium hexachloroplatinate solution (3 mM), in order to increase their surface area.

The WE was polished and cleaned prior to each cell assembly. The surface was treated using a nitric acid bath (~2min) followed by sonication for 5 min in D.I. water before polishing. The surface of the electrode was polished using 15 (only for initial polishing), 3 and 1 μm aqueous diamond polish mixtures (BAS), and finally with 0.05 μm alumina polish (BAS). The electrode was pre-treated in 1 M H<sub>2</sub>SO<sub>4</sub> by cycling the potential between 1.2 and - 0.2 V vs. SCE for 50 scans at 50 mV s<sup>-1</sup> prior to cell assembly.

The time taken for the cell to reach equilibrium at the initial starting temperature of 30 °C was ~12 hours. Stability was ascertained by monitoring the

fluctuation of the DHE voltage and by cyclic voltammetry (CV). When the deviation in the DHE was less than 5 mV, and the oxygen reduction peak onset in the CV remained at a stable potential, the cell was deemed to be at steady-state equilibrium with the corresponding temperature, pressure and relative humidity. Subsequent temperature increases (10 K increments) were allowed to reach equilibrium over five hours, although equilibrium was often observed before this period.

Following assembly of the solid-state cell with the test membrane, the cell was allowed to equilibrate at the initial temperature of 303 K (30 °C) and pressure of 30 psi (2.04 atm) until the response was stable. Upon reaching stability, cyclic voltammetry, slow sweep voltammetry and chronoamperometry were performed at each temperature from 303 – 323 K in 10 K increments. Following completion of experiments in oxygen, the cell was purged with nitrogen for ~4 hrs at 303 K and pressure of 30 psi before cyclic voltammetry was performed to assess the electrochemically active Pt area.

## **2.3 Results and Discussion**

### **2.3.1 Preparation and Physical Characterization of SPEEK**

#### **2.3.1.1 Preparation of SPEEK**

SPEEK was prepared as described in the experimental section 2.2.2. The ion-exchange capacity of the final SPEEK was adjusted by controlling the duration of the sulfonation reaction. Samples were precipitated from the reaction

solution at 29, 36, and 54 h intervals to yield a series of SPEEK polymers with varying ion exchange capacity.

### **2.3.1.2 Determination of Ion-Exchange Capacity and Proton Conductivity**

IEC is directly proportional to the degree of sulfonation (DS) and has been shown to have a direct influence on membrane properties such as water uptake, swelling, and proton conductivity.<sup>(4, 30, 50, 104)</sup> The IEC of the SPEEK membranes were determined by titration as outlined in 2.2.4, and the water content was determined using equation 2.3. Throughout this work, the IEC of the SPEEK ionomer is designated at the end of the sample name. For example, samples referred to as SPEEK 1.02, SPEEK 1.55, and SPEEK 1.88 possess IECs of 1.02, 1.55, and 1.88 meq g<sup>-1</sup>, respectively. Ion exchange capacities and water contents for SPEEK and Nafion<sup>®</sup> 117 are reported in Table 2.1 together with proton conductivities measured in liquid D.I. water and room temperature (22-23 °C).

Table 2.1: Ion exchange capacity, water content, and proton conductivity for Nafion<sup>®</sup> and SPEEK membranes.

Ionomer	Reaction time h	Ion Exchange Capacity meq g <sup>-1</sup>	Water content at 50 °C %	Proton Conductivity at 22 °C S cm <sup>-1</sup>
Nafion <sup>®</sup> 117	---	0.91 ± 0.04	30 ± 4	0.078 ± 0.008
SPEEK	29	1.02 ± 0.06	20 ± 4	0.0049 ± 0.0005
SPEEK	36	1.55 ± 0.06	32 ± 4	0.023 ± 0.003
SPEEK	54	1.88 ± 0.05	48 ± 6	0.041 ± 0.004

It can be seen that the conductivity of SPEEK increases with IEC, which has been shown to be due to the increased water content in the membrane at higher IEC values.(4, 39, 105) For aromatic membranes, such as SPEEK, the proton conductivity depends much more on the amount of water present in the membrane than in the case of Nafion<sup>®</sup>.(4, 37) Larger water contents are required to create a hydrophilic network for proton transport.(39) However, Xing *et al.*(106) and Kaliaguine *et al.*(39) show there is an upper limit to the water content and thus mechanical strength for hydrocarbon membranes. High levels of hydration lead to excessive swelling, severe dimensional changes, and dramatic losses in mechanical integrity. For this reason, all SPEEK membranes examined were limited to IEC values less than 1.88 meq g<sup>-1</sup>. Membranes having higher IECs were not of sufficient mechanical integrity to be studied in the solid-state electrochemical cell over the entire temperature range.

### **2.3.2 Cyclic Voltammetry at the Pt | Ionomer Interface under N<sub>2</sub> and O<sub>2</sub> Environments**

#### **2.3.2.1 Determination of the Real Electrochemically Active Surface Area**

The real electrochemically active surface area at the Pt | Ionomer electrolyte interface is a required parameter for estimating kinetic and mass transport parameters for solid polymer electrolytes. The exchange current density is implicitly related to the real area of the electrode, rather than the geometric area. The electrochemically active surface area (ESA) was determined by cyclic voltammetry (see section 1.5.2.3), under a nitrogen environment at 100 % relative humidity, 303 K and 30 psi. The potential was

cycled between 0.15 V and 1.5 V vs. DHE for 50 cycles at 50 mV s<sup>-1</sup>. The charge associated with H-adsorption on Pt, illustrated in the cyclic voltammogram in **Figure 2.6**, was determined using the Corrview<sup>®</sup> software after the double layer charge had been subtracted.

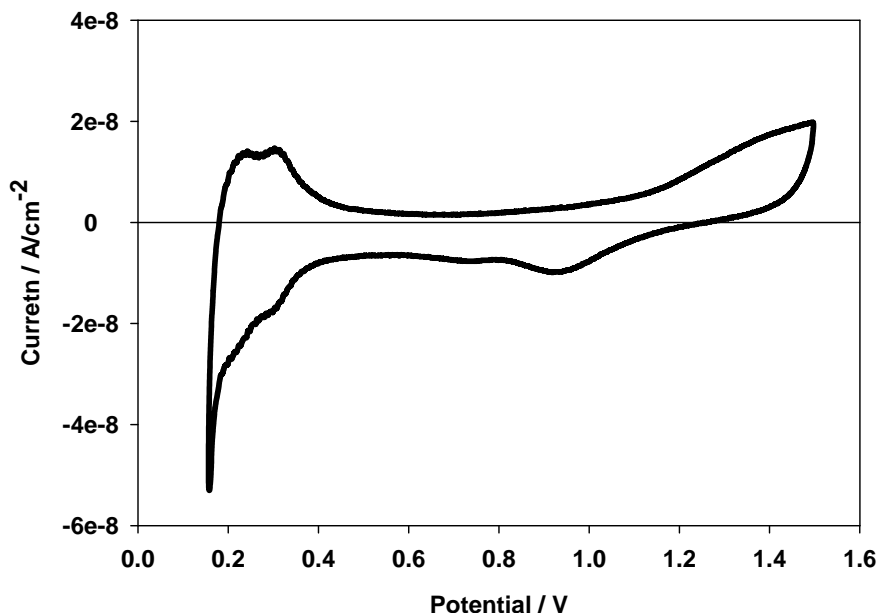


**Figure 2.6:** Cyclic voltammogram of Pt|SPEEK in solid-state cell under nitrogen, 100 % relative humidity, 303 K and 30 psi.

Following determination the electrochemically active area, the roughness factor was calculated by dividing the calculated electrochemically active surface area by the geometrical area ( $\pi r^2$ ) of the electrode (with radius = 50  $\mu\text{m}$ ). The electrochemical surface areas and roughness factors for Pt in contact with both Nafion<sup>®</sup> and SPEEK membranes can be seen in Table 2.2. The roughness factors attained for the microelectrode in this study are comparable to those seen

by Beattie *et al.*(94) and Parthasarathy *et al.*(78, 91) and demonstrate that there is acceptable contact between the solid electrolyte and Pt in the solid-state cell.

Table 2.2: Geometric area, real area and roughness factor for the solid-state Pt microelectrode | Ionomer interface.

Pt   Ionomer interface	Geometric area (cm <sup>2</sup> ) X 10 <sup>5</sup>	Pt - H <sub>ads</sub> charge (C/cm <sup>2</sup> ) X 10 <sup>8</sup>	Real area (cm <sup>2</sup> ) X 10 <sup>4</sup>	Electrode roughness
Pt   Nafion <sup>®</sup> 117 (94)	7.85	---	2.11	2.7
Pt   Nafion <sup>®</sup> 117	7.85	3.82 ± 0.4	1.72 ± 0.1	2.3 ± 0.2
Pt   SPEEK 1.02	7.85	3.49 ± 0.3	1.66 ± 0.1	2.1 ± 0.2
Pt   SPEEK 1.55	7.85	3.59 ± 0.3	1.71 ± 0.1	2.2 ± 0.2
Pt   SPEEK 1.88	7.85	3.55 ± 0.3	1.68 ± 0.1	2.1 ± 0.2

To illustrate the effect from differing potential sweep scan rates, cyclic voltammograms for a Pt | SPEEK 1.88 polymer interface in the presence of pure oxygen at 303 K, 100 % RH and 30 psi are represented in **Figure 2.7** for 5 and 50  $\text{mV s}^{-1}$ . The mass transport limited oxygen reduction current at slow sweep rate (dashed line), 5  $\text{mV s}^{-1}$ , is clearly seen for the oxygen-saturated ionomer. The CV scan at 50  $\text{mV s}^{-1}$  (solid) in the same environment shows typical voltammetric behaviour.

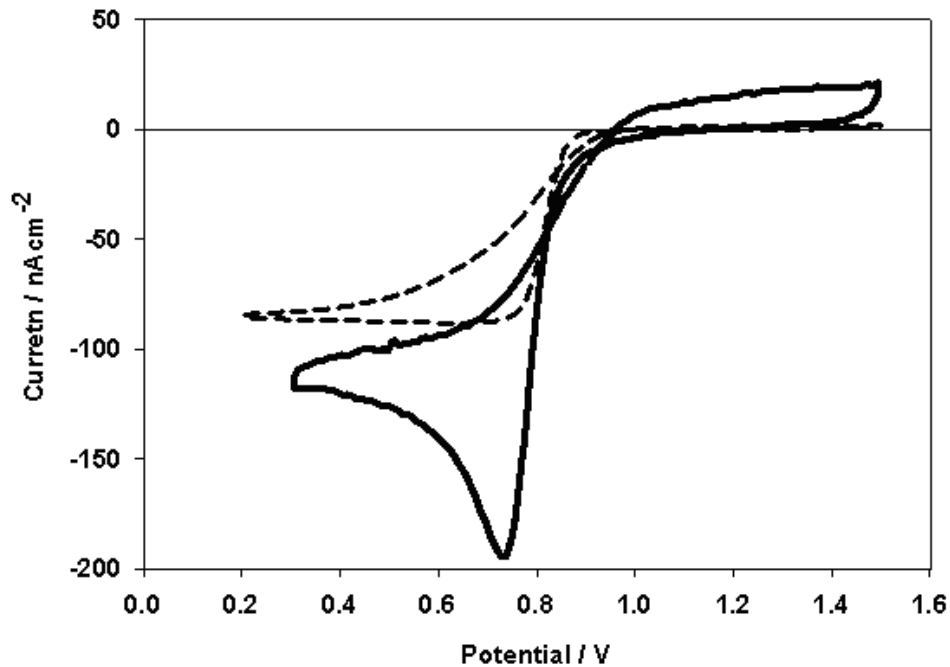


**Figure 2.7:** Cyclic voltammograms for oxygen reduction at a Pt | SPEEK 1.88 membrane interface at 303 K, 100% RH and 30 psi oxygen at 50  $\text{mV s}^{-1}$  (solid) and 5  $\text{mV s}^{-1}$  scan rate (dashed).

### 2.3.2.2 Stability of the Dynamic Hydrogen Reference Electrode

The stability of the dynamic hydrogen electrode (DHE) was monitored by observing the position of the oxygen reduction peak, onset at  $\sim 0.8$  V vs. DHE, for

cyclic voltammograms obtained at each temperature. No significant shift in the peak positions were observed with increasing temperature, indicating that the potential of the DHE electrode remained stable over the temperature ranges studied. Monitoring of the DHE multi-meter showed a deviation on the order of  $\pm 2$  mV, which is an acceptable deviation and accounted for in the error analysis of the data.

### **2.3.3 O<sub>2</sub> Mass Transport Parameters for Nafion<sup>®</sup> 117 and SPEEK possessing different IECs**

The oxygen diffusion coefficient and oxygen solubility were determined for Nafion<sup>®</sup> 117 and a series of SPEEK membranes with IEC values 1.02, 1.55 and 1.88 meq g<sup>-1</sup> (i.e., SPEEK 1.02, SPEEK 1.55, and SPEEK 1.88). **Figure 2.8** shows slow-sweep voltammograms for Nafion<sup>®</sup> 117 and SPEEK membranes. A scan rate of 5 mV s<sup>-1</sup> produced current potential curves with a well-defined plateau (only the forward sweep is shown for clarity). From this, it is found that the diffusion limited current,  $I_d$ , at the Pt | SPEEK ionomer interface is significantly lower than the  $I_d$  determined at the Pt | Nafion<sup>®</sup> interface.  $I_d$  is also dependent on the IEC of SPEEK, with higher IECs resulting in larger limiting currents.

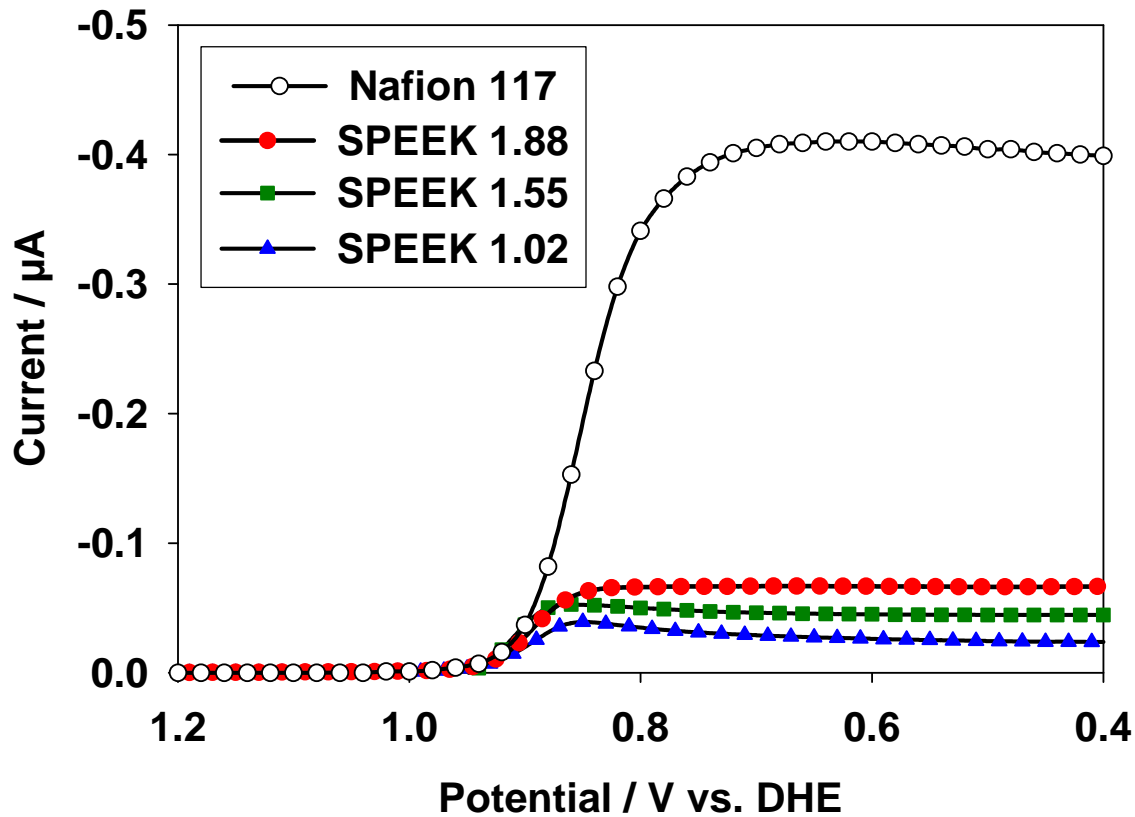


Figure 2.8: Slow-Sweep voltammetry of Nafion<sup>®</sup> 117 and SPEEK at 303 K, 30 psi oxygen and 100% RH. Nafion 117 ( $\circ$ ), SPEEK 1.02 ( $\blacktriangle$ ), SPEEK 1.55 ( $\blacksquare$ ), and SPEEK 1.88 ( $\bullet$ ).

Chronoamperometric analysis of ORR in SPEEK at 303 K, 100 % RH and 30 psi oxygen can be seen in **Figure 2.9**, and subsequent plots of  $I$  vs.  $t^{-1/2}$  for the oxygen reduction are linear between 0.5 and 5 s as shown in **Figure 2.10**.

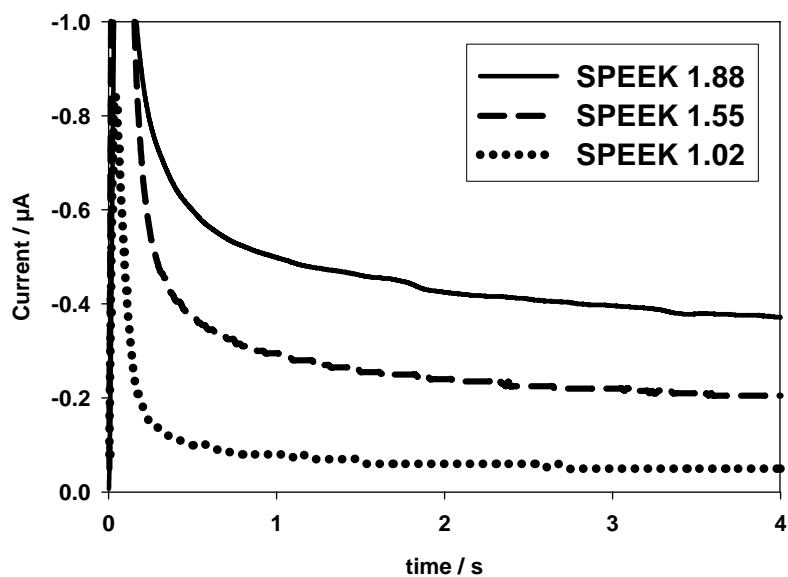


Figure 2.9: Chronoamperograms for  $O_2$  reduction at a Pt | SPEEK membrane interface for SPEEK 1.02 (solid), SPEEK 1.55(dashed), and SPEEK 1.88 (dotted) at 303 K, 30 psi oxygen and 100% RH.

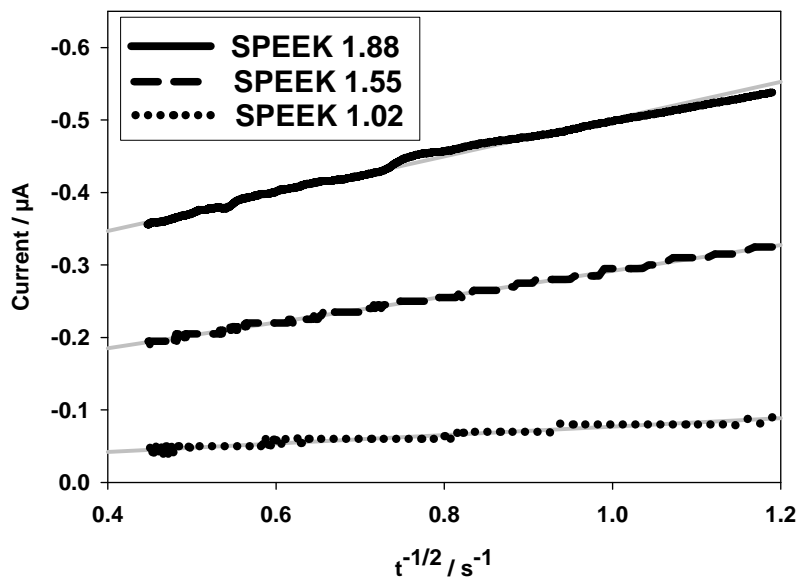


Figure 2.10: Plots of  $I$  vs.  $t^{-1/2}$  for a chronoamperometric step from 1.2 to 0.4 V for SPEEK 1.02 (solid), SPEEK 1.55 (dashed), and SPEEK 1.88 (dotted) at 303 K, 30 psi oxygen and 100% RH.

The oxygen diffusion coefficient,  $D_b$ , and oxygen solubility,  $c_b$ , were obtained from the linear plots using regression analysis (shown as the grey lines in **Figure 2.10**). Oxygen permeability is the product  $D_b c_b$ , and is given in Table 2.3, together with the oxygen diffusion coefficient,  $D_b$ , and solubility,  $c_b$ .

**Table 2.3: Oxygen mass transport parameters for Nafion<sup>®</sup> 117 and SPEEK ionomers of varying IEC from chronoamperometry at 303 K, 100 % RH and 30 psi oxygen.**

<b>Ionomer IEC</b>	<b>Diffusion coefficient <math>D_b</math> (cm<sup>2</sup> s<sup>-1</sup>)  x 10<sup>6</sup></b>	<b>Solubility <math>c_b</math> (mol cm<sup>-3</sup>)  x 10<sup>6</sup></b>	<b>Permeability <math>D_b c_b</math> (mol cm<sup>-2</sup> s<sup>-1</sup>)  x 10<sup>12</sup></b>
<b>Pt   Nafion<sup>®</sup> 117 (this work)</b>			
<b>0.9</b>	4.54 ± 0.4	11.7 ± 0.9	53.1 ± 6.4
<b>Pt   Nafion<sup>®</sup> 117 (77)</b>			
<b>0.9</b>	5.96	9.19	54.8
<b>Pt   SPEEK</b>			
<b>1.02</b>	0.83 ± 0.03	6.09 ± 0.47	5.04 ± 0.61
<b>1.55</b>	3.24 ± 0.28	2.09 ± 0.18	6.76 ± 0.81
<b>1.88</b>	7.23 ± 0.57	1.20 ± 0.09	8.65 ± 1.03

A significant difference in oxygen permeability is observed for Nafion<sup>®</sup> and SPEEK membranes. At the same operational temperature, SPEEK membranes exhibit ~6 to 10 times lower oxygen permeability than Nafion<sup>®</sup>. This result is due to different diffusion and solubility coefficients of oxygen. The variation of  $D_b$ ,  $c_b$  and  $D_b c_b$  values with IEC are shown in **Figures 2.11, 2.12 and 2.13**.

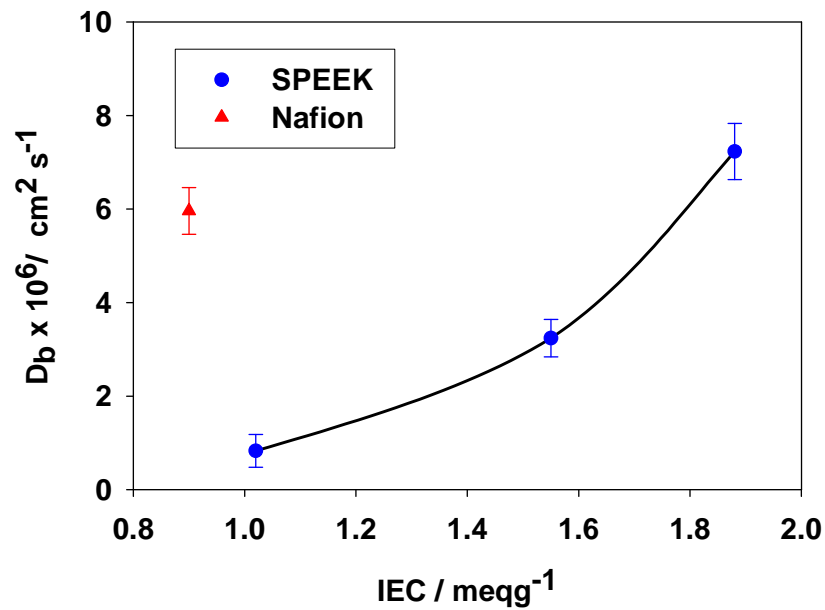


**Figure 2.11: Oxygen diffusion coefficient for Nafion<sup>®</sup> and SPEEK membranes as a function of IEC at 303 K, 30 psi oxygen and 100% RH.**

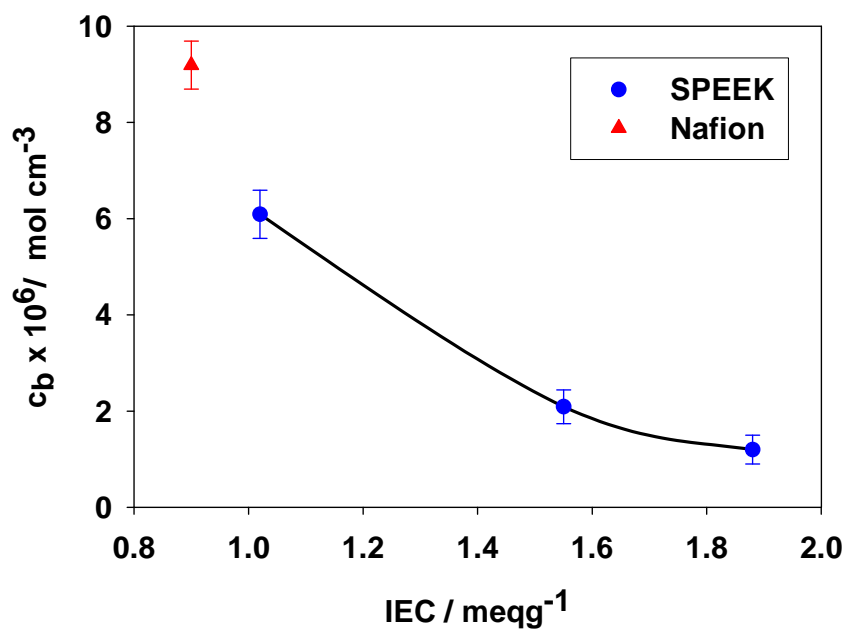


Figure 2.12: Oxygen solubility for Nafion<sup>®</sup> and SPEEK membranes as a function of IEC at 303 K, 30 psi oxygen and 100% RH.

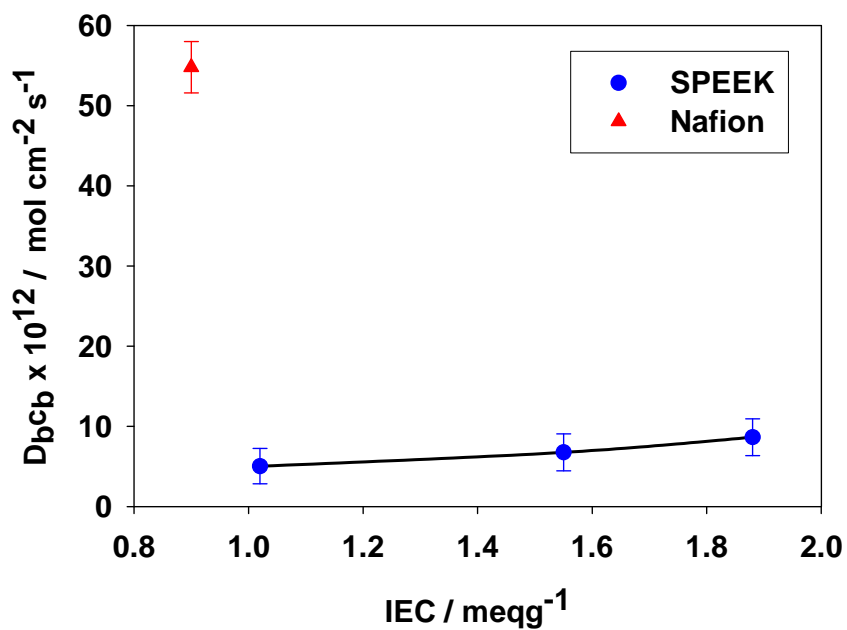


Figure 2.13: Oxygen permeability for Nafion<sup>®</sup> and SPEEK membranes as a function of IEC at 303 K, 30 psi oxygen and 100% RH.

**Figure 2.11** illustrates the large dependence of  $D_b$  on IEC for the SPEEK membranes, which can be explained on the basis of the increasing water content with increasing IEC. Water sorption increases with IEC due to the hydrophilicity of the sulfonic group.(4, 93) Buchi *et al.*(93) showed supporting evidence that membranes with high IECs and a high water uptake exhibit larger oxygen diffusion coefficients since oxygen diffusion is faster in aqueous domains compared to the hydrophobic perfluorinated backbone regions of Nafion<sup>®</sup>. SPEEK membranes possessing high IEC and significantly higher water contents (48 %) compared to Nafion<sup>®</sup> (30 %) showed higher oxygen diffusion coefficients,  $7.23 \times 10^{-6} \text{ cm}^2 \text{ s}^{-1}$ , compared to Nafion<sup>®</sup> ( $5.26 \times 10^{-6} \text{ cm}^2 \text{ s}^{-1}$ ). Zhang *et al.*(43, 90) also supports the dependence of water uptake and IEC on increased oxygen transport for a series of non-fluorinated sulfonated poly(arylene ether sulfone) (SPES) and sulfonated poly(phenylene sulfide sulfone) (SPSS) polymer electrolytes. In addition, Zhang *et al.*(43, 90) states that the chemical composition of the membrane is a major determinant in the observed mass transport properties due to a less pronounced hydrophobic-hydrophilic nano-phase segregation compared to perfluorinated ionomers. Experimental evidence for SPEEK supports this assertion, wherein oxygen permeability in SPEEK is much lower than in Nafion<sup>®</sup>.

**Figure 2.12** shows that oxygen solubility in SPEEK membranes is consistently lower than in Nafion<sup>®</sup> 117 for all SPEEK IECs, which can be rationalized by the fact that oxygen is more soluble in perfluorinated ( $-\text{CF}_2\text{CF}_2-$ ) materials than hydrocarbon materials.(91, 107) The low oxygen solubility in

hydrocarbon membranes was also reported by Zhang *et al.*(90) for sulfonated poly(arylene ether sulfone) membranes having IECs similar to those described in this work (1.5 - 2.2 meq g<sup>-1</sup>). Similar trends have been observed for perfluorinated membranes, where oxygen solubility is found to be greater in fluorocarbon regions and greater in membranes that contain lower water contents.(108)

Although the permeability of O<sub>2</sub> in SPEEK increases with increasing IEC, as observed in **Figure 2.13**, the resulting oxygen permeability for all SPEEK membranes examined is lower compared to Nafion<sup>®</sup> 117. Since the oxygen diffusion coefficients are not dissimilar, the substantially lower permeability is largely due to the considerably lower oxygen solubility in SPEEK membranes, which in turn is a result of the absence of fluorinated regions and/or the presence of high water contents.

#### **2.3.4 O<sub>2</sub> Mass Transport Parameters for Nafion<sup>®</sup> 117 and SPEEK 1.88 as a Function of Temperature**

The oxygen diffusion coefficient, oxygen solubility and permeability were determined for Nafion<sup>®</sup> 117 and SPEEK 1.88 for varying operating temperatures. **Figure 2.14** and **Figure 2.15** illustrate the  $I$  vs.  $t^{-1/2}$  plots for oxygen reduction in Nafion<sup>®</sup> and SPEEK 1.88 at temperatures 303 to 323 K, 100 % RH and 30 psi oxygen.

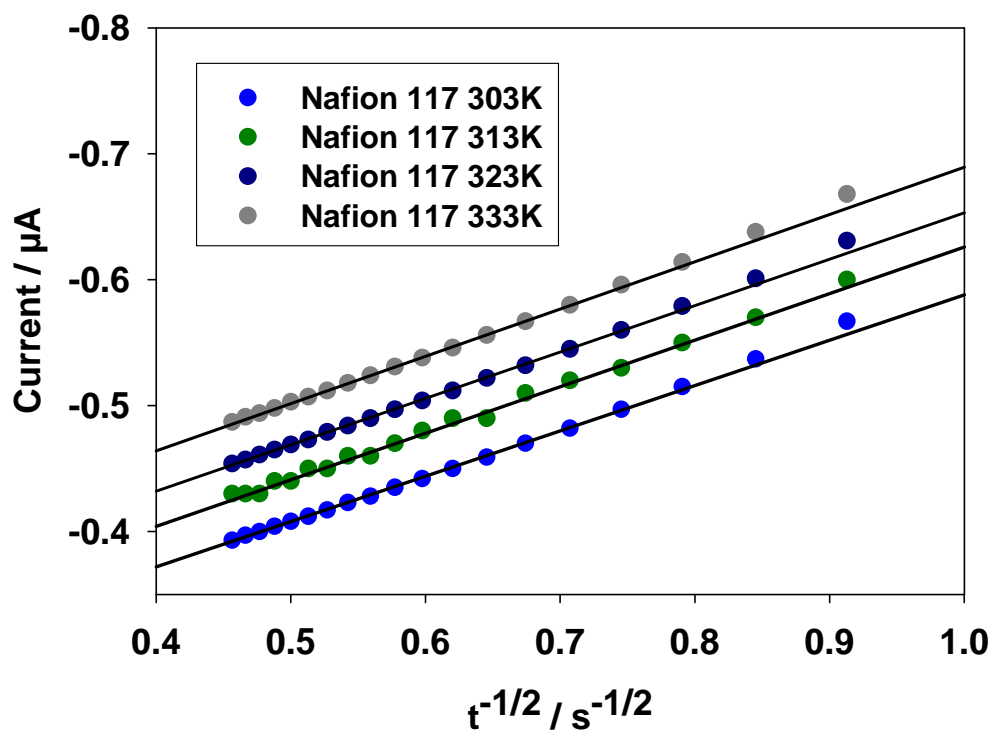


Figure 2.14: Linear plots of  $i$  vs.  $t^{-1/2}$  for a chronoamperometric step from 1.2 to 0.4 V for Pt|Nafion<sup>®</sup> 117 between 0.5 and 5 s at different temperatures (303 – 323 K), 30 psi oxygen and 100% RH.

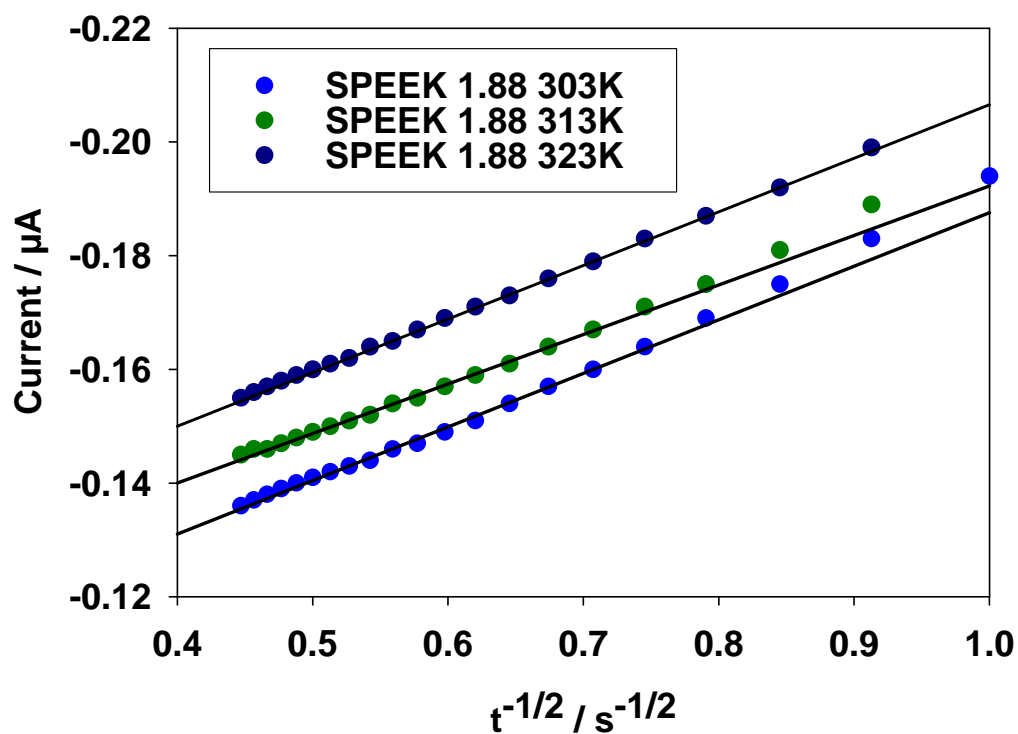


Figure 2.15: Linear plots of  $i$  vs.  $t^{-1/2}$  for a chronoamperometric step from 1.2 to 0.4 V for Pt | SPEEK 1.88 between 0.5 and 5 s at different temperatures (303 – 323 K), 30 psi oxygen and 100% RH.

The limiting current for oxygen reduction, oxygen diffusion coefficient,  $D_b$ , oxygen solubility,  $c_b$ , and oxygen permeability in Nafion<sup>®</sup> 117 and SPEEK 1.88 ionomers at different temperatures are given in Table 2.4.

**Table 2.4: Mass transport parameters for Nafion<sup>®</sup> 117 and SPEEK 1.88 for the temperature range 303–323 K, 100 % RH and 30 psi oxygen.**

<b>Temperature</b> <b>K</b>	<b>Limiting</b> <b>Current</b> <b>nA</b>	<b><math>D_b</math></b> <b>(<math>\text{cm}^2 \text{s}^{-1}</math>)</b> <b><math>\times 10^6</math></b>	<b><math>c_b</math></b> <b>(<math>\text{mol cm}^{-3}</math>)</b> <b><math>\times 10^6</math></b>	<b><math>D_b c_b</math></b> <b>(<math>\text{mol cm}^{-2} \text{s}^{-1}</math>)</b> <b><math>\times 10^{12}</math></b>
<b>Pt   Nafion<sup>®</sup> 117</b>				
<b>303</b>	329 ± 8	3.09 ± 0.21	13.8 ± 0.9	42.6 ± 2.6
<b>313</b>	347 ± 9	3.86 ± 0.27	11.6 ± 0.8	44.9 ± 2.5
<b>323</b>	381 ± 11	4.74 ± 0.34	10.4 ± 0.7	49.3 ± 2.8
<b>Pt   SPEEK 1.88</b>				
<b>303</b>	120 ± 10	8.01 ± 0.56	1.15 ± 0.09	9.24 ± 0.95
<b>313</b>	131 ± 9	11.0 ± 0.6	1.06 ± 0.08	11.8 ± 0.9
<b>323</b>	143 ± 10	11.3 ± 0.8	1.05 ± 0.08	11.9 ± 0.8

The temperature dependence of O<sub>2</sub> mass transport parameters followed the same trend for both of the membranes studied, with the oxygen diffusion coefficient increasing, and the oxygen solubility decreasing with increasing temperature. In addition to the expected increase in diffusion of molecules with temperature, an increase in temperature is believed to enhance the motion of

polymer segments, in turn increasing the free volume within the polymer. These trends are the same as those found by Beattie *et al.*(94) and Zhang *et al.*(96), who reported increasing oxygen diffusion coefficients and decreasing solubilities with increasing temperature for Nafion<sup>®</sup> 117. Beattie *et al.*(94) reported  $D_b$  values between  $5.96 \times 10^6$  to  $9.09 \times 10^6 \text{ cm}^2 \text{ s}^{-1}$  and  $c_b$  values between  $9.19 \times 10^6$  to  $8.20 \times 10^6 \text{ mol cm}^{-3}$  for Nafion<sup>®</sup> 117 at 3 atm (44 psi) oxygen, and Zhang *et al.*(96) reported values  $3.03 \times 10^6$  to  $5.50 \times 10^6 \text{ cm}^2 \text{ s}^{-1}$  for  $D_b$  and  $11.24 \times 10^6$  to  $9.42 \times 10^6 \text{ mol cm}^{-3}$  for  $c_b$  at 3 atm (44 psi) oxygen over a similar temperature range used in the present work. The  $D_b$  values in the present study are  $3.09 \times 10^6$  to  $4.74 \times 10^6 \text{ cm}^2 \text{ s}^{-1}$  and the  $c_b$  values are  $13.8 \times 10^6$  to  $10.4 \times 10^6 \text{ mol cm}^{-3}$  at 30 psi (2.04 atm) oxygen pressure. These data lie within the same order of magnitude as those reported by Zhang *et al.*(96) and Beattie *et al.*(94) after differences in oxygen pressure are accounted for.

### **2.3.5 Evaluation of ORR Kinetics at Pt | Nafion<sup>®</sup> 117 and Pt | SPEEK 1.88 interfaces as a Function of Temperature**

ORR kinetic parameters of exchange current density, Tafel slopes and  $\alpha$  coefficients at Pt | Nafion<sup>®</sup> 117 and Pt | SPEEK 1.88 interfaces at different operating temperatures (303 – 323 K) were determined using slow-sweep voltammetry performed between 1.2 and 0.3 V (vs. DHE) at a scan rate of  $5 \text{ mV s}^{-1}$ . The voltammograms shown are the forward scan of the last of ten successive scans for each membrane and temperature. Voltammograms obtained for Nafion<sup>®</sup> 117 and SPEEK 1.88 at different cell temperatures, 100 % RH and 30 psi oxygen are represented in **Figure 2.16** and **Figure 2.17**.

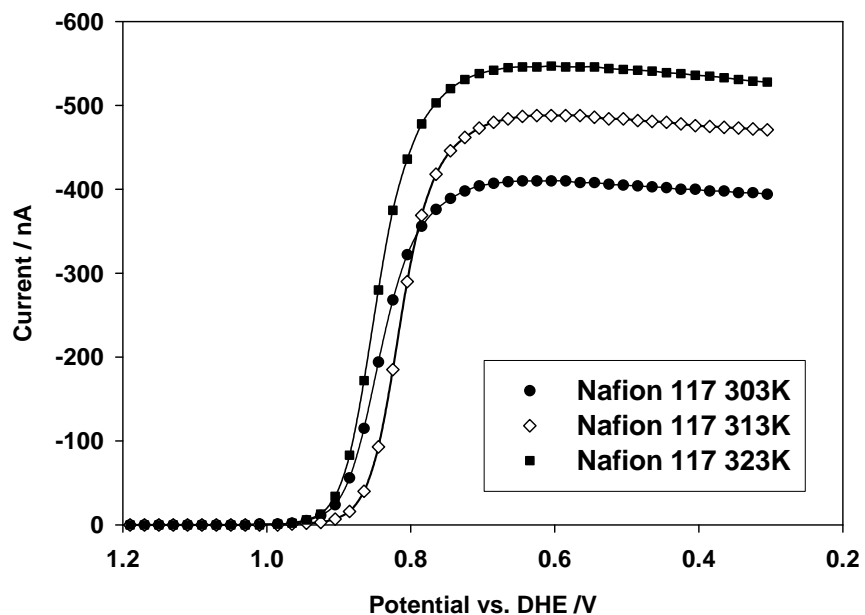


Figure 2.16: Slow-sweep voltammograms for  $O_2$  reduction at the Pt | Nafion<sup>®</sup> 117 for the temperature range 303–323 K, 30 psi  $O_2$ , and a scan rate of  $5 \text{ mV s}^{-1}$ .

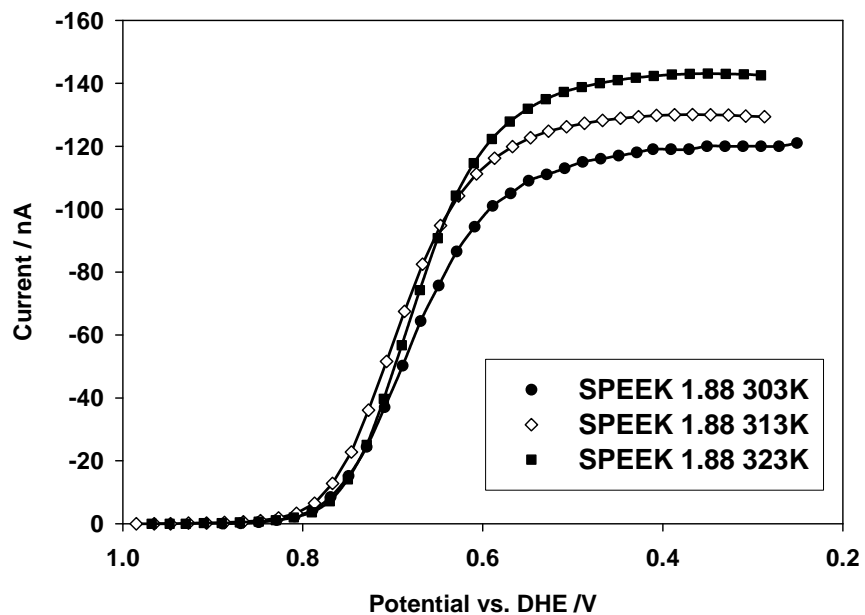


Figure 2.17: Slow-sweep voltammograms for  $O_2$  reduction at the Pt | SPEEK 1.88 for the temperature range 303–323 K, 30 psi  $O_2$ , and a scan rate of  $5 \text{ mV s}^{-1}$ .

From these plots, it is evident that  $I_d$  observed at the Pt|Nafion<sup>®</sup> 117 and Pt|SPEEK 1.88 interfaces increase with temperature, with Nafion<sup>®</sup> exhibiting a significantly higher limiting current, as reported in Table 2.4. For a meaningful estimation of the ORR kinetic parameters, a correction in potential must be applied to account for difference between the DHE reference electrode and the standard hydrogen electrode (SHE). In the solid-state cell, the DHE was found to be  $-80 \pm 12$  mV vs. SHE. The experimental error of  $\pm 12$  mV was the maximum deviation in potential observed over the entire study of membranes and temperatures. Typically, the fluctuation in the DHE was minimal and was in the range of  $\pm 3$  mV. While the use of a DHE results in a stable reference electrode potential, a potential correction of +80 mV to the theoretical reversible potential for oxygen reduction,  $E_r$ , was employed. The significance of this correction has been noted by Beattie *et al.*(94), as neglecting it leads to an overestimation of the exchange current density.

Exchange current densities,  $j_d$ , Tafel slopes, and  $\alpha$  transfer coefficients were calculated from the slow-sweep voltammetry data using a mass transfer corrected Tafel equation (equation 1.20). For each O<sub>2</sub> reduction wave shown in **Figure 2.16** and **Figure 2.17**, the working electrode potential (E) was plotted versus  $\log [(j_d)/(j_d - j)]$  as seen in **Figure 2.18** and **Figure 2.19**.

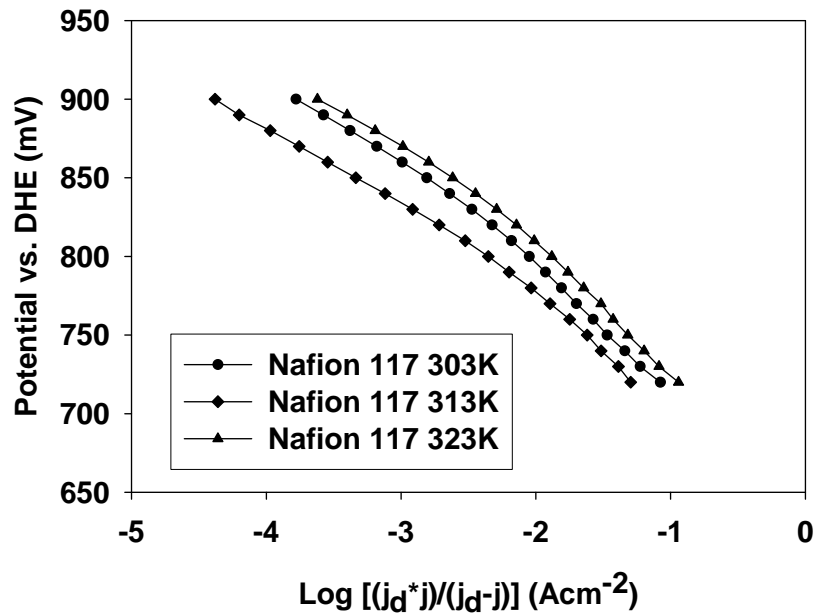


Figure 2.18: Mass-transport corrected Tafel plots for Nafion<sup>®</sup> 117 for the temperature range 303 – 323 K. 30 psi O<sub>2</sub> pressure and 100% RH.

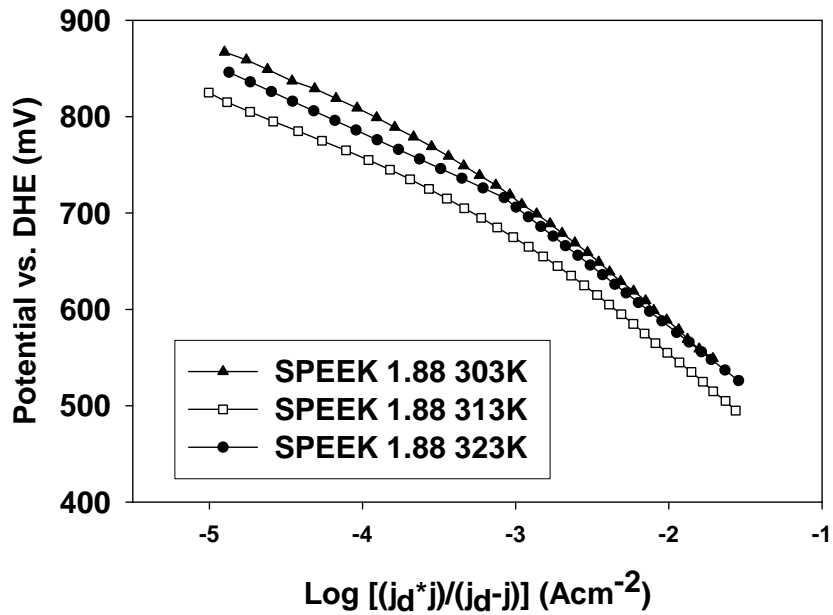


Figure 2.19: Mass-transport corrected Tafel plots for SPEEK 1.88 for the temperature range 303 – 323 K. 30 psi O<sub>2</sub> pressure and 100% RH.

From these plots the exchange current density for oxygen reduction can be calculated by extrapolation of the linear portions of the Tafel plots to the theoretical reversible potential,  $E_{r,pr}$ .  $E_{t,pr}$  is the standard electrode potential,  $E^\circ$ , for oxygen reduction (1.229 V versus SHE, at 298 K and 1 atm  $O_2$  pressure), corrected for temperature and  $O_2$  pressure according to the following methodology presented by Parthasarathy *et al.*(78, 79) and outlined in equations 2.5, 2.6 and 2.7,

$$\Delta G^\circ = -70650 - 8.0T \ln T + 92.84T \quad (2.5)$$

where  $\Delta G^\circ$  is the standard free energy of formation,  $\Delta G^\circ$  (cal mol<sup>-1</sup>), of one mole of water at the required temperature.(7) When  $\Delta G^\circ$  is known, the reversible potential for oxygen reduction,  $E_r$ , can be calculated by equation 2.6,(79)

$$E_r = -\Delta G^\circ/nF \quad (2.6)$$

where n is equal to 2 for one mole of water in the oxygen reduction reaction. Lastly, the reversible potential must be corrected for the oxygen pressure,  $E_{r,pr}$ , using the Nernst relation below,(7)

$$E_r = E_r + (RT/4F)\ln P_{O_2} \quad (2.7)$$

where  $P_{O_2}$  is the pressure of oxygen, corrected for the saturation vapour pressure of water (0.122 atm. at 323 K (6)).

ORR mass transport-corrected Tafel plots exhibiting two linear Tafel regions are shown in **Figure 2.18** and **Figure 2.19** for Nafion<sup>®</sup> 117 and SPEEK 1.88. The presence of dual Tafel slopes has been reported by Damjanovic *et al.*(109) for Pt in acidic aqueous electrolytes and also by Parthasarathy *et al.*(91)

for Pt|Ionomer microelectrode interfaces. It is reasoned that dual Tafel slopes result because the kinetics and mechanism of oxygen reduction on oxide-free Pt are different from that reported on an oxide-covered Pt (potentials above 1 V). Between 1 V and 0.6 V, oxygen-containing species are adsorbed on oxide-free Pt. A consequence of this is that O<sub>2</sub> reduction on Pt electrode may occur either on oxide-covered or oxide-free surfaces. The mechanism and kinetics of O<sub>2</sub> reduction may differ significantly for these two types of surfaces.(109) Damjanovic *et al.*(17) has shown that in acidic solutions, the first rate-controlling electrochemical step of the oxygen reduction mechanism on oxide-free Pt involves O<sub>2</sub> adsorption under Temkin conditions. Temkin conditions are associated with a high coverage of adsorbed oxygen-containing species, and should exhibit a symmetry factor,  $\alpha$ , of 1 and a Tafel slope of  $-60 \text{ mV decade}^{-1}$  ( $-2.303RT/\alpha nF$ ). However, Temkin conditions only occur in a narrow potential window, since, as the rate of the reaction increases, coverage by reaction intermediates decreases, eventually reaching the level at which Langmuirian conditions become predominant. At higher reaction rates and current densities, when the coverage of oxygen-containing species is low, Langmuir conditions become the mechanism-controlling factor and a characteristic slope of  $-120 \text{ mV decade}^{-1}$  ( $\alpha = 1/2$ ) is expected, and with it a significant change in the kinetic parameters for oxygen reduction. Despite the change in Tafel slopes, the first charge transfer rate determining step (RDS) is the same in both the low and the high current density regions, corresponding to the one-electron transfer reaction shown in equation 2.18.



The change in the kinetic mechanism is evident in the Tafel slopes of **Figure 2.18** and **Figure 2.19**, where the slopes for Nafion<sup>®</sup> 117 and SPEEK 1.88 reflect these kinetic changes. Tafel parameters corresponding to each temperature and membrane are listed in Table 2.5. They include the corrected reversible potential for oxygen reduction,  $E_{r,pr}$ , the Tafel slopes for both the low and high current density range, the transfer coefficient alpha,  $\alpha$ , associated with each slope and the exchange current densities,  $j_o$ , for each range.

Table 2.5: Electrode kinetic parameters for Nafion<sup>®</sup> 117 and SPEEK 1.88 interfaces as a function of temperature 303–323 K, 100 % RH, and 30 psi O<sub>2</sub>.

Temperature K	E <sub>r,pr</sub> mV vs. SHE	Slope (lcd) mV	j <sub>o</sub> (lcd) A cm <sup>-2</sup>	alpha	Slope (hcd) mV	j <sub>o</sub> (hcd) A cm <sup>-2</sup>	alpha
<b>SPEEK 1.88</b>							
<b>303</b>	1309	-73.2	(5.7 ± 1.4) × 10 <sup>-11</sup>	0.81	-125.7	(4.7 ± 1.3) × 10 <sup>-8</sup>	0.47
<b>313</b>	1301	-72.4	(3.4 ± 1.1) × 10 <sup>-11</sup>	0.81	-123.1	(8.3 ± 1.7) × 10 <sup>-8</sup>	0.48
<b>323</b>	1292	-72.1	(6.8 ± 1.5) × 10 <sup>-11</sup>	0.82	-122.3	(7.4 ± 1.8) × 10 <sup>-8</sup>	0.48
<b>Nafion<sup>®</sup> 117</b>							
<b>303</b>	1309	-55.1	(1.8 ± 1.0) × 10 <sup>-10</sup>	1.08	-83.4	(5.7 ± 1.5) × 10 <sup>-8</sup>	0.71
<b>313</b>	1301	-54.3	(1.3 ± 1.0) × 10 <sup>-10</sup>	1.10	-79.7	(2.3 ± 1.3) × 10 <sup>-8</sup>	0.75
<b>323</b>	1292	-56.2	(1.1 ± 1.0) × 10 <sup>-9</sup>	1.06	-85.5	(1.8 ± 1.3) × 10 <sup>-7</sup>	0.70
<b>Nafion<sup>®</sup> 117 (94)</b>							
<b>323</b>	1292	-58.1	4.44 × 10 <sup>-11</sup>	1.02	-94.6	6.37 × 10 <sup>-8</sup>	0.63

The slopes at low current density (lcd) are  $-55$  and  $-72$   $\text{mV dec}^{-1}$  for Nafion<sup>®</sup> 117 and SPEEK 1.88, respectively, and the slopes at high current density (hcd) are correspondingly  $-84$  and  $-122$   $\text{mV dec}^{-1}$ . Compared to the theoretical slopes presented by Damjanovic *et al.*(17, 109) of  $-60$   $\text{mV dec}^{-1}$  ( $-RT/F$ ) and  $-120$   $\text{mV dec}^{-1}$  ( $-2RT/F$ ) for Pt-oxide and Pt-oxide free surfaces, the Nafion<sup>®</sup> 117 and SPEEK 1.88 data reflects the change in kinetic mechanism but shows a deviation from the theoretical values. Further, the transfer coefficients  $\alpha$  for Nafion<sup>®</sup> 117 and SPEEK 1.88 also exhibit a deviation from the characteristic values of 1 (lcd) and 0.5 (hcd).(91, 94) At present the source of these deviations is not known. A similar result was reported by Beattie *et al.*(94) and explained to be due to impurities in the membrane and possible differences in the membrane pre-treatment. Such deviations of the Tafel parameters from typical values are inherent in these measurements, as is evident from the similar results for Nafion<sup>®</sup> 117 reported by Basura *et al.*(77), Beattie *et al.*(94) and Zhang *et al.*(96). The exact cause is complex and difficult to control. A future consideration in correcting the experimental data with respect to the electronic contact resistance in the cell, determined from electrochemical impedance spectroscopy, may allow a more accurate interpretation of the kinetic differences between varying solid polymer electrolytes.

Tafel plot data for SPEEK membranes also demonstrate the two linear regions observed for Nafion<sup>®</sup>, but possess larger kinetic limitations as evidenced by the larger Tafel slopes,  $-72$   $\text{mV (decade)}^{-1}$  (lcd) and  $-122$   $\text{mV (decade)}^{-1}$  (hcd). Beattie *et al.*(94) reasoned that the kinetic parameters obtained at low current

density should be used when comparing different materials as the change in Tafel slope upon going from low to high current density is dependent on the length of time of anodic pre-treatment of the Pt surface. The low current density region is unaffected by electrode pre-treatment, and thus, provides a more accurate means for comparing Nafion<sup>®</sup> and SPEEK 1.88 kinetic parameters. The exchange current densities in the low current density regime are  $1.1 \times 10^{-9} \text{ A cm}^{-2}$  and  $6.8 \times 10^{-11} \text{ A cm}^{-2}$  at 50 °C, for Nafion and SPEEK, respectively. Thus, the rate of ORR is faster at the Pt|Nafion<sup>®</sup> interface. The lower exchange current density for SPEEK and larger Tafel slope will result in larger kinetic limitations when used in fuel cell cathodes. This prediction is realized and demonstrated in Chapter 4 where fuel cell polarization data are discussed.

## 2.4 Conclusion

The effects of ion exchange capacity on the electrochemical reduction of oxygen at a Pt|PEM interface was investigated using chronoamperometry and slow-sweep voltammetry and a solid state electrochemical cell that mimics a fuel cell environment. The effect of increasing temperature on limiting current, oxygen diffusion, oxygen solubility and oxygen permeability for SPEEK membranes was also investigated.

Oxygen diffusion coefficients,  $D_b$ , increased with increasing IEC for SPEEK membranes due to larger water content in the membrane, while oxygen solubilities,  $c_b$ , decreased with increasing IEC due to reduced hydrophobic character. The ORR limiting current and oxygen permeability in SPEEK

membranes increased with IEC. However, compared to Nafion<sup>®</sup> 117, the values for limiting current were significantly lower for all IEC SPEEK membranes due to the significantly reduced solubility of oxygen.

For both Nafion<sup>®</sup> 117 and SPEEK 1.88 membranes, the oxygen diffusion coefficient,  $D_b$ , increased with increasing temperature, while oxygen solubility,  $c_b$ , decreased with increasing temperature. Mass transport properties for SPEEK electrolytes were significantly different to Nafion<sup>®</sup> 117. It was found that SPEEK possessed  $D_b$  values higher than Nafion<sup>®</sup> 117 due to the large water content but  $c_b$  values were considerably lower than Nafion<sup>®</sup> 117 due to the non-fluorinated hydrocarbon backbone of SPEEK. The magnitude of the differences in  $D_b$  and  $c_b$  resulted in the oxygen permeability in SPEEK being four to six times lower than in Nafion<sup>®</sup> 117, for a given temperature.

ORR kinetic parameters (Tafel slope, transfer coefficient, and exchange current density) were obtained for Pt|Nafion<sup>®</sup> 117 and Pt|SPEEK interfaces. Comparing the Tafel plots, both membranes are characterized by two slopes, corresponding to oxide-covered and oxide-free Pt. A higher exchange current density for ORR was observed in Nafion<sup>®</sup> 117, leading to inherently faster rates of electrochemical reaction.

## CHAPTER 3: MICROSTRUCTURAL ANALYSIS OF NAFION<sup>®</sup>- AND SPEEK-BASED CATALYST LAYERS

### 3.1 Introduction

In order to maximize the efficiency of the cathode, the microstructure of the catalyst layer must be optimized to produce an ionic pathway for protons that extends the triple phase reaction region. Additionally, the catalyst layer must have a low barrier to O<sub>2</sub> permeation, high electronic connectivity, provide optimal distribution of reactant gases, and have a porous structure suitable for removal of liquid water.(20, 53) Satisfying the above conditions for the catalyst layer is accomplished through careful consideration of the volume of conducting media required by each phase and the distribution of the respective conducting networks dictated by the fabrication conditions and techniques.

Past studies by Uchida *et al.*(110), Fournier *et al.*(111) and Gode *et al.*(70) illustrate the numerous degrees of freedom associated within catalyst layer fabrication and the diverse resulting microstructures attainable. In these studies, the use of scanning electron microscopy, together with gas and mercury porosimetry, allowed the nature of the solvent, the amount of Pt on carbon, the type of carbon, the relative amount of Nafion<sup>®</sup> to catalyst/carbon, and the presence or absence of PTFE to be evaluated in regards to the microstructure of the catalyst layer. Uchida *et al.*(110) investigated catalyst inks obtained using an extensive variety of solvents for the Nafion<sup>®</sup> polymer. Fournier *et al.*(111)

investigated the effect of the type of carbon on the performance of PEFC cathodes. Gode *et al.*(70) studied the influence of the cathode composition on electrochemical performance for Nafion<sup>®</sup> contents between 10 to 70 wt%.

In subsequent works, researchers investigated the effect of the Nafion<sup>®</sup> content in the cathode on the performance and structure of electrodes.(51, 52, 112-114) In these studies, Nafion<sup>®</sup> was incorporated directly in the catalyst ink that was sprayed or brushed on the gas diffusion electrode (GDL). The optimal ratio of Nafion<sup>®</sup> to total weight (Pt/C + dry Nafion<sup>®</sup>) was found to be 30 – 40 wt%. Gode *et al.*(70) confirmed this by comparing the performance of cathodes with varying electrolyte content, finding that cathodes with low Nafion<sup>®</sup> content (< 30 wt%) were limited by poor kinetics due to incomplete wetting of Pt by Nafion<sup>®</sup>, by slower proton migration throughout the cathode, as well as by lower O<sub>2</sub> diffusion. For cathodes with medium Nafion<sup>®</sup> content (35 <  $x$  < 45 wt%), the wetting of Pt by Nafion<sup>®</sup> is reported to be at a maximum and the mass-transport limitation is essentially due to O<sub>2</sub> diffusion in the catalyst agglomerates. When the Nafion<sup>®</sup> content is higher (greater than 45 wt%), the overall porosity and average pore size decrease dramatically, consequently the cathode becomes limited by diffusion of O<sub>2</sub> in the cathode.

At the cathode, under normal operating conditions, there is a concern of flooding since excessive amounts of liquid water accumulate due to both the ORR and the electro-osmotic drag of water across the PEM from the anode. To effectively manage water within the cathode its hydrophobic properties are often adjusted. Too little water starves the solid electrolyte and results in dehydration

and an increase in the protonic resistance; an excessive accumulation of water presents mass transport issues. Typically, a hydrophobic material, polytetrafluoroethylene (PTFE), is added to the catalyst layer to tailor hydrophobic properties.(110, 112, 115) Uchida *et al.*(110) and Poltarzewski *et al.*(115) used PTFE directly in the catalyst layer, while Giorgi *et al.*(112) investigated the influence of PTFE in the gas diffusion layer and found that optimal ORR kinetics were obtained for a PTFE content of 10 wt%. A higher PTFE content resulted in a decrease in the total porosity of the electrode, a decrease in active Pt catalyst area, and, hence, a decrease in catalyst utilization.

In regards to non-Nafion<sup>®</sup>-based catalyst layers, SPEEK lacks the necessary hydrophobicity to prevent flooding of the cathode. However, Easton *et al.*(60) showed that the presence of sintered PTFE enhanced the hydrophobic character of the CL, reduced flooding, and increased the fuel cell performance. In this work it was believed that sintering of the PTFE above its melting point (327 °C) was a strict requirement. However, the need to sinter the PTFE restricts the number of fabrication processes available since SPEEK, and other sulfonated hydrocarbon electrolytes, decompose at these temperatures.

In this chapter, a modified catalyst ink formulation is proposed and investigated. Pt/C, SPEEK, and PTFE are incorporated into a single catalyst ink. These were deposited as catalyst layers, wherein the PTFE is not sintered. Physical characterization techniques have been employed to understand the effect of incorporating SPEEK, into the catalyst layer. Peak pore size, hydrophobic character, and surface morphology of SPEEK- and Nafion<sup>®</sup>-based

catalyst layers are compared. SPEEK 1.88 (IEC 188 mmol g<sup>-1</sup>) was chosen as the electrolyte as it possessed the highest proton conductivity (see Table 2.2) in the SPEEK series studied, and retained sufficient mechanical stability for use in the catalyst layer.

## **3.2 Experimental**

### **3.2.1 Materials**

Dimethylacetamide (DMAc), isopropyl alcohol (IPA), and sulfuric acid (H<sub>2</sub>SO<sub>4</sub>) were purchased from Alfa-Aesar and used as received. Hydrogen peroxide (H<sub>2</sub>O<sub>2</sub>), Nafion<sup>®</sup> 5 wt% resin solution (in lower aliphatic alcohols) and 60 wt% emulsion poly(tetrafluoroethylene) (in alcohols and surfactant) (PTFE) were purchased from Sigma Aldrich and used as received. PEEK was supplied by Victrex USA Inc., D.I. water (Millipore Co.) was used as a dispersion medium for the ink and for hydrating membranes. Carbon fiber paper (Toray TGPH - 060, wet proofed with 10 wt% PTFE) and catalyst, 20 wt% Pt on Vulcan XC72 carbon black (20 wt% Pt/C), were purchased from E-TEK Inc. and used as received.

### **3.2.2 Scanning Electron Microscopy**

A review of scanning electron microscopy (SEM) is given in 1.5.1.1. For analysis of Nafion<sup>®</sup>- and SPEEK-based catalyst layers a Hitachi S-3500N scanning electron microscope was employed. Catalyst layer samples were prepared by fracturing the electrode, when frozen with liquid nitrogen, into approximately 0.5 x 0.5 cm<sup>2</sup> samples. Following fracturing, samples were affixed to the appropriate sized stage required for SEM analysis. Eight samples were

supported on a circular peltier stage for individual analysis in the microscope; images were captured and observed using the supplied Quartz PCI image software (Quartz Imaging Corporation).

### **3.2.3 Mercury Porosimetry**

The pore size distribution for Nafion<sup>®</sup>- and SPEEK-based catalyst layers was determined using a Micromeritics AutoPore IV mercury intrusion system (Micromeritics Instrument Corporation). The concise theory for mercury intrusion analysis is outlined previously in section 1.5.1.2. Catalyst layer samples supported on gas diffusion electrodes were prepared by sectioning a 0.1 - 0.3 g sample with a scalpel into suitable dimensions for incorporation into a 3.00 mL Hg potentiometer for low and high pressure analysis. Cumulative volume and pore size distributions were calculated using Autopore IV software based upon the Washburn equation outlined previously in section 1.5.1.2. Pore size distribution data was normalized for the corresponding amount of catalyst layer material in each sample.

### **3.2.4 Contact Angle Measurements**

In this work, the Sessile method of contact angle determination was used to characterize the hydrophobic character of each catalyst layer surface (see section 1.5.1.3). Wetting measurements were performed using a AST Optima contact angle system under ambient conditions (18 - 22 °C, 30 - 35 % relative humidity) using a horizontal light beam to illuminate the water droplet. Samples were supported on a horizontal stage and 2.0  $\mu$ L drops of D.I. water were

deposited randomly across the surface for analysis. Contact angles were captured and observed for 5 - 7 water droplets, and averaged for the contact angle of each catalyst layer.

### 3.2.5 Fabrication of Nafion<sup>®</sup> - and SPEEK-based Catalyst Layers

Catalyst inks were prepared using different fabrication methods depending on whether Nafion<sup>®</sup> or SPEEK were incorporated into the catalyst layer. Details for each method are outlined below in Sections 3.2.5.1 and 3.2.5.2. Catalyst layers contained  $0.25 \pm 0.03 \text{ mg cm}^{-2}$  Pt (20 wt% Pt on Vulcan XC72). Nafion<sup>®</sup> solution (5 wt% in alcohols) or SPEEK 1.88 solution (5 wt% in DMAc), were used to supply the electrolyte. PTFE emulsion (60 wt%) was used as the hydrophobic binder. The PTFE content in the catalyst layer was 10 wt%, if present. In order to isolate the effect of changes in only the cathode catalyst layer, and to systematically understand the influence of the novel electrolyte and different fabrication procedures, a simplified MEA structure was implemented, in which no micro-porous layer (MPL) was incorporated between the catalyst layer and carbon paper gas diffusion layer.

Two fabrication methods were developed and examined for the incorporation of SPEEK electrolyte into catalyst layers. Catalyst layers prepared by Method 1 are referred to as **SPEEK\_CL1**, and catalyst layers prepared by Method 2 are termed **SPEEK\_CL2**. Nafion<sup>®</sup>-based catalyst layers, **Nafion\_CL**, were prepared from an experimental method commonly employed in the literature and outlined below in section 3.2.5.3.(52, 54, 60)

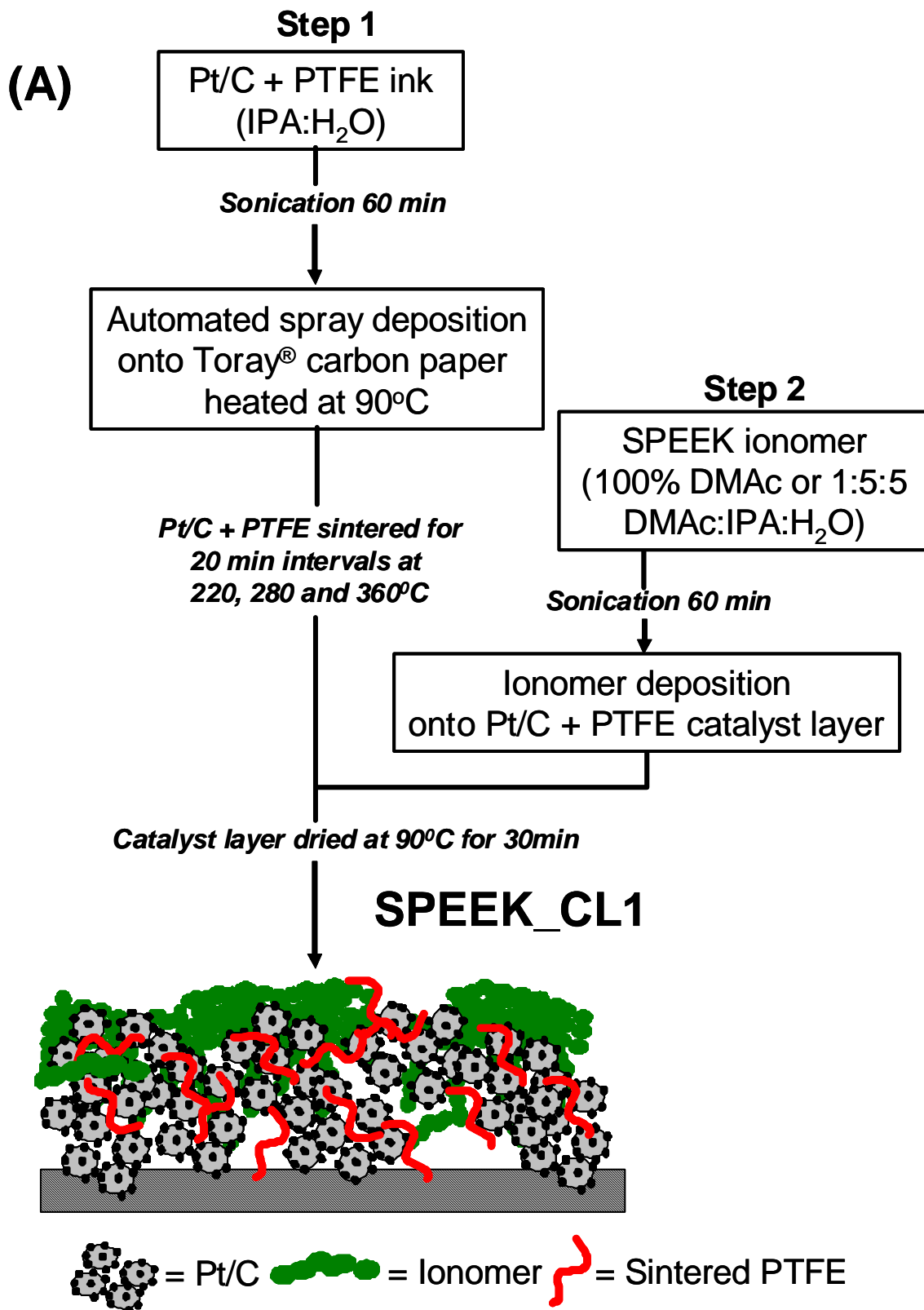
### 3.2.5.1 Fabrication of Graded SPEEK-based Catalyst Layers

Catalyst layers, **SPEEK\_CL1**, were prepared using the traditional approach developed by Easton *et al.*(60) which combined 10 wt% PTFE and Pt/C catalyst in a homogeneous ink in 1:1 IPA:H<sub>2</sub>O, and which was sonicated for 90 min to ensure complete homogeneous mixing. The ink was sprayed onto a carbon paper substrate (Toray TGP-060, 10 % wet proofed), heated at a constant temperature of 90 °C with a hot plate, using an automated spray machine (Ultra™ TT Automation Series System from EFD). Sintering of the hydrophobic PTFE was achieved by heating the CL step-wise at 220, 280 and 360 °C for 20 min intervals. A solution of SPEEK 1.88 (5 wt% in 100 % DMAc or 1:5:5 DMAc:IPA:Water) was sprayed on top of the pre-formed catalyst layer which contained only Pt/C and PTFE until the desired loading of SPEEK was achieved. A loading of 10 wt% SPEEK was chosen based on previous studies on the optimization of SPEEK content by Easton *et al.*(60). Electrodes were dried at 90 °C in an oven for 30 min. before being immersed into 0.5 M H<sub>2</sub>SO<sub>4</sub> for ~12 hr to remove residual DMAc, followed by immersion in H<sub>2</sub>O for ~12 hr to remove residual acid.

### 3.2.5.2 Fabrication of Homogeneous SPEEK-based Catalyst Layers

**SPEEK\_CL2** catalyst layers were prepared from a one-step procedure without thermally treating the PTFE. Catalyst layers were prepared by combining Pt/C, solubilized SPEEK 1.88, and PTFE (10 wt% loading) into a single dispersion medium (100 % DMAc or 1:5:5 DMAc:IPA:Water). After sonication, the ink was sprayed directly onto the GDL carbon substrate using an automated

spray coater until the appropriate loading was achieved. Electrodes were dried at 90 °C in an oven for 30 min before being immersed into 0.5 M H<sub>2</sub>SO<sub>4</sub> for ~12 hr to remove residual DMAc, followed by immersion in H<sub>2</sub>O for ~12 hr to remove residual acid. Unlike Method 1, no thermal annealing was used in the fabrication of **SPEEK\_CL2** catalyst layers. Based on a review of the literature, this (Method 2) is the first report in which a sulfonated hydrocarbon electrolyte has been co-deposited with both Pt/C *and* PTFE. The catalyst layer microstructure expected from the two different fabrication methods is portrayed in **Figure 3.1**. In contrast to the expected non-uniform graded distribution of SPEEK in **SPEEK\_CL1**, **SPEEK\_CL2** catalyst layers are expected to result in a more uniform distribution of SPEEK.



**(B)**

**Step 1**

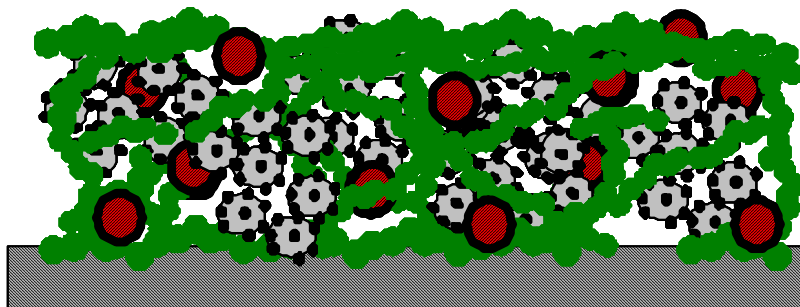
Pt/C + PTFE + SPEEK ionomer ink  
(DMAc:IPA:H<sub>2</sub>O)

*Sonication 60 min*

Automated spray deposition of ink onto  
Toray<sup>®</sup> carbon paper heated at 90°C

*Catalyst layer dried at 90°C for 30min*

**SPEEK\_CL2**



 = Pt/C    = Ionomer    = PTFE

Figure 3.1: Outline for Method 1 (A) and Method 2 (B) SPEEK-based catalyst layer fabrication techniques and expected resulting microstructure.

### 3.2.5.3 Fabrication of Nafion<sup>®</sup>-based Catalyst Layers

Nafion<sup>®</sup>-based catalyst layers, termed **Nafion\_CL**, were fabricated by spray coating ink dispersions containing 20 wt% P/C and 30 wt% Nafion<sup>®</sup> solution (Aldrich, 5 wt% solution) in 1:1 IPA:H<sub>2</sub>O. **Nafion\_CL** catalyst layers were devoid of PTFE, since previous work has shown that the perfluorinated backbone of Nafion<sup>®</sup> has sufficient hydrophobicity to reduce flooding by water.<sup>(52, 112, 116)</sup> **Nafion\_CL** cathodes were used to compare against **SPEEK\_CL1** and **SPEEK\_CL2** cathodes; additionally, **Nafion\_CL** was used as the anode in all MEAs.

## 3.3 Results and Discussion

### 3.3.1 Scanning Electron Microscopy (SEM)

**Nafion\_CL**, **SPEEK\_CL1** and **SPEEK\_CL2** catalyst layers were analyzed using a Hitachi S-3500N scanning electron microscope. The SEM images shown in **Figure 3.2**, **Figure 3.3** and **Figure 3.4** show the surfaces of **Nafion\_CL** (1:1 IPA:H<sub>2</sub>O), **SPEEK\_CL1** (100% DMAc) and **SPEEK\_CL2** (100% DMAc) catalyst layers deposited on gas diffusion electrodes. The large sub-structures observed are the underlying carbon fibers of the gas diffusion layer.

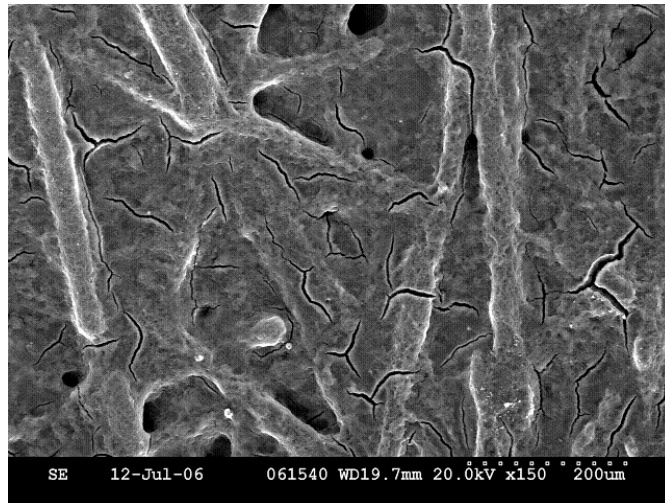


**Figure 3.2: SEM image of catalyst layer surface for Nafion\_CL (1:1 IPA: H<sub>2</sub>O). Loadings of 0.25 mg cm<sup>-2</sup> Pt/C and 30 wt% ionomer.**

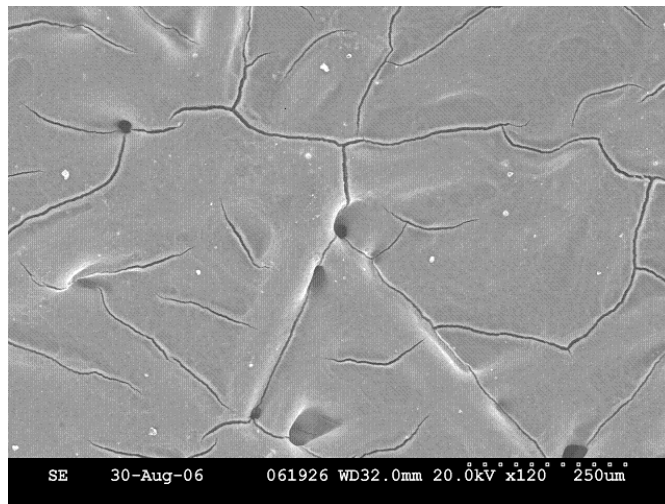


**Figure 3.3: SEM image of catalyst layer surface for SPEEK\_CL1 (100 % DMAc). Loadings of 0.25 mg cm<sup>-2</sup> Pt/C, 10 wt% PTFE and 10 wt% ionomer.**

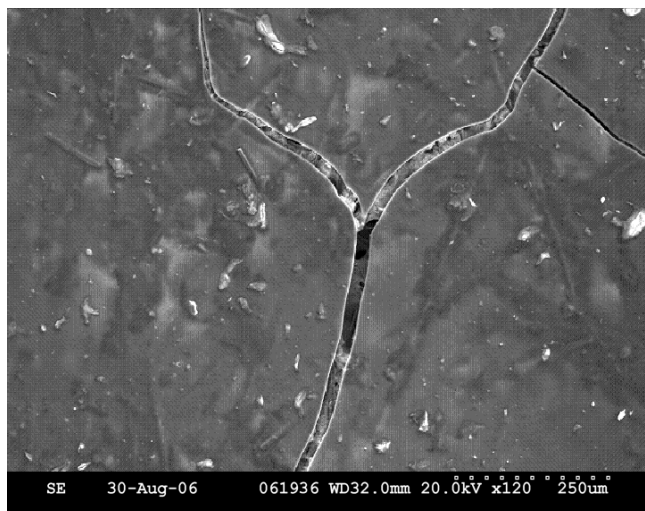


**Figure 3.4: SEM image of catalyst layer surface for SPEEK\_CL2 (100 % DMAc). Loadings of 0.25 mg cm<sup>-2</sup> Pt/C, 10 wt% PTFE and 10 wt% ionomer.**

The surface of the SPEEK-based catalyst layers, prepared with 100% DMAc, are much denser than **Nafion\_CL**, which may present implications in the mass transport of gases into the catalyst layer for fuel cell applications. These dense layers are thought to be due to the use of DMAc for dissolving SPEEK. DMAc possesses a high boiling point (167 °C) and requires longer drying times, which may result in dense films. To achieve a similar surface morphology to traditional Nafion<sup>®</sup> catalyst layers, low boiling temperature solvents for the preparation of solutions of SPEEK were investigated. Combinations of miscible solvents based on ratios of DMAc:IPA:H<sub>2</sub>O were studied, with the aim to minimize the overall DMAc content. The solvents were not only required to dissolve SPEEK but the solutions had to possess an appropriate viscosity and stability for ink fabrication. The optimum solvent system had a ratio of 1:5:5 DMAc:IPA:H<sub>2</sub>O (40 mL). This solvent system allowed complete solubilization of

the ionomer, an acceptable viscosity for spraying, and an efficient evaporation time of the solvent.

An SEM micrograph of a SPEEK-based catalyst layer prepared by Method 1, **SPEEK\_CL1**, using the multi-component solvent of 1:5:5 DMAc:IPA:H<sub>2</sub>O, is shown in **Figure 3.5**. The porosity of the underlying gas diffusion layer can now be clearly seen, indicating the importance of the choice of solvent for depositing the solid polymer electrolyte.

The same solvent mixture was used in the formulation of catalyst inks based on Pt/C, SPEEK, and PTFE. The SEM of a **SPEEK\_CL2** catalyst layer is shown in **Figure 3.6**. The characteristic surface morphology is similar to **SPEEK\_CL1** even though the former is based on a one-pot, one step procedure, and the latter is based on a two-pot, multi-step procedure.

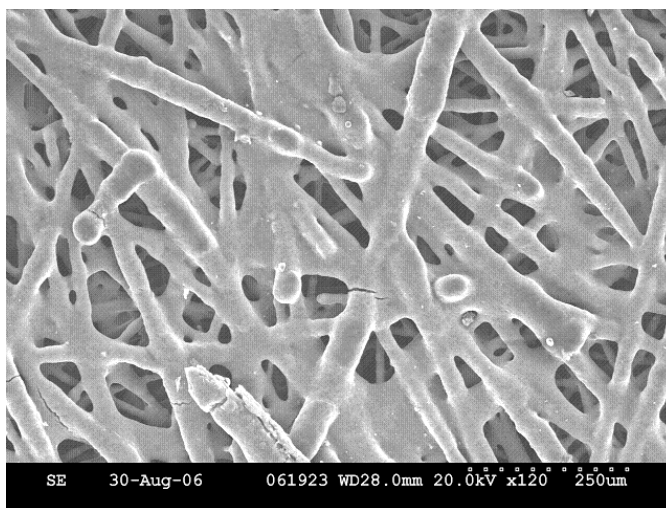


**Figure 3.5: SEM image of catalyst layer surface for SPEEK\_CL1 (DMAc:IPA:H<sub>2</sub>O (1:5:5)). Loadings of 0.25 mg cm<sup>-2</sup> Pt/C, 10 wt% PTFE and 10 wt% ionomer.**

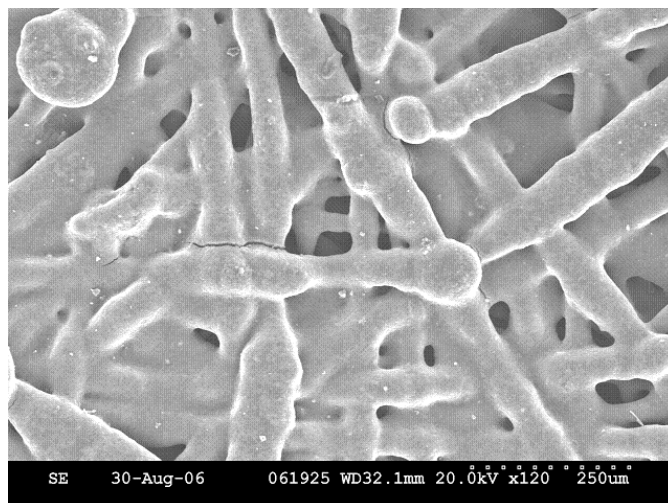


**Figure 3.6: SEM image of catalyst layer surface for SPEEK\_CL2 (DMAc:IPA:H<sub>2</sub>O (1:5:5)). Loadings of 0.25 mg cm<sup>-2</sup> Pt/C, 10 wt% PTFE and 10 wt% ionomer.**

SPEEK catalyst layers prepared using 1:5:5 DMAc:IPA:H<sub>2</sub>O possessed an increased porosity compared to 100 % DMAc CLs as observed by SEM micrographs (**Figure 3.5** and **Figure 3.6**), and quantitatively determined by mercury porosimetry analysis, as described in the next section. For both methods, the 1:5:5 DMAc:IPA:H<sub>2</sub>O solvent system formed a more porous CL, with the carbon fiber support matrix easily distinguished under the CL ink. SEM micrographs show that SPEEK-based CLs fabricated by Method 1 possess a more porous CL compared to those fabricated using Method 2 when equivalent solvent systems are used, as evidenced by the extent of carbon fiber matrix exposed.

### **3.3.2 Mercury Porosimetry**

Pore size and pore size distributions, calculated from mercury porosimetry analysis of **Nafion\_CL**, **SPEEK\_CL1** and **SPEEK\_CL2** prepared using

DMAc:IPA:H<sub>2</sub>O dispersion medium/solvent, are shown in **Figure 3.7**. The difference in peak pore size for **SPEEK\_CL1** catalyst layers prepared from solutions of SPEEK in DMAc and DMAc:IPA:H<sub>2</sub>O solvents is illustrated in **Figure 3.8**. The peak pore size for each catalyst layer is presented in Table 3.1.

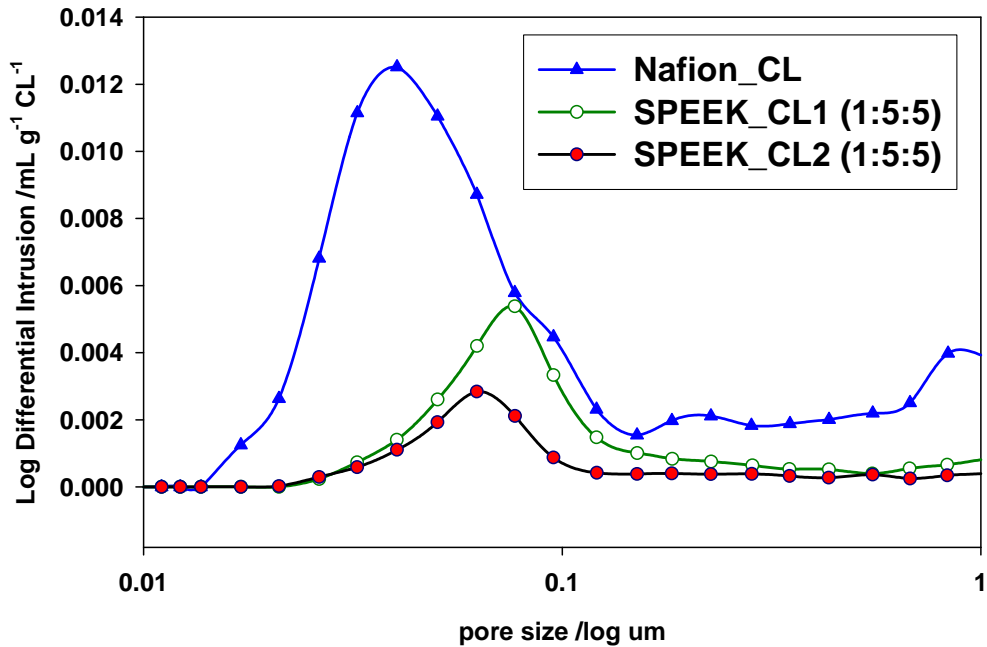


**Figure 3.7:** Catalyst layer pore size distribution, normalized to catalyst layer mass content for Nafion\_CL (-▲-)(1:1 IPA: H<sub>2</sub>O), SPEEK\_CL1(-○-), and SPEEK\_CL2(-●-) (1:5:5 DMAc:IPA:H<sub>2</sub>O).

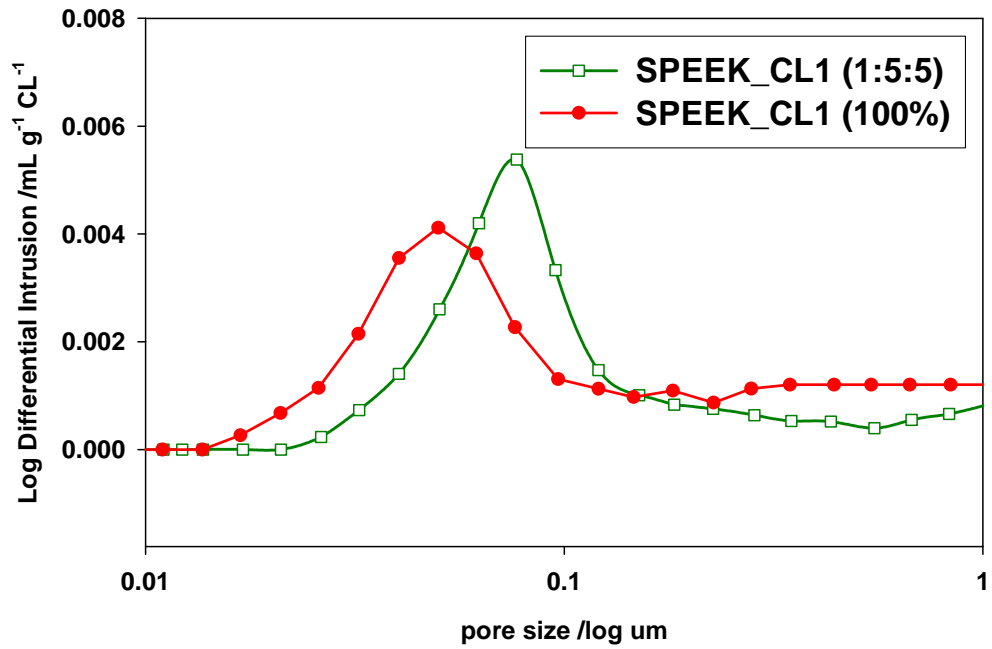


Figure 3.8: Catalyst layer pore size distribution, normalized to catalyst layer content, for SPEEK\_CL1. 100 % DMAc (-●-) and 1:5:5 DMAc: IPA: H<sub>2</sub>O(-□-) solvent system

Table 3.1: Solvent/Dispersion medium, electrolyte content, and peak pore size for Nafion\_CL, SPEEK\_CL1 and SPEEK\_CL2.

Catalyst Layer	Solvent /Dispersion medium	Electrolyte content wt%	Peak pore size nm
SPEEK_CL1	DMAC	10	51 ± 3
SPEEK_CL1	1:5:5 DMAC:IPA:H <sub>2</sub> O	10	77 ± 4
SPEEK_CL2	1:5:5 DMAC:IPA:H <sub>2</sub> O	10	62 ± 3
Nafion_CL	1:1 IPA:H <sub>2</sub> O	30	40 ± 3

Table 3.1 shows peak pore sizes for the **SPEEK\_CL1** to be  $77 \pm 4$  nm, and **SPEEK\_CL2** to be  $62 \pm 3$  nm for equivalent SPEEK content and solvent composition. The “dense” surface morphology of the **SPEEK\_CL1** catalyst layer prepared from 100 % DMAc yields a smaller peak pore size ( $51 \pm 3$  nm) compared to that prepared from DMAc:IPA:H<sub>2</sub>O. **Nafion\_CL** catalyst layers possess the smallest peak pore size. The pores in this size region are macropores (30 – 100 nm) and are sufficient in size for molecular gas diffusion and water removal.(53) The existence of micro- and macro-pores in the catalyst layer has been presented previously by Watanabe *et al.*(117, 118). The porosimetry data indicates that catalyst layers prepared by Method 2 possess smaller peak pore sizes than those prepared by Method 1. This may potentially restrict oxygen diffusion and water transport in catalyst layers prepared by Method 2, and this may increase the mass transfer limitations during fuel cell operation. These implications are discussed later in the thesis. Compared to the peak pore size of  $40 \pm 3$  nm determined for **Nafion\_CL**, larger diameter pores found in SPEEK catalyst layers are reasoned to be due to the presence of the PTFE. This work confirms a similar result published by Easton *et al.*(60), where the presence of the PTFE is found to lead to larger pore sizes. These larger pores are thought to be desirable since SPEEK is more hydrophilic than Nafion<sup>®</sup>, and larger pores can potentially lead to better water management within the catalyst layer.

### 3.3.3 Hydrophobic/Hydrophilic Character of SPEEK-based Catalyst Layers

In this work, the Sessile method of contact angle determination was used to characterize hydrophobic character of each CL (see section 1.5.1.3). The sessile drop method is one in which a drop of water is placed on top of the sample allowing the contact angle to be measured by fitting a tangent to the three-phase point where the liquid surface touches the solid surface.<sup>(20)</sup> The difference in hydrophobicity of **SPEEK\_CL1** and **SPEEK\_CL2** surfaces can be seen in **Figure 3.9**. Contact angles of  $154 \pm 3^\circ$  and  $81 \pm 3^\circ$  were determined for the **SPEEK\_CL1** and **SPEEK\_CL2** catalyst layers, respectively. In the former, PTFE is sintered in the preformed catalyst layer, prior to the deposition of solid polymer electrolyte; whereas in the latter, PTFE is not sintered and is simply deposited as an emulsion in the catalyst ink. Clearly, the surfaces of catalyst layers prepared by Method 1 are much more hydrophobic than those prepared by Method 2. The enhanced hydrophobicity of **SPEEK\_CL1** catalyst layers could be due to many factors including the process by which SPEEK precipitates in the pores from solution during evaporation of the solvent, or the sintering process by which PTFE melts and subsequently crystallizes, or by which volatile precursors, such as surfactants, present in the PTFE emulsion ink matrix, are removed during the thermal treatment. The implication of the hydrophobicity of the catalyst layers will be discussed later in the context of fuel cell performance.

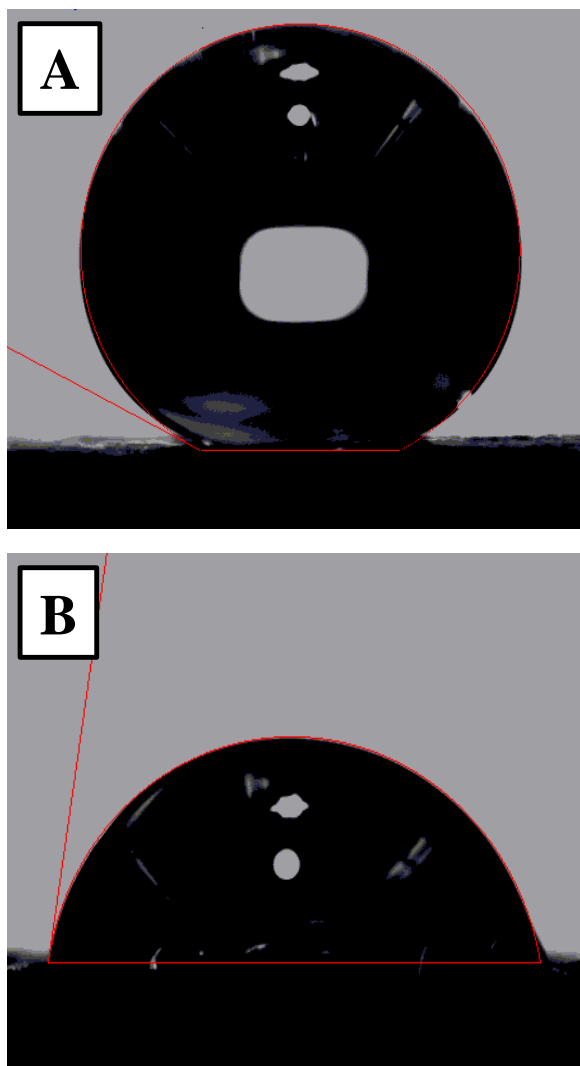


**Figure 3.9: Contact angle of D.I. water droplet on SPEEK\_CL1 (A) and SPEEK\_CL2 (B) surfaces.**

### **3.4 Conclusion**

The physical characteristics of SPEEK-based catalyst layers were examined using SEM, Hg porosimetry and contact angle measurement analysis. The electrode fabrication procedure and ink dispersion medium was studied, and

comparisons are made with Nafion<sup>®</sup>-based catalyst layers prepared using conventional fabrication techniques.

A strong relationship between solvent choice and the resulting catalyst layer porosity was found. **SPEEK\_CL1** catalyst layers fabricated with DMAc solvent yielded catalyst layers with small pore sizes and a dense film morphology on top of the gas diffusion layer. Since optimum peak pore size and porosity in the catalyst layer is essential to achieve efficient mass transport in the cathode, consequently the importance of using minimal amounts of higher boiling solvent in catalyst layer fabrication is indicated.

Scanning electron microscopy shows that SPEEK-based catalyst layers fabricated by Method 1 and Method 2 possess comparable surface morphologies when an analogous solvent/dispersion medium, DMAc:IPA:H<sub>2</sub>O, was employed. Catalyst layers fabricated by Method 1, resulted in larger pore sizes compared to those fabricated using Method 2. A larger pore size (for the same electrode composition) is thought to be more favorable for the electrode's ability to transport gas through the porous network. Larger pores are also thought to support more efficient water management, and a reduced tendency to flood. The hydrophobicity of catalyst layers prepared by Method 1 was found to be higher than those prepared by Method 2. It remains to be determined if the increased hydrophobicity is due to the sintering of PTFE or other factors that result from the heat treatment, or simply the deposition technique itself.

## CHAPTER 4: ELECTROCHEMICAL CHARACTERIZATION OF SPEEK-BASED CATALYST LAYERS

### 4.1 Introduction

While many groups have reported on the limitations of Nafion<sup>®</sup>-based catalyst layers,(5, 50-52) few have focused on understanding the electrochemical and physical characteristics of sulfonated hydrocarbon-based catalyst layers. It is recognized, however, that the choice of solid polymer electrolyte greatly influences fuel cell performance. A review of the literature on sulfonated hydrocarbon-based catalyst layers is provided in Chapter 1.

Electrochemical techniques such as the H<sub>2</sub>/O<sub>2</sub> performance polarization analysis (IV), cyclic voltammetry (CV), and electrochemical impedance spectroscopy (EIS) are powerful methods for investigating the electrochemical properties of PEMFC catalyst layers.(20, 70, 84, 116) Since the performance of a given MEA is a function of the kinetic, Ohmic and mass transfer resistances, accounting for losses associated with these various processes is vital component in understanding and improving fuel cell performance.

In this chapter, SPEEK-based catalyst layers are studied using electrochemical techniques. These studies complement the ORR mass transport and kinetic analyses carried out for SPEEK solid electrolytes and the physical characterization of catalyst layers described in Chapters 2 and 3, respectively.

## 4.2 Experimental

### 4.2.1 Materials

Dimethylacetamide (DMAc), iso-propyl alcohol (IPA), and sulfuric acid ( $\text{H}_2\text{SO}_4$ ) were purchased from Alfa-Aesar and used as received. Hydrogen peroxide ( $\text{H}_2\text{O}_2$ ), Nafion<sup>®</sup> 5 wt% solution (in low aliphatic alcohols) and 60 wt% poly(tetrafluoroethylene) (PTFE) emulsion (in alcohols and surfactant) were purchased from Sigma Aldrich and used as received. SPEEK was prepared as described in Chapter 2. The experimental procedure for fabrication of catalyst layers containing Nafion<sup>®</sup> and SPEEK 1.88 electrolyte is outlined in 3.2.5.

### 4.2.2 Fabrication of Membrane Electrode Assemblies

Nafion<sup>®</sup> and SPEEK Membrane Electrode Assemblies (MEA) were prepared by placing 5 cm<sup>2</sup> cathode and anode electrodes on either side of a pre-treated SPEEK 1.88 membrane (3 x 3 cm, see 2.2.3). Cathodes were selected from **Nafion\_CL**, **SPEEK\_CL1** or **SPEEK\_CL2** electrodes, and anodes were **Nafion\_CL**. Electrodes and SPEEK PEM were hot pressed together at 135 °C and 85 kg cm<sup>-2</sup> for 90 s between Teflon<sup>®</sup> plates in a Carver Hot press. The MEA geometrical operating area was 5 cm<sup>2</sup>.

### 4.2.3 Fuel Cell Single Cell Operating Conditions

MEAs were tested in a 5 cm<sup>2</sup> single cell having dual serpentine flow channels (Teledyne Technologies Inc.) using a fuel cell test station Medusa, Teledyne Technologies Inc. The single cell is depicted in **Figure 4.1**. The cell was heated at 50 °C by cartridges in each end plate. Pure H<sub>2</sub> and O<sub>2</sub> were used

as reactant gases. Identical  $H_2$  and  $O_2$  partial pressures were used in each experiment and passed through humidifiers whose temperatures were maintained to produce a constant relative humidity (100 % RH) of gases at the inlet. Flow rates were  $200 \text{ mL min}^{-1}$  and back pressures were atmospheric for both  $H_2$  and  $O_2$ . These flow rates equate to stoichiometric flows of 12/24 ( $H_2/O_2$ ) at  $0.5 \text{ A cm}^{-2}$ . High gas flow rates, and equally high stoichiometric flows, were applied to avoid gas starvation in the gas diffusion layer and to ensure that differences observed in performance were due to the differences in the catalyst layers of each MEA.

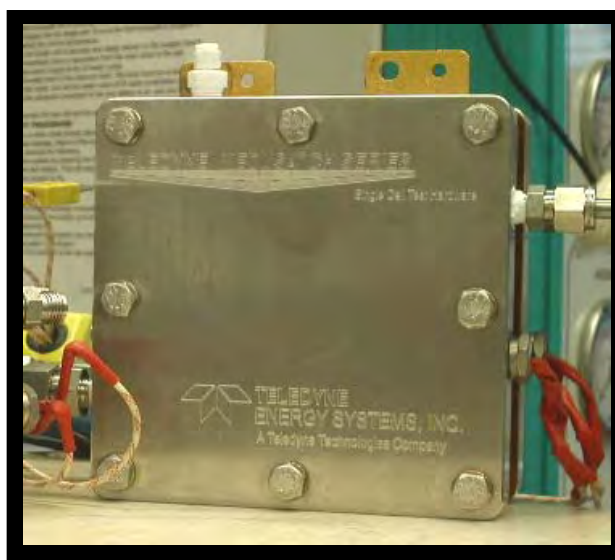


**Figure 4.1: Teledyne Technologies Inc.  $5\text{cm}^2$  single cell fixture used for fuel cell experiments.**

## **4.2.4 Fuel Cell Electrochemical Experiments**

### **4.2.4.1 Polarization Performance**

Prior to obtaining I-V polarization data, the cell was conditioned in 30 min intervals between 0.75 and 0.60 V in 0.05 V steps. Following cell conditioning,

polarization data were collected by scanning the cell voltage from open circuit voltage (OCV) to 0.2 V in 0.05 V steps (60 s at each potential point). Polarization curves were obtained for all MEAs in a single cell configuration at 50 °C, atmospheric pressure and 100 % RH. Scans were repeated 8 - 10 times to ensure reproducibility within each MEA. Results were presented as the average of the successive scan, showing less than 11% deviation for all MEAs.

#### **4.2.4.2 Cyclic Voltammetry (CV)**

Cyclic voltammograms were recorded using a Solartron 1287 potentiostat between 0.9 and 0.04 V vs. SHE at a scan rate of 20 mV s<sup>-1</sup>. The last of 50 cycles was used for data analysis. Using the supplied software, Corrware<sup>®</sup>, the double layer charging capacitance of the MEA was accounted for, charges corresponding to Pt - H adsorption were determined and averaged for calculation of the ESA for each cathode catalyst layer (see section 1.5.2.3).

#### **4.2.4.3 Electrochemical Impedance Spectroscopy (EIS)**

EIS was employed by imposing a small sinusoidal (AC) voltage (10 mV) of known amplitude and frequency (10 kHz to 0.1 Hz) to the cell while monitoring the AC amplitude and phase response of the cell using a Solartron 1287 potentiostat and a 1260 frequency analyzer. Following completion of polarization measurements, impedance measurements were carried out after purging the cathode with humidified nitrogen (100 % RH) for 15 min. This procedure removes residual oxygen without dehydrating the membrane. The cell potential

was maintained at 0.45 V vs. SHE during EIS experiments, to remove the influence of other electrochemical reactions influencing the EIS response.

## 4.3 Results and Discussion

### 4.3.1 Electrochemical Characterization of SPEEK-based Catalyst Layers

In order to quantify the differences between **Nafion\_CL**, **SPEEK\_CL1** and **SPEEK\_CL2**, current-potential polarization curves were measured for each MEA. The polarization curves obtained for **Nafion\_CL**, **SPEEK\_CL1** and **SPEEK\_CL2**, after correcting for Ohmic losses in the cell, can be seen in **Figure 4.2**. The Ohmic loss (uncompensated resistance,  $R_u$ ) for each polarization curve was determined from the high frequency x-intercept of Nyquist plots obtained by EIS, shown in **Figure 4.3**, and are also plotted in **Figure 4.2**. Ohmic voltage losses are due to the summed resistance of ion migration within the electrolyte, resistance to electron transport within the cell components (electrodes, gas diffusion layer, and flow field/current collectors), and contact resistances.(119) The trend of decreasing high frequency resistance with increasing current density is evident for all MEAs, and reasoned to be due to increased water production that reduces the proton resistance of the PEM.(20)

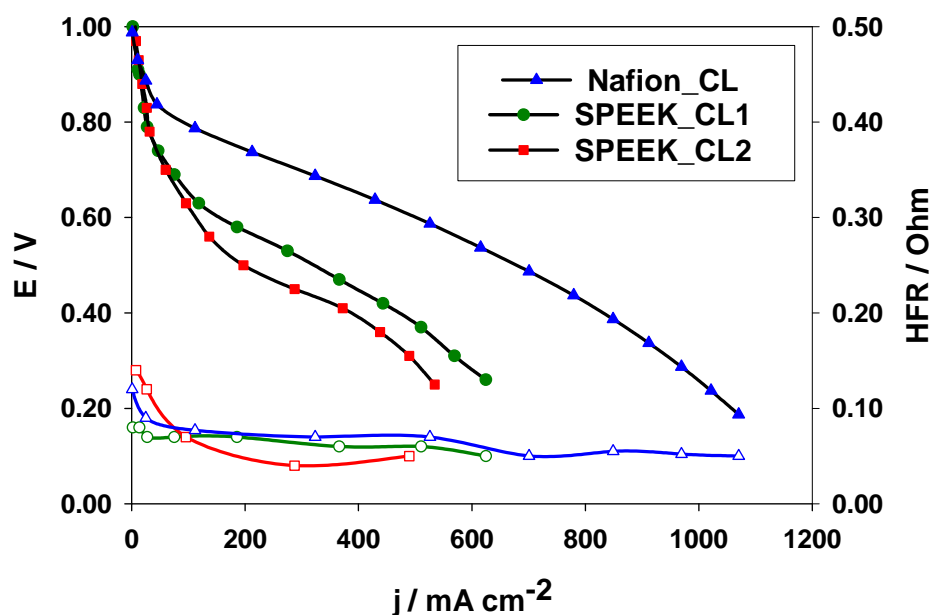


Figure 4.2: Polarization performance (closed) and high frequency resistance (HFR) (open) for Nafion\_CL, SPEEK\_CL1 and SPEEK\_CL2 MEAs. 50 °C cell, 0.2 L/min  $\text{H}_2/\text{O}_2$  humidified gases, and atmospheric pressure.

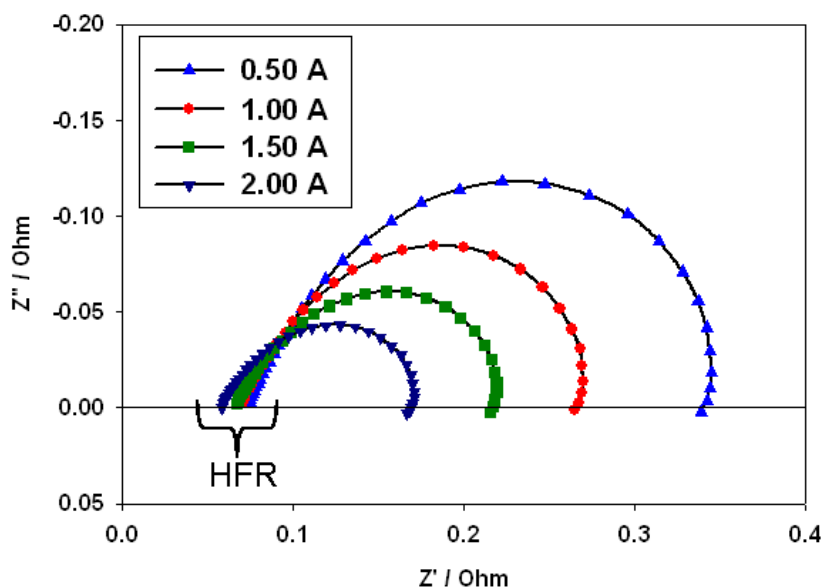


Figure 4.3: Typical EIS Nyquist response for SPEEK\_CL1 cathode at increasing current density: 0.50 A, 1.0 A, 1.5 A, and 2.0 A.  $\text{H}_2/\text{O}_2$ , 100 % RH, 0.2 L  $\text{min}^{-1}$  and 50 °C cell temperature.

Despite the open circuit voltages being similar, **SPEEK\_CL1** and **SPEEK\_CL2** show significant activation overpotential compared to **Nafion\_CL**. This manifests itself as decreased performance across the entire current density range. A similar observation for a sulfonated polyarylene ether sulfone-based catalyst layer was reported by von Kraemer.(62) A strong correlation between performance and method of SPEEK-based catalyst layer fabrication is observed. The two-pot, two-step preparation method described as Method 1 (see Chapter 3) provides catalyst layers that result in higher current densities throughout the polarization region, compared to the one-pot, one-step that is described as Method 2.

#### **4.3.2 Electrochemical Surface Area of SPEEK-based Catalyst Layers**

Cyclic voltammograms of **Nafion\_CL**, **SPEEK\_CL1** and **SPEEK\_CL2** catalyst layers, illustrating the extent of Pt utilization in the catalyst layer are shown in **Figure 4.4**. SPEEK-based catalyst layers show a suppressed CV profile compared to Nafion<sup>®</sup>-based catalyst layers. The electrochemical surface areas for each catalyst layer, normalized per gram of Pt, were calculated from the charge accumulated due to the adsorption of hydrogen on Pt, as explained in the experimental section (section 1.5.2.3), and are provided in Table 4.1.

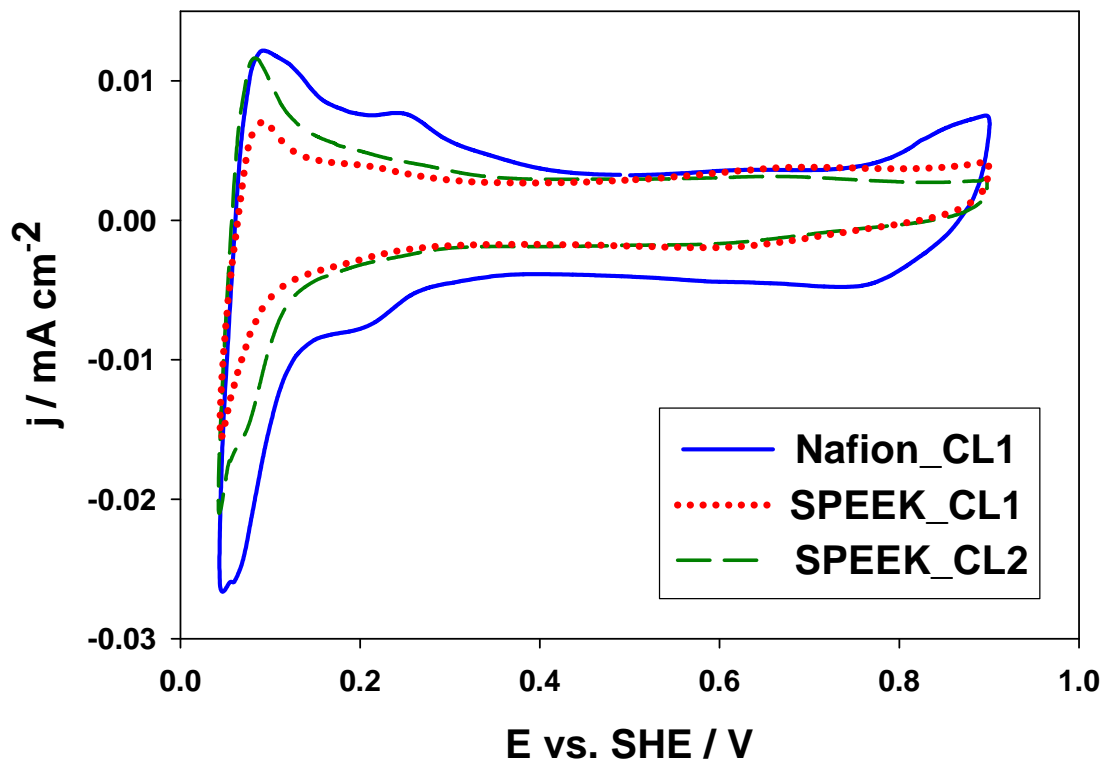


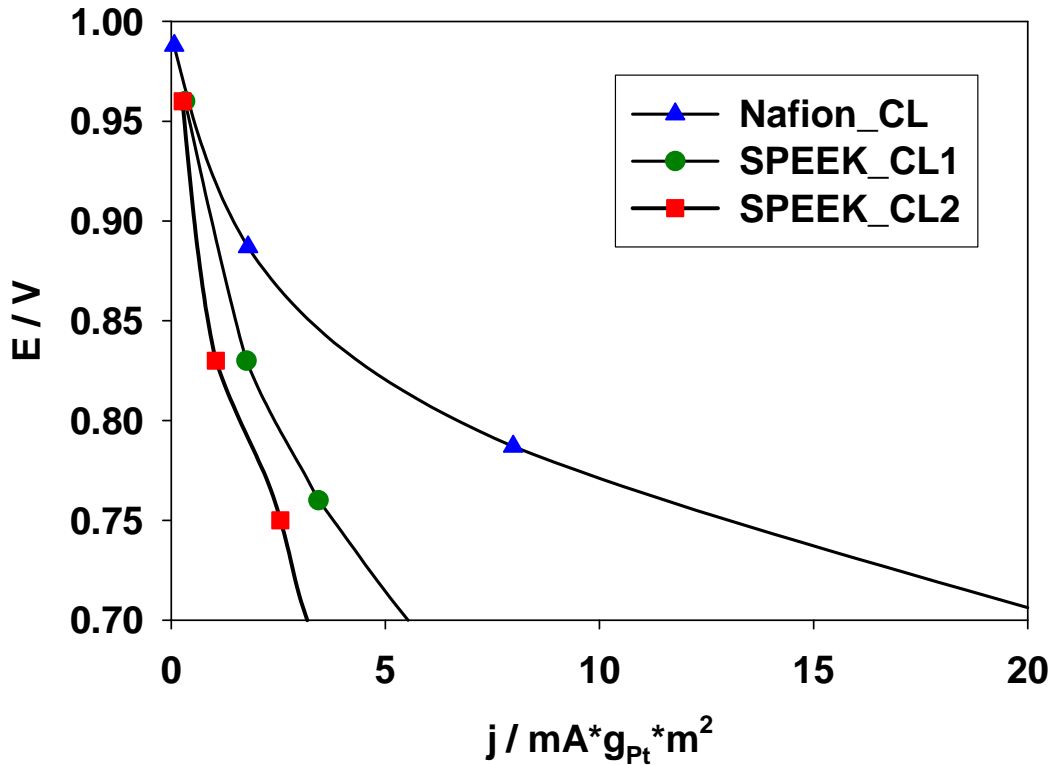
Figure 4.4: Cyclic voltammograms for Nafion\_CL (dash), SPEEK\_CL1 (short dash) and SPEEK\_CL2 (solid). 50 °C, N<sub>2</sub>/H<sub>2</sub> 0/0.2 L min<sup>-1</sup>, and potential window of 0.04 – 0.9 V at scan rate of 20 mV s<sup>-1</sup>.

Table 4.1: Electrochemical surface area for Nafion\_CL, SPEEK\_CL1 and SPEEK\_CL2. 50 °C cell temperature, 0.2 L min<sup>-1</sup> H<sub>2</sub>/N<sub>2</sub>, 100 % RH, and atmospheric pressure.

Catalyst Layer	Charge Pt-H <sub>ads</sub> mC cm <sup>-2</sup>	C <sub>dl</sub> mF cm <sup>-2</sup>	ESA m <sup>2</sup> g <sup>-1</sup>
Nafion_CL	294.7 ± 12	126 ± 6	70 ± 3
SPEEK_CL1	86.1 ± 9	22 ± 2	32 ± 4
SPEEK_CL2	98.3 ± 11	25 ± 3	37 ± 4

ESA values for **Nafion\_CL** are  $70 \pm 3 \text{ m}^2 \text{ g}^{-1}$  and compare well with similarly-structured Nafion<sup>®</sup>-based catalyst layers reported in the literature.(116) Comparing SPEEK-based catalyst layers, **SPEEK\_CL2** shows a 15 % higher usage for Pt compared to **SPEEK\_CL1**, which indicates that the modified fabrication method (Method 2) which is predicted to lead to a homogeneous SPEEK content increases the active area. ESA values for SPEEK-based catalyst layers are  $32 \pm 4 \text{ m}^2 \text{ g}^{-1}$  for **SPEEK\_CL1** and  $37 \pm 4 \text{ m}^2 \text{ g}^{-1}$  for **SPEEK\_CL2**. Thus, SPEEK-based catalyst layers show notably lower ESAs than **Nafion\_CL**, regardless of which fabrication method is used. The Nafion<sup>®</sup> cathode has nearly double the effective usage of Pt. This result indicates that for the SPEEK contents used to prepare **SPEEK\_CL1** and **SPEEK\_CL2**, the “wetting” of the active sites is diminished and Pt utilization is lower. To account for the difference in electrochemically active surface area between Nafion<sup>®</sup>- and SPEEK-based catalyst layers, the polarization performance data (**Figure 4.2**) was normalized to the respective ESA ( $\text{m}^2/\text{g}_{\text{Pt}}$ ) of each catalyst layer and is presented in **Figure 4.5**. After normalization, it is evident that SPEEK-based catalyst layers still suffer from significant activation limitations, as **Nafion\_CL** has a two fold increase in normalized current density when comparing the catalyst layers in the kinetically controlled potential of region of 0.85V. The low electronically active surface area for SPEEK-based catalyst layers does not solely account for the reduced polarization performance. To account for the larger activation limitations, losses to each catalyst layer were further investigated by considering the influence of the catalyst layer solvent choice and

PTFE presence, additionally the variance in ionic conductivity outlined between the catalyst layers is interpreted in section 4.3.6.



4.5: Polarization performance for Nafion\_CL, SPEEK\_CL1 and SPEEK\_CL2 MEAs normalized by the electronically active surface area for each catalyst layer. 50 °C cell, 0.2 L/min H<sub>2</sub>/O<sub>2</sub> humidified gases, and atmospheric pressure.

To characterize limitations due to the choice of electrolyte, the effect of SPEEK electrolyte was investigated as it has been reported previously by Xu *et al.*(120) and Gottesfeld *et al.*(121) that the presence of solid electrolyte on top of Pt decreases its ESA compared to a clean Pt surface. Rotating disk studies show that Nafion® partially blocks the Pt surface, leading to a ~20 % decrease in ESA. In light of this, the extent of blocking Pt sites by SPEEK was evaluated by

preparing catalyst layers incorporating both Nafion<sup>®</sup> and SPEEK electrolyte simultaneously. Cathode electrodes were prepared using the fabrication method proposed for **Nafion\_CL**, with the additional amendment of adding SPEEK as well. **Figure 4.6** shows cyclic voltammograms of catalyst layers containing SPEEK contents of 0 to 30 wt% and a fixed content of Nafion<sup>®</sup>. ESA values for each catalyst layer were calculated from the hydrogen adsorption charge, and presented in Table 4.2.

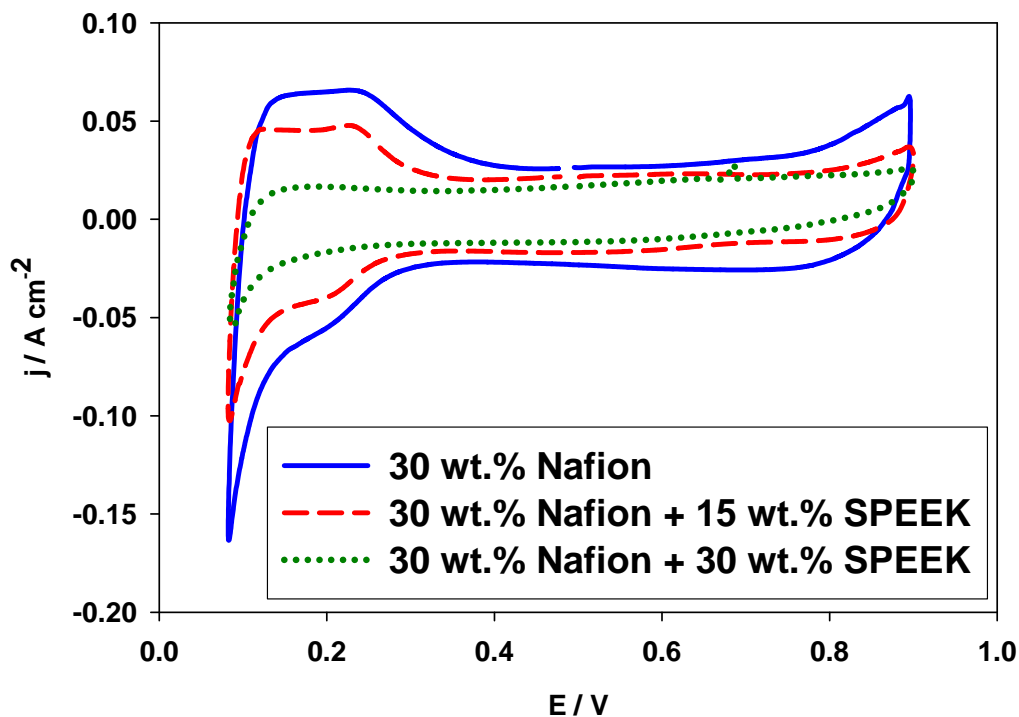


**Figure 4.6:** Cyclic voltammograms of Nafion\_CL with 0 wt% (solid), 15 wt% (dashed), and 30 wt% (dotted) SPEEK. 50 °C, N<sub>2</sub>/H<sub>2</sub> gases, 100 % RH, scan rate 20 mV s<sup>-1</sup>, and Potential window 0.04 – 0.9 V. The Nafion<sup>®</sup> content was 30 wt%.

**Table 4.2: Electrochemical Surface Area for 30 wt% Nafion<sup>®</sup> catalyst layer containing varying content of SPEEK. 50 °C cell temperature, 0.2 L min<sup>-1</sup> H<sub>2</sub>/N<sub>2</sub>, and ambient pressure.**

Catalyst Layer	ESA m <sup>2</sup> g <sup>-1</sup>
30 wt% Nafion <sup>®</sup>	68 ± 5
30 wt% Nafion <sup>®</sup> + 15 wt% SPEEK	42 ± 4
30 wt% Nafion <sup>®</sup> + 30 wt% SPEEK	15 ± 2

Table 4.2 shows an approximately five-times decrease in ESA (from 68 to 15 m<sup>2</sup> g<sup>-1</sup>) when increasing the SPEEK content from 0 to 30 wt%. These decreasing ESA values clearly indicate that the addition of SPEEK strongly blocks active sites of Pt. This will be detrimental to fuel cell efficiency and lower catalyst utilization.

#### 4.3.3 Electrochemical Influence from PTFE in Catalyst Layer

The effect of the presence of PTFE emulsion in the preparation of **SPEEK\_CL2** catalyst layers is shown in **Figure 4.7**. The corresponding ESA values for each catalyst layer are 28 ± 3 and 32 ± 4 m<sup>2</sup> g<sup>-1</sup> with and without PTFE, respectively. It is evident that the presence of PTFE in the catalyst layer does not affect the ESA of the catalyst layer, within experimental error. This result is in agreement with studies reported by Poltarzewki *et al.*(115), Uchida *et al.*(110), and Giorgi *et al.*(112) on the incorporation of PTFE in Nafion<sup>®</sup>-based

catalyst layers, whom also showed that the presence of PTFE is not detrimental to ESA values.

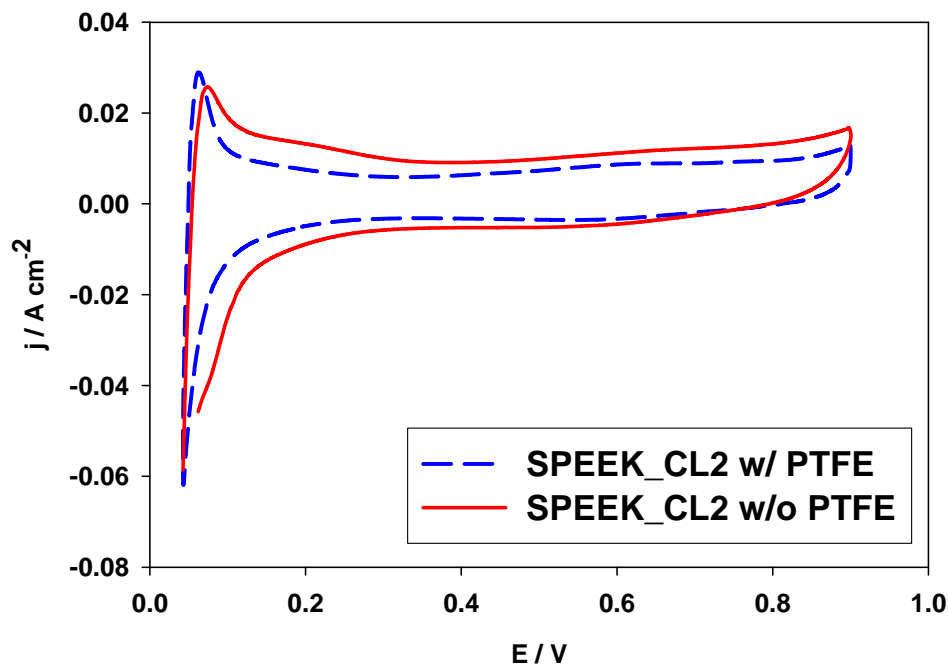
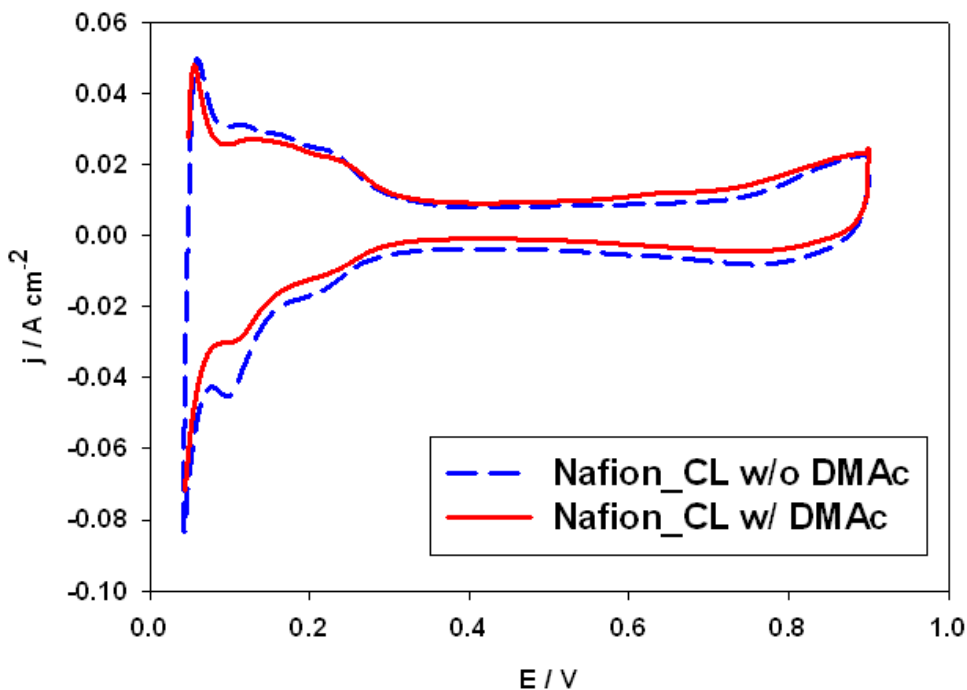


Figure 4.7: Cyclic voltammograms of SPEEK\_CL2 with PTFE (dashed) and without PTFE (solid). 50 °C cell temperature,  $\text{N}_2/\text{H}_2$  0/0.2  $\text{L min}^{-1}$ , 100 % RH, scan rate 20  $\text{mV s}^{-1}$ , and potential window 0.04 – 0.9 V.

#### 4.3.4 Influence of Solvents/Dispersion Media on ESA

The importance of the solvent and dispersion media used to prepare catalyst inks and catalyst layers on their physical characteristics was described in Chapter 3. Herein, the influence of the solvent and dispersion media on the ESA was investigated because SPEEK-based catalyst layers required the use of dimethylacetamide (DMAc) in addition to IPA and  $\text{H}_2\text{O}$ . The effect of using DMAc in the preparation of catalyst layers on the ESA of Pt was investigated by preparing a **Nafion\_CL** ink that contained the equivalent amount of DMAc (2 mL)

used in the preparation of **SPEEK\_CL1** and **SPEEK\_CL2** catalyst layers. The Nafion<sup>®</sup>/ DMAc electrode was dried at 90 °C in an oven for 30 min to mimic the SPEEK-based catalyst layer procedure. Cyclic voltammograms of the Nafion<sup>®</sup>-based catalyst layers prepared with and without DMAc are shown in **Figure 4.8**.



**Figure 4.8:** Cyclic voltammograms of Nafion\_CL prepared with (solid) without DMAc solvent (dashed) . 50 °C cell temperature,  $\text{N}_2/\text{H}_2$  stream, scan rate 20  $\text{mV s}^{-1}$ , and potential window 0.04 – 0.9 V.

Results show a depressed ESA value for catalyst layers prepared with DMAc solvent, with a decrease in ESA from  $70 \pm 4$  to  $58 \pm 3 \text{ m}^2 \text{ g}^{-1}$ . The use of DMAc, although not depressing the ESA values to the extent seen for the SPEEK catalyst layers (see table 4.1), does have an influence on the ESA of Nafion<sup>®</sup>-based catalyst layers. Noteworthy, a similar dependence on the ESA on the ionomer solvent choice was observed by Sambandam *et al.*(64) for

sulfonated poly(ether ether ketone) electrolyte catalyst layers, where ESA values were shown to be 30 % lower for catalyst layers prepared with DMAc solvent over the traditional alcohol solvent. However, no conclusive reasons were presented in that work to account for the differences in ESAs.

To further examine the effect of DMAc on Pt utilization, experiments were performed using ex-situ cyclic voltammetry on a 100  $\mu\text{m}$  polycrystalline Pt electrode in 1.0 M  $\text{H}_2\text{SO}_4$  containing varying DMAc concentrations. **Figure 4.9** below illustrates the slight decrease in ESA with increasing DMAc concentration. In the range of concentrations studied (1, 10, and 30 %), the overall change in ESA is low (less than  $7 \pm 2$  %), indicating that the presence of DMAc alone is not a significant factor in reducing the ESA of Pt.

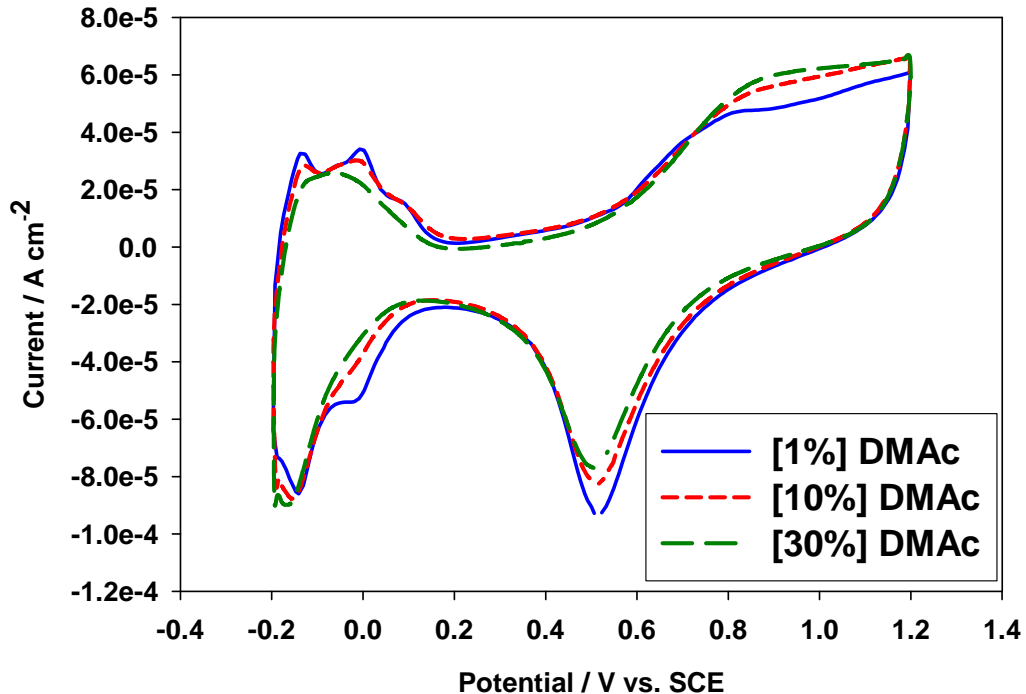


Figure 4.9: Cyclic voltammograms of a 100  $\mu\text{m}$  Pt electrode in 1.0 M  $\text{H}_2\text{SO}_4$  electrolyte containing DMAC concentrations of 1% (solid), 10% (short dash) and 30% (long dash), scan rate of  $50 \text{ mV s}^{-1}$ .

In addition, a film of solubilized SPEEK electrolyte ( $\sim 2 - 3 \mu\text{m}$  thickness (122)), from a 5 wt% solution in DMAC, was cast onto the surface of a 100  $\mu\text{m}$  Pt micro-electrode to assess the effect from the solid polymer electrolyte. It can be seen in **Figure 4.10** that the ESA decreases by  $9 \pm 2 \%$  upon deposition of SPEEK on top of the Pt surface. A similar experiment with Nafion<sup>®</sup> ionomer showed a similar degree of ESA change ( $8 \pm 2 \%$ ). These ex-situ electrochemical results suggest that there is a small decrease in ESA due to solvent and/or solid polymer electrolyte presence, but not to the extent that accounts for the difference between SPEEK- and Nafion<sup>®</sup>-based catalyst layers reported in Table 4.1.

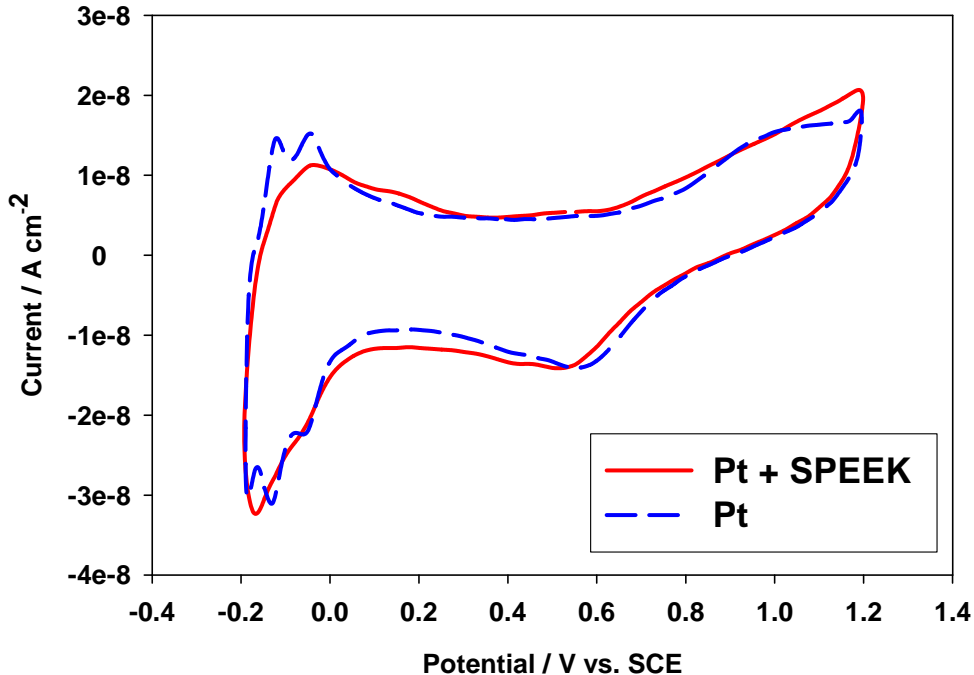


Figure 4.10: Cyclic voltammograms of 100  $\mu\text{m}$  Pt bare electrode bare (dashed) and SPEEK covered (solid). 1.0M  $\text{H}_2\text{SO}_4$  electrolyte, scan rate of  $50 \text{ mV s}^{-1}$ .

#### 4.3.5 Influence of Cathode Operating Environment

In-situ, fuel cell cyclic voltammetry was used to assess the utilization of Pt in the catalyst layer under different operating environment conditions. Adapting a similar approach to the one outlined by Brosha *et al.*(120), ESAs of **SPEEK\_CL1** and **Nafion\_CL** cathodes were investigated first under humidified nitrogen and secondly fully hydrated (purged) with D.I water. **Figure 4.11** and **4.12** represent voltammograms of **Nafion\_CL** and **SPEEK\_CL1** cathodes that are flooded with  $\text{N}_2$  then purged D.I water.

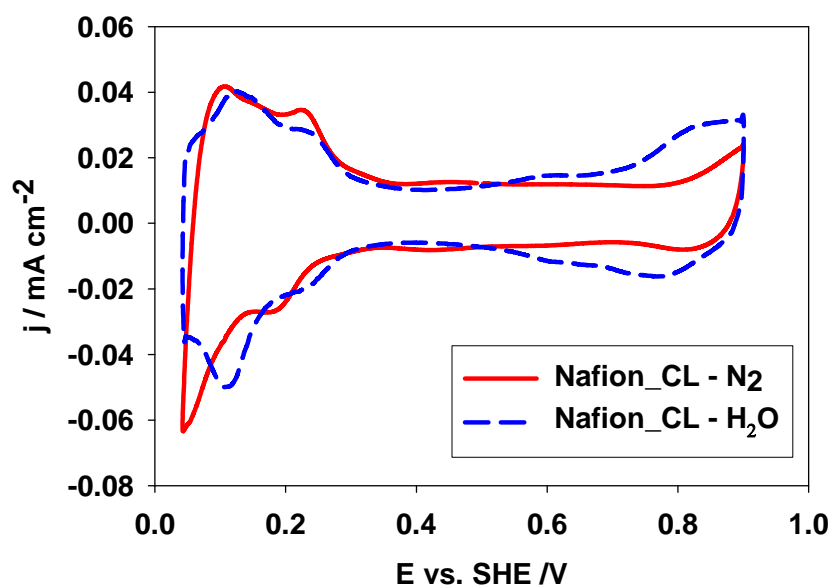


Figure 4.11: Cyclic voltammograms of Nafion\_CL cathode under humidified  $\text{N}_2$  (solid) and  $\text{H}_2\text{O}$  (dashed) environments. 50 °C cell temperature, potential window 0.04 – 0.9 V, scan rate, 50  $\text{mV s}^{-1}$ .

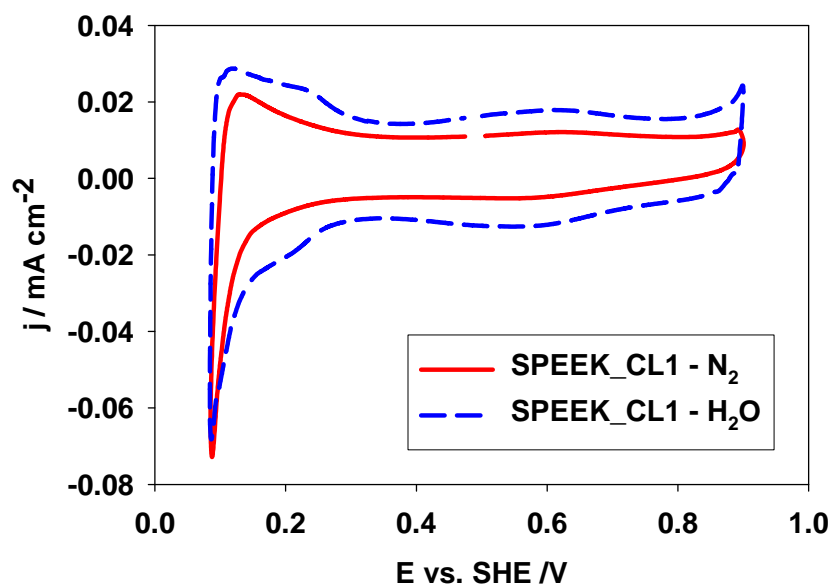


Figure 4.12: Cyclic voltammograms of SPEEK\_CL1 cathode in humidified  $\text{N}_2$  (solid) and  $\text{H}_2\text{O}$  (dashed) environments. 50 °C cell temperature, potential window 0.04 – 0.9 V, scan rate, 50  $\text{mV s}^{-1}$ .

The measured ESA for **Nafion\_CL** was  $65 \pm 3 \text{ m}^2 \text{ g}^{-1}$  under nitrogen and  $71 \pm 3 \text{ m}^2 \text{ g}^{-1}$  under purged D.I water. This slight difference may be attributed to changes in the ionomer/ Pt interface when  $\text{H}_2\text{O}$  is introduced into the cathode, as the presence of water will cause the ionomer to swell. Results suggest that the Pt utilization is originally high for Nafion<sup>®</sup> cathodes for all environments, as ESA results differ by only 9 %. A similar increase in the ESA was also found by Xu for their PFSI cathode when the cathode was purged with water or methanol.(120)

For **SPEEK\_CL1**, the ESA values were  $22 \pm 3 \text{ m}^2 \text{ g}^{-1}$  under nitrogen and  $29 \pm 3 \text{ m}^2 \text{ g}^{-1}$  in D.I  $\text{H}_2\text{O}$  as depicted in **Figure 4.12**. The 31 % increase in SPEEK ESA when purged with water is larger than for Nafion<sup>®</sup> catalyst layers, and indicates that Pt utilization is originally lower for SPEEK ionomer catalyst layers when operated at 100% RH compared to a flooded environment. In a non-flooded environment, poor wetting of the SPEEK electrolyte is thought to result in poor conductivity in the catalyst layer and a low ESA value. A strong dependence of proton conductivity on the relative humidity for SPEEK has been shown by Rikukawa *et al.*(37), with results indicating that conductivity increases with higher relative humidities and water uptake. This strong dependence on RH may result in SPEEK catalyst layers having poor proton conductivity unless in a completely flooded environment. Unfortunately, a flooded cathode presents significant mass transport limitations towards oxygen diffusion in the CL. The balance of Pt utilization, protonic resistance and mass transport limitations in the cathode was decoupled using electrochemical impedance spectroscopy, outlined below.

### 4.3.6 Proton Conductivity of Nafion<sup>®</sup> - and SPEEK-based Catalyst Layers

The extent of ionic resistance and mass transport limitations in the catalyst layer were determined for all MEAs using electrochemical impedance spectroscopy (EIS), outlined in the experimental section 1.5.2.4. The proton resistance of the catalyst layer was determined using the linear high frequency response (10 K Hz – 1 K Hz) as seen in the inset of **Figure 4.13**. This high frequency impedance response depends on the parameters of the catalyst layer,  $R_p$  and  $C_{dl}$ , and allows catalyst layer resistance and protonic conductivity to be determined from theory developed by Eikerling *et al.*(85) and Havranek *et al.*(86).

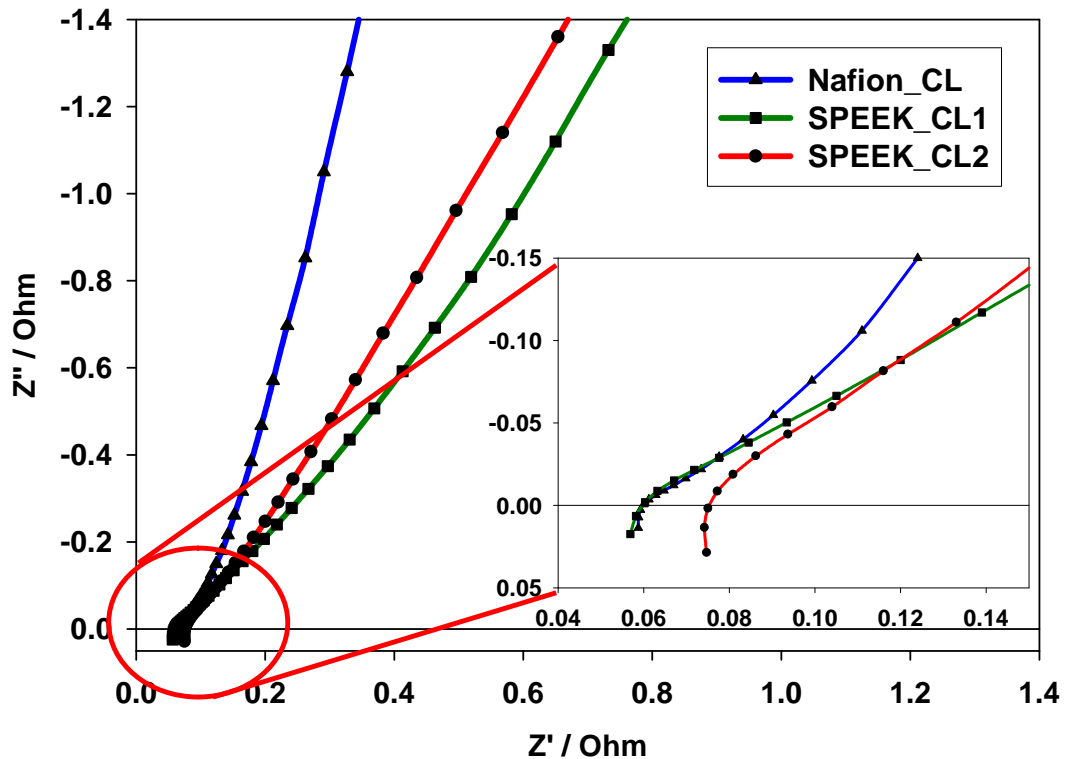


Figure 4.13: Nyquist EIS Response from 10 KHz - 0.1 Hz for Nafion\_CL, SPEEK\_CL1, and SPEEK\_CL2 at 0.45 V under  $N_2$ . High frequency intercept region shown in inset. 50<sup>o</sup>C cell,  $H_2/N_2$  100 % RH, and ambient pressure.

Determining the slope of  $|Z|$  vs.  $\omega^{-1/2}$  in **Figure 4.14**, and knowing the double layer capacitance charge (see **Figure 4.4**), the protonic resistance can be calculated (tabulated in Table 4.3) for each catalyst layer using equation 1.27.(86)

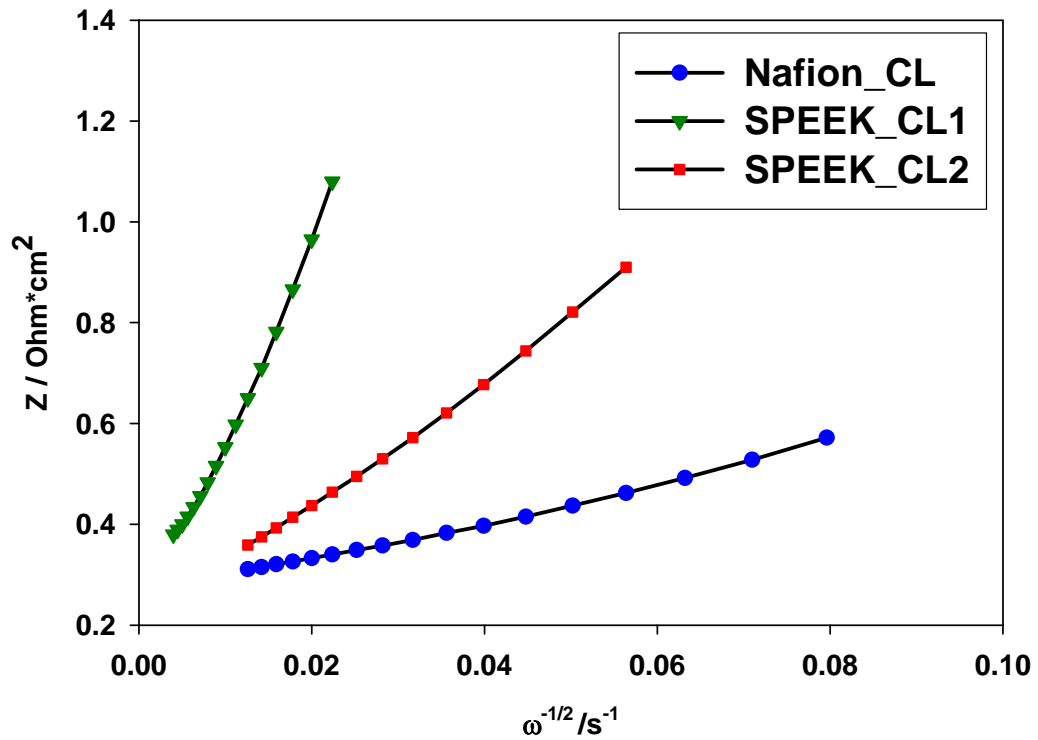


Figure 4.14: Modulus of the impedance vs.  $\omega^{-1/2}$ , taken from high frequency (10 K – 1 K Hz), for Nafion\_CL, SPEEK\_CL1 and SPEEK\_CL2.

**Table 4.3: Double layer capacitance, proton resistance and ionic conductivity for Nafion\_CL, SPEEK\_CL1 and SPEEK\_CL2 catalyst layers.**

<b>Catalyst Layer</b>	<b>C<sub>dl</sub></b> <b>mF cm<sup>-2</sup></b>	<b>R<sub>p</sub></b> <b>Ω*cm<sup>2</sup></b>	<b>σ<sub>H<sup>+</sup>,CL</sub></b> <b>mS cm<sup>-1</sup></b>
<b>Nafion_CL</b>	126 ± 7	2.21 ± 0.2	0.92 ± 0.07
<b>SPEEK_CL1</b>	22 ± 4	40.0 ± 5	0.050 ± 0.005
<b>SPEEK_CL2</b>	25 ± 4	33.3 ± 4	0.059 ± 0.005

According to experimental results, **Nafion\_CL** exhibits a lower specific protonic resistance, 2.21 Ω cm<sup>2</sup>, compared to **SPEEK\_CL1** (40.0 Ω cm<sup>2</sup>) and **SPEEK\_CL2** (33.3 Ω cm<sup>2</sup>). Calculated ionic conductivities of the catalyst layer are 0.92 mS cm<sup>-1</sup>, 0.050 mS cm<sup>-1</sup> and 0.059 mS cm<sup>-1</sup> for **Nafion\_CL**, **SPEEK\_CL1** and **SPEEK\_CL2**, respectively. Nafion<sup>®</sup> catalyst layer conductivities in this work are in agreement with values determined by Havranek *et al.*(86), Lefebvre *et al.*(123) and Springer *et al.*(124), when differences in catalyst composition are taken into account. SPEEK-based catalyst layers are ~18 times lower in conductivity than **Nafion\_CL**. This can be reasoned to be due to the combined effects of Nafion<sup>®</sup> having inherently higher bulk ionic conductivity (0.078 S cm<sup>-1</sup> at 25 °C in water) compared to SPEEK (0.041 S cm<sup>-1</sup> at 25 °C in water) and of the influence of the catalyst layer composition. Unlike the bulk PEM, the catalyst layer contains Pt/C and PTFE, so a lower conductivity is expected. The weight percent loading of Nafion<sup>®</sup> in the catalyst layer in this work

equates to 0.18 volume fraction, while **SPEEK\_CL1** and **SPEEK\_CL2** equals to 0.13 volume fraction. The larger volume fraction of Nafion<sup>®</sup> and larger inherent bulk conductivity provide justification for the higher conductivity found for **Nafion\_CL**. According to results presented in Table 4.3 **SPEEK\_CL1** possesses a lower protonic conductivity than **SPEEK\_CL2**. With both SPEEK catalyst layers containing the same ionomer content, results support that Method 2 fabrication procedure forms a more favorable microstructure for proton transport; this result is also supported by the larger ESA value determined for **SPEEK\_CL2**.

#### **4.3.7 Electrochemical Characterization of Varying Content SPEEK-based Catalyst Layers**

Since sufficient catalyst layer conductivity is essential to minimize cathode activation losses, the effect of increasing the ionic conductivity by increasing electrolyte content was studied. Similar studies have been performed for Nafion<sup>®</sup> catalyst layers,(51, 116) but literature results specific for SPEEK-based catalyst layers are limited. To further understand the dependence on electrolyte content, **SPEEK\_CL1** catalyst layers containing 10, 20, 30 and 40 wt% solid polymer electrolyte content were fabricated using Method 1, and were characterized using CV and EIS techniques previously outlined. **Figure 4.15** illustrates the fuel cell polarization performance for each sample.

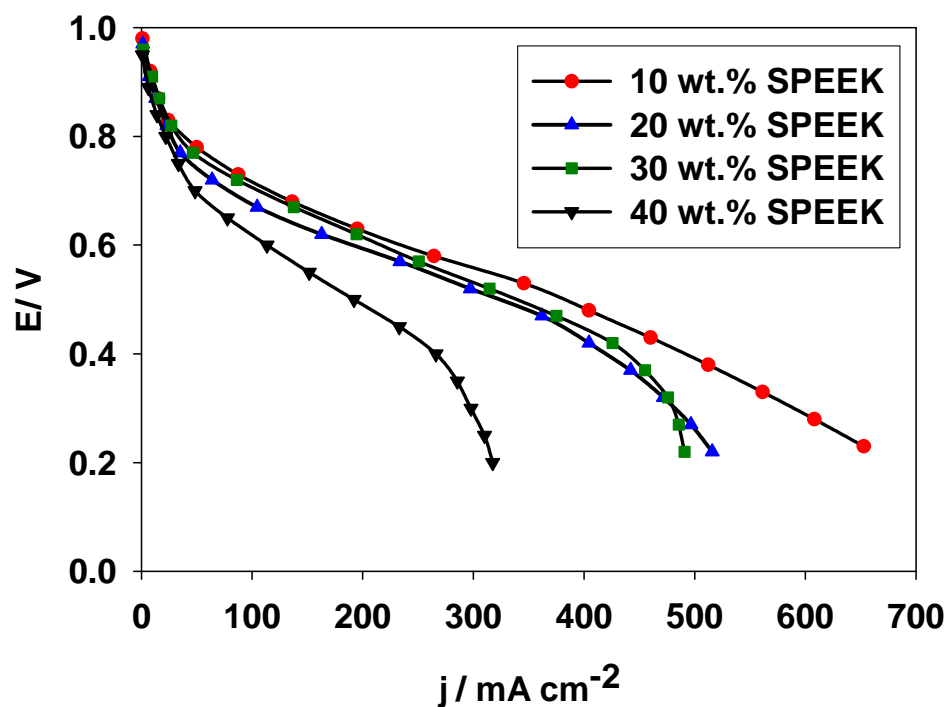


Figure 4.15: 5 cm<sup>2</sup> polarization performance for SPEEK\_CL1 cathodes with ionomer content of 10 (●), 20 (▲), 30 (■) and 40 (▼) wt%. 50 °C cell, 0.2 L/min H<sub>2</sub>/O<sub>2</sub> 100 % RH, and atmospheric pressure.

Polarization data shows that performances decrease across the entire current density region when the SPEEK content is increased. This confirms results by Easton *et al.*(60), wherein the optimized weight content of SPEEK ionomer in the catalyst layer was determined to be between 10 - 15 wt% based on the limiting capacitance being maximum at this weight content. However, the relationship between catalyst layer protonic conductivity and weight content was not studied previously.

Cyclic voltammetry and EIS experiments were utilized to determine the ESA and proton conductivity of each different cathode. The respective cyclic

voltammograms can be seen in **Figure 4.16**, and were used to calculate ESA and double layer charging values, which are presented in Table 4.4. EIS experiments allowed the proton resistance and conductivity to be determined for each catalyst layer (also presented in Table 4.4).

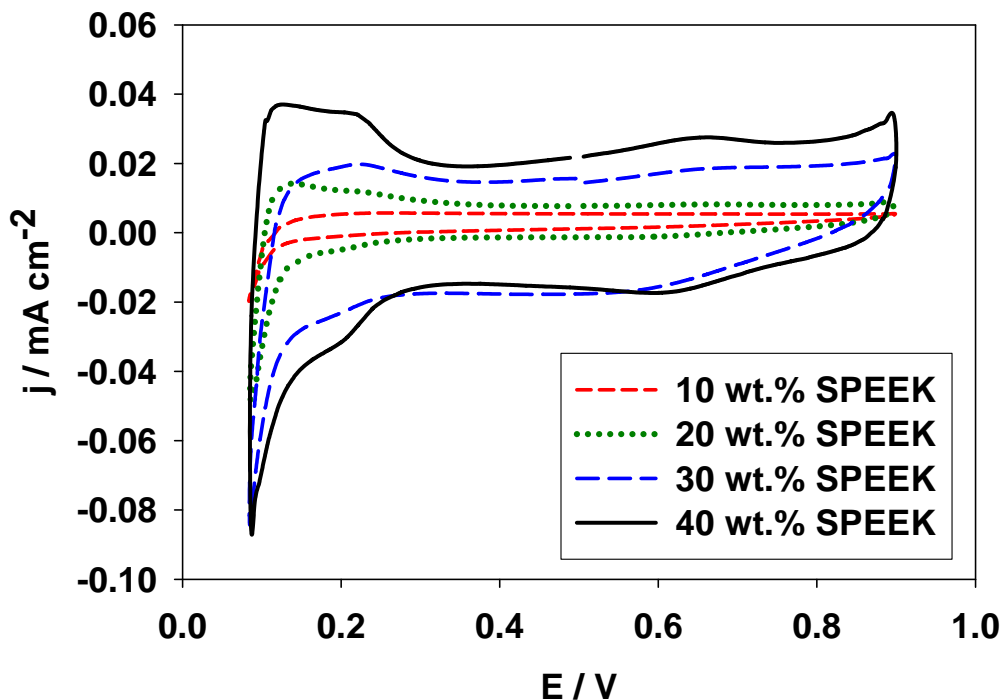


Figure 4.16: Cyclic voltammograms of SPEEK\_CL1 with electrolyte content of 10 (short dash), 20 (dotted), 30 (long dash) and 40 (solid) wt% SPEEK. 50 °C cell temperature,  $\text{N}_2/\text{H}_2$  0/0.2  $\text{L min}^{-1}$  100 % RH, scan rate  $50 \text{ mV s}^{-1}$ , and a potential window 0.04 – 0.9 V vs. SHE.

**Table 4.4: Double layer capacitance charge, ESA, CL proton resistance, and CL conductivity for SPEEK\_CL1 containing increasing SPEEK weight content.**

<b>Catalyst Layer (ionomer wt%)</b>	<b>C<sub>dl</sub> mF cm<sup>-2</sup></b>	<b>ESA m<sup>2</sup> g<sup>-1</sup></b>	<b>R<sub>p</sub> Ω cm<sup>2</sup></b>	<b>σ<sub>H<sup>+</sup>, CL</sub> mS cm<sup>-1</sup></b>
<b>SPEEK_CL1 (10 wt%)</b>	25 ± 4	11 ± 2	50 ± 4	0.040 ± 0.005
<b>SPEEK_CL1 (20 wt%)</b>	39 ± 5	23 ± 3	38 ± 4	0.052 ± 0.006
<b>SPEEK_CL1 (30 wt%)</b>	120 ± 7	27 ± 3	30 ± 4	0.067 ± 0.005
<b>SPEEK_CL1 (40 wt%)</b>	140 ± 8	46 ± 4	3.6 ± 0.6	0.56 ± 0.06

Both ESA and conductivity values increase with increasing SPEEK weight content. This can be rationalized to be due to increased SPEEK content facilitating a more continuous pathway for proton transport; increasing the contact between Pt/C and ionomer as seen with increasing double layer charging current for the cyclic voltammograms. A similar trend of increasing ionic conductivity in the catalyst layer with increasing electrolyte content has been seen by Lefebvre *et al.*(123) and Xie *et al.*(116), however SPEEK catalyst layers possessed lower ionic conductivity than these published works. At present this deviation can not be accounted for, but results allow a comparison for increasing SPEEK-based catalyst layers to be made as experimental reproducibility is high.

To account for the varying volume fraction of SPEEK electrolyte in each catalyst layer, the proton conductivity in Table 4.4 was normalized to a volume fraction, and compared to the bulk SPEEK membrane electrolyte conductivity

(Table 2.1) by calculating the ratio of catalyst layer conductivity to bulk conductivity, as seen in Table 4.5.

**Table 4.5: CL conductivity normalized to volume fraction of electrolyte in each SPEEK\_CL1 and comparison to bulk SPEEK electrolyte conductivity.**

<b>SPEEK_CL1 ionomer wt%</b>	<b>CL <math>\sigma_{H^+}</math>, CL mS cm<sup>-1</sup></b>	<b>CL <math>\sigma_{H^+}</math> Normalized to Ionomer Volume mS cm<sup>-1</sup></b>	<b>Ratio CL/Bulk <math>\sigma_{H^+}</math> %</b>
<b>10</b>	0.040 ± 0.005	0.31 ± 0.04	0.75 ± 0.06
<b>20</b>	0.052 ± 0.006	0.28 ± 0.04	0.74 ± 0.07
<b>30</b>	0.067 ± 0.005	0.24 ± 0.04	0.54 ± 0.06
<b>40</b>	0.56 ± 0.06	1.19 ± 0.05	2.90 ± 0.12

Normalized **SPEEK\_CL1** conductivity values show a noticeable transition to higher values when the electrolyte content is increased from 30 to 40 wt%, this jump is of the order of ~5 times. This reflects the importance of the SPEEK content and the volume fraction necessary to achieve a suitable degree of percolation for the ionic component. The low conductivity values for SPEEK loadings of 10 to 30 wt% indicate that the connectivity of acidic groups is poor when the ionomer is deposited in the presence of Pt/C catalyst. Furthermore, even when the ionomer content is 40 wt%, i.e., sufficient to produce a percolation network of ionomer, the conductivity of SPEEK inside the catalyst layer is only ~

3% of that of the bulk electrolyte. These results indicate that the presence of Pt/C particles affect the proton conductivity of the ionomer inside the catalyst layer. The precise reason for this is as yet unknown but it may be due to the nature of adsorption of SPEEK on the Pt/C catalyst, its distribution within the catalyst layer, and the extent of dissociation of the acid groups.

Although higher SPEEK content enhances proton conductivity and ESA values, it proves detrimental to fuel cell performance, as seen with the superior performance of the 10 wt% **SPEEK\_CL1** in **Figure 4.15**. The large difference between the conductivity for 30 and 40 wt% SPEEK electrolyte catalyst layers reveal that the content of electrolyte has significant impact the ionic percolation in the catalyst layer, future considerations towards mathematically modeling the catalyst layer, in order to determine the percolation threshold for each electrolyte content, may reveal a strong correspondence to the observed experimental data seen here. The ionic conductivity for 40 wt% **SPEEK\_CL1** approaches the conductivity value for the Nafion<sup>®</sup> based catalyst layer result (0.1 mS $\text{cm}^{-2}$ ) observed by Lefebvre *et al.*(123), and supports that the transmission line analysis technique used is valid for SPEEK-based catalyst layer conductivity calculations.

To account for the interplay of materials in the electrode for providing the most effective pathway throughout the electrode for each reactant; the effect of SPEEK content towards mass transport limitations in the catalyst was also considered. The presence of excessive SPEEK may restrict the amount of gaseous pathways available for oxidant transport, overwhelming the beneficial

characteristics of increasing proton conductivity and higher ESA. Poltarzewski *et al.*(115) and Uchida *et al.*(110) confirm a comparable result for Nafion<sup>®</sup>-based systems, with the optimal ratio of Nafion<sup>®</sup> ionomer to the total weight (Pt/C + dry Nafion<sup>®</sup>) being 30 – 40 wt%. A similar phenomenon of reduced void space for reactant diffusion resulting from excessive Nafion<sup>®</sup> in the catalyst layer has also been reported by Xie *et al.*(116), where excessive Nafion<sup>®</sup> added to the catalyst layer blocks the pores required for gaseous oxygen diffusion.

In order to estimate the effective properties of each SPEEK-based catalyst layer, the differences in void volume fraction were determined from CL composition analysis. The cumulative solid phase volume fraction in the catalyst layer can be calculated knowing the mass loading for Pt, carbon, PTFE and electrolyte, the catalyst layer thickness, and the densities of Pt (21.45 mg cm<sup>-3</sup>), carbon (1.8 mg cm<sup>-3</sup>), PTFE ( 0.9 mg cm<sup>-3</sup>), Nafion<sup>®</sup> ( 2.0 mg cm<sup>-3</sup>) and SPEEK 1.88 (1.2 mg cm<sup>-3</sup> ).(20, 100) The resulting void fraction,  $V_{\text{void}}$ , in the catalyst layer for oxygen diffusion is then obtained from equation 4.4.

$$V_{\text{void}} = 1 - V_{\text{Pt}} - V_{\text{C}} - V_{\text{PTFE}} - V_{\text{Ionomer}} \quad (4.4)$$

This void fraction volume can be interpreted as the volume fraction of the catalyst layer available for gaseous oxygen transport or water transport. Representative volumes for each component in each SPEEK catalyst layer are depicted in **Figure 4.17; Nafion\_CLs** composition is also shown for comparison.

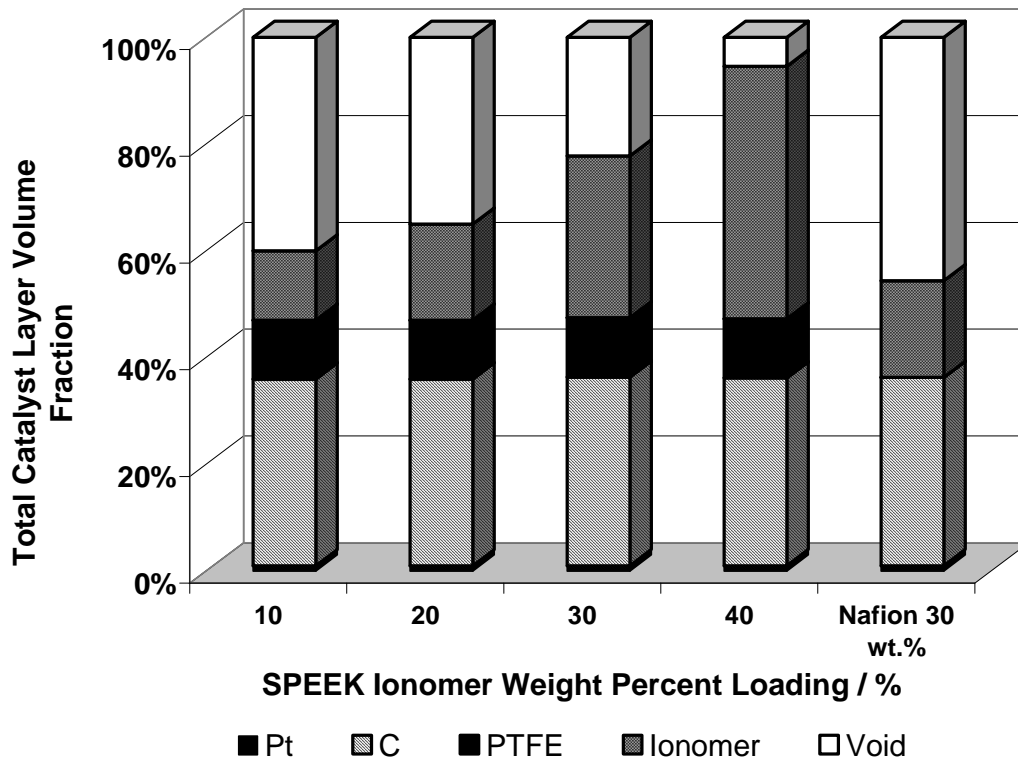


Figure 4.17: Compositional analysis for Nafion\_CL and increasing ionomer content SPEEK\_CL1.

Results show that increasing the SPEEK content from 10 to 40 wt% decreases the void fraction in the catalyst layer from 40 % to 6 %. With values as low as 6 % void fraction, secondary pores responsible for the gas diffusivity and water management in the catalyst layer will be minimal. Previous literature in regards to determining the optimum composition for Nafion<sup>®</sup> catalyst layers find the optimum void volume to be 30 - 36 %.(20, 54, 70) Comparing SPEEK and Nafion<sup>®</sup> catalyst layers of similar weight ionomer content, it is seen that SPEEK catalyst layers suffer from reduced porosity due to a lower void volume. For example, for an ionomer weight content of thirty percent, the void volume of

**Nafion\_CL** is 45 % compared to 22 % for **SPEEK\_CL1**. This significant difference in void space for reactant transport and water management can be accounted for by the lower density of SPEEK ( $1.20 \text{ mg cm}^{-3}$ ) compared to Nafion<sup>®</sup> ( $2.0 \text{ mg cm}^{-3}$ ). As a consequence, the differences in ionomer density, and the additional presence of PTFE, result in a significantly lower void pore volume for SPEEK catalyst layers, demonstrating the limitation towards oxygen and water transport, and thus potential mass transport limitations.

Considerations of the different hydrophobicity of each electrolyte must also be noted, as the affinity for retaining water in the catalyst layer will additionally influence the mass transport. SPEEKs hydrocarbon backbone is less hydrophobic than Nafion<sup>®</sup>. Combined with the larger content of sulfonic acid groups, SPEEK ionomer is expected to retain more water due to its higher affinity for water. With smaller void fractions at comparable loadings to Nafion<sup>®</sup>, SPEEK catalyst layers will likely suffer from water management limitations and flooding. For this reason, addition of the hydrophobic PTFE to SPEEK ionomer catalyst layers is essential to facilitate water management. Easton *et al.*(60) supports incorporation of PTFE, showing increased performance for SPEEK catalyst layers due to increased hydrophobic character reducing mass transport limitations. Considerations to sintering PTFE must also be noted, as catalyst layers fabricated by Method 1 show increased hydrophobicity from the thermal treatment step. A more hydrophobic character may lead to reduced mass transport limitations due to better water management and higher fuel cell

performance, a case observed for sintered **SPEEK\_CL1** compared to unsintered **SPEEK\_CL2**.

The onset of mass transport limitations for varying electrolyte content **SPEEK\_CL1** catalyst layers was determined by electronic impedance spectroscopy. EIS experiments were performed in a H<sub>2</sub>/O<sub>2</sub> fuel cell at increasing operational current densities to quantify the total ionic and electronic resistance, R<sub>T</sub>, of the MEA, which includes the following summation of resistances:

$$R_T = R_U + R_{CT} + R_{MT} \quad (4.1)$$

where R<sub>U</sub> represents the uncompensated resistance (membrane resistance, cell resistance, and cell hardware resistance), R<sub>CT</sub> is the charge transfer resistance and R<sub>MT</sub> is the mass transport resistance in the catalyst layer. Typical Nyquist impedance responses for **SPEEK\_CL1** catalyst layers at increasing operational current can be seen in **Figure 4.18**. Features of each Nyquist plot include a shift of the real impedance from the origin due to R<sub>U</sub>, and an arc resulting from a charge transfer response and mass transport response. The rapid H<sub>2</sub> kinetics result in a negligible impedance contribution from the anode, allowing any differences observed in the Nyquist plot to be attributed to the varying cathode catalyst layers.(125)

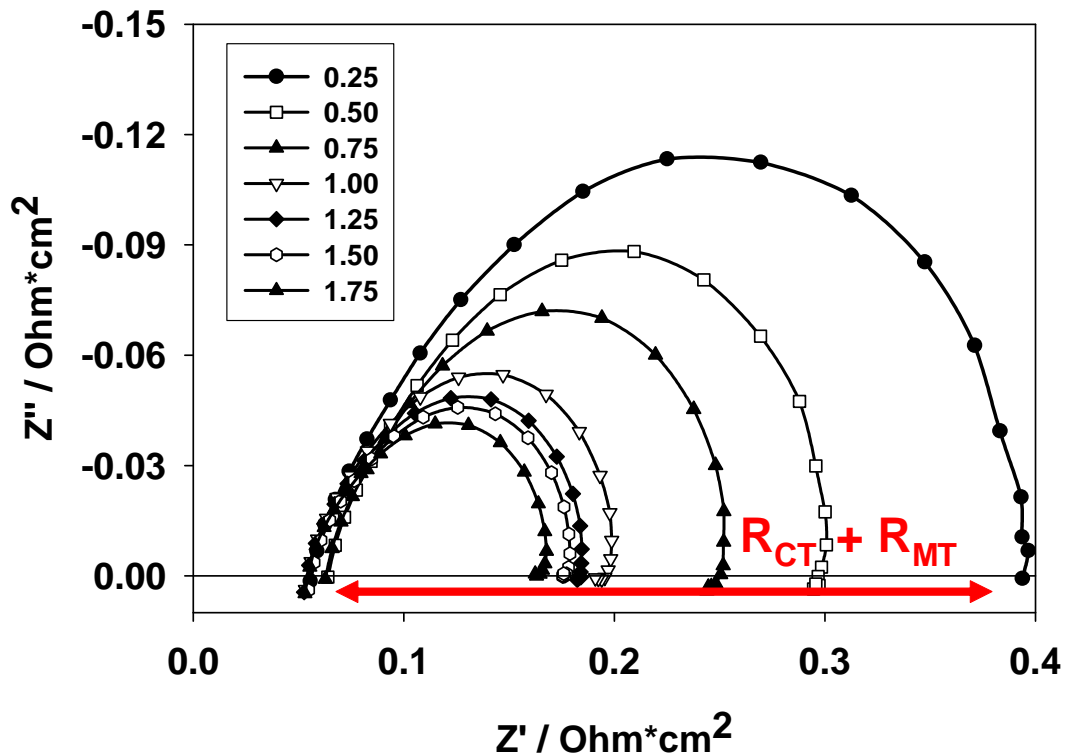


Figure 4.18: EIS Nyquist response for SPEEK\_CL1 catalyst layer 10 wt% SPEEK, at increasing cell current (A).  $\text{H}_2/\text{O}_2$  at  $0.2 \text{ L min}^{-1}$  and  $50^\circ \text{C}$  cell temperature.

The EIS arc response represents the combined magnitude of the charge transfer resistance,  $R_{CT}$ , and mass transfer resistance,  $R_{MT}$ , occurring in cathode under  $\text{H}_2/\text{O}_2$ . At high current densities, the contribution from the charge transfer resistance can be deemed negligible since the cathode kinetics are fast, the remaining resistance can be attributed to oxygen diffusion to active Pt sites. The transition from charge transfer to mass transport limitations can be seen by plotting the real resistance ( $Z'$ ) vs. current density for each **SPEEK\_CL1** cathode as seen in **Figure 4.19**.

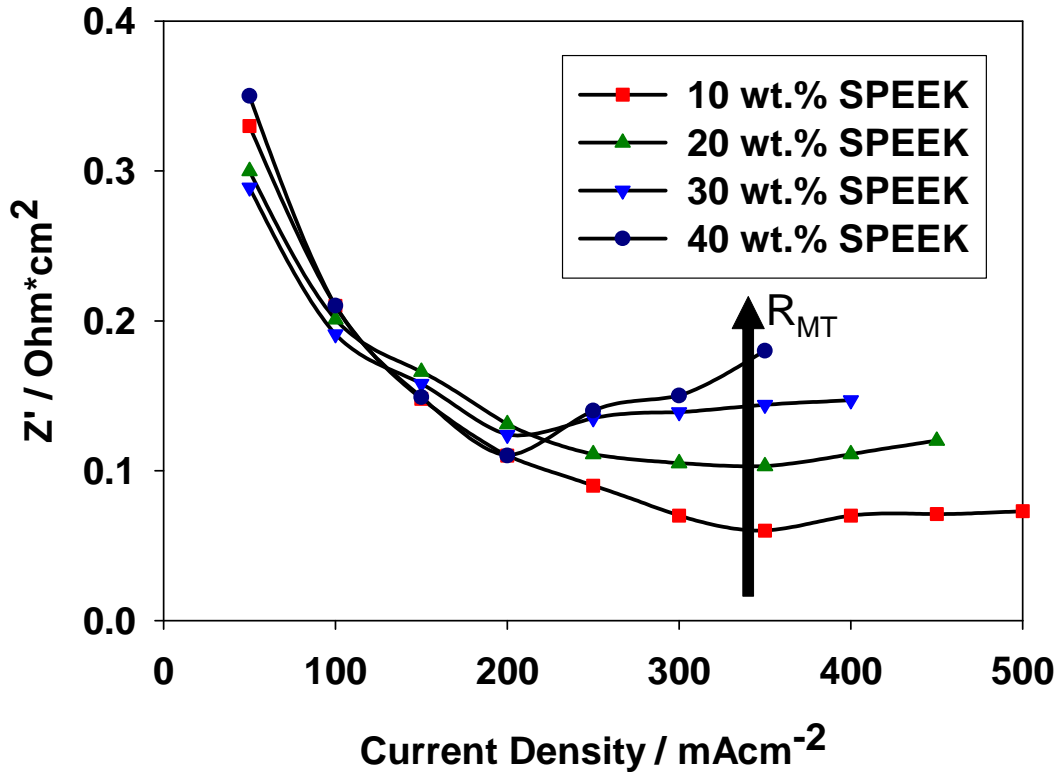


Figure 4.19: Variance of total ionic and electronic resistance in the cathode determined from EIS data for SPEEK\_CL1 with 10 (■), 20 (▲), 30 (▼), and 40 (●) weight percent SPEEK.

The transition to the mass transfer controlled regime is indicated by the change in slope in **Figure 4.19** at  $\sim 200 \text{ mA cm}^{-2}$ , this change is indicative of the transition from  $R_{CT}$  to  $R_{MT}$  resistance dominating. The highest SPEEK loading catalyst layers (30 and 40 wt%) show significantly larger mass transfer limitations than the lower weight content catalyst layers. This is illustrated by comparing the real resistance ( $Z'$ ) at the fixed current density of  $350 \text{ mA cm}^{-2}$  in **Figure 4.19**. This current density is representative of the mass transfer controlled regime of the polarization curve for each MEA, and it can be observed that the mass transport resistance increases linearly with increasing electrolyte content. As is

evident in Table 4.4 and **Figure 4.19**, the influence of SPEEK content in the catalyst layer has a significant impact on ESA, proton conductivity, and mass transport resistance. Higher loadings of SPEEK electrolyte in the catalyst layer support higher ESA and proton conductivity values, but stronger mass transport resistance.

#### **4.4 Conclusion**

Under fuel cell operating conditions, the influence of SPEEK ionomer electrolyte has a significant influence on the electrochemical performance of fuel cell cathodes. The effect of SPEEK ionomer on the electrochemically active surface area, proton conductivity in the catalyst layer, oxygen mass transport properties and water management has been extensively studied in this work. Compared to Nafion<sup>®</sup>-based catalyst layers, SPEEK-based catalyst layers exhibit greater overpotential limitations and lower performing PEMFCs.

Measurements performed in an operating fuel cell by means of cyclic voltammetry, electrochemical impedance spectroscopy and current-potential polarization allow the primary limitations of SPEEK-based catalyst layers to be quantified. Results show a strong low ESA values and protonic conductivity of SPEEK-based catalyst layers, attributed to the lower inherent bulk conductivity of SPEEK, reduced ionic connectivity in the CL, and a stronger blocking effect of active Pt sites compared to Nafion<sup>®</sup>. Use of a novel fabrication technique to obtain a homogeneously distributed catalyst layer, outlined as Method 2, was ineffective in reducing the performance gap between Nafion<sup>®</sup>- and SPEEK-based

catalyst layers, possibly due to un-sintered PTFE not possessing sufficient hydrophobic character to prevent mass transport limitations.

Additional ex-situ studies revealed that the use of a non-traditional solvent system, such as DMAc, required to dissolve SPEEK is detrimental to the ESA, marginally lowering the ESA. However this experimental observation doesn't account for the large reduction in ESA when comparing SPEEK-based and Nafion<sup>®</sup>-based catalyst layers. Rather the interplay between solvent choice, the electrolyte content, ink impurities, operating conditions and fabrication method for the SPEEK catalyst layers dictate the overall active area.

Studies of SPEEK-based catalyst layers with increased electrolyte content showed increased ESA and proton conductivity. However, the offset in mass transport limitations was more severe, and catalyst layers with high SPEEK contents suffered from limitations due to reduced oxygen diffusion and increased hydrophilic properties leading to poorer water management. The present work suggests that the SPEEK ionomer of 1.88 IEC with a 10 wt% weight loading was the most suitable as the solid polymer electrolyte in the cathode. For high performance fuel cells comparable to Nafion<sup>®</sup>, SPEEK-based catalyst layers need to be improved to have higher proton conductivity, higher gas permeability, and better water management properties.

## CHAPTER 5: CONCLUSION AND FUTURE WORK

In this thesis, the effect of a novel hydrocarbon based cathode of a proton exchange membrane fuel cell has been investigated. Sulfonated poly(ether ether ketone) (SPEEK) was selected as the electrolyte and characterized under fuel cell conditions, acting as both the PEM and catalyst layer solid electrolyte. The influence towards the catalyst layer microstructure, electronically active area, catalyst layer proton conductivity, and mass transport limitation for SPEEK electrolyte were studied.

The effects of temperature on the electrochemical reduction of oxygen at a Pt | PEM interface has been successfully investigated for SPEEK and Nafion<sup>®</sup> membranes using chronoamperometry and slow-sweep voltammetry in a solid-state electrochemical cell. Mass transport (oxygen solubility, diffusion coefficient, and permeability) and kinetic (exchange current density, Tafel slope, and transfer coefficient) parameters of SPEEK membranes have been studied as a function of the IEC and temperature. Limiting current densities for the ORR indicate a stronger mass transport limitation for all SPEEK membranes studied compared to Nafion<sup>®</sup>. Differences in oxygen kinetic and mass transport parameters have been attributed to the properties of the polymer membranes and the associated differences in oxygen solubility and diffusion coefficients values. Nafion<sup>®</sup> membranes were found to have larger oxygen permeability coefficients compared to all SPEEK membranes. Increasing the IEC for SPEEK membranes

resulted in oxygen diffusion coefficients increasing due to larger water content in the membrane, while oxygen solubility decreased due to the reduced hydrophobic character. Future considerations towards correlating the water content and the phase separation of the electrolyte may allow improvement in selecting the solid polymer electrolyte in regards to oxygen mass transport properties. Quantifying oxygen transport properties for varying electrolytes of varying degrees of tortuosity, investigated by imaging the stained electrolyte using transmission electron microscopy, may further direct the choice of electrolyte in the catalyst layer if a strong correlation is observed between the water channel pathway and oxygen diffusion parameter. Comparing the Tafel plots for oxygen reduction at the Pt| membrane interface, both membranes display two Tafel slopes corresponding to oxide covered and oxide free Pt surfaces at all temperatures studied. Nafion<sup>®</sup> 117 possesses a higher exchange current density for low and high current density regions compared to all SPEEK membranes, indicating a faster rate for the oxygen reduction reaction.

In addition to investigating the oxygen mass transport properties of SPEEK membranes, this thesis also highlights the physical differences in microstructure between catalyst layers fabricated with Nafion<sup>®</sup> or SPEEK electrolyte. SPEEK catalyst layers have a larger macropore peak pore size compared to Nafion<sup>®</sup>. A novel fabrication method for SPEEK-based catalyst layers was developed, and shown to lead to catalyst layers possessing similar peak pore size but dramatically reduced hydrophobic properties compared to ones prepared by the traditional fabrication method. Contact angle analysis

confirms that sintering PTFE increases the hydrophobic property of the catalyst layer, but restricts the fabrication method to a graded distribution approach for the electrolyte in the catalyst layer. In view of the fact that catalyst layers require additional hydrophobic character for less hydrophobic electrolytes such as SPEEK, future considerations of hydrophobic materials that have sintering temperatures compatible within the electrolytes' thermal stability range are worthwhile pursuing if a simultaneous ink fabrication method is desired. Additionally, a strong effect of solvent choice on the catalyst layer surface morphology has been observed for catalyst layers. Although SEM micrographs allowed observation of the differences in SPEEK-based catalyst layers prepared from different solvent compositions, a future study utilizing higher magnification or the use of environmental scanning electron microscopy may allow the electrochemical differences between the emulsion based Nafion<sup>®</sup> ink and the solubilized SPEEK ink to be explained based on observed differences in how the ionomer is deposited on the catalyst particles. With catalyst layer morphology and porosity determining mass transport limitations, electrolyte emulsions devoid of high boiling solvents/dispersion media may be necessary.

SPEEK-based cathodes prepared from both fabrication methods exhibit lower fuel cell current densities compared to a Nafion<sup>®</sup>-based cathode. Electrochemical characterization of the SPEEK-based cathodes yields lower electrochemical surface areas, lower catalyst layer proton conductivities and larger mass transport limitations. Development of a more homogeneously distributed catalyst layer using a novel fabrication technique was ineffective in

meeting the performance of Nafion<sup>®</sup> catalyst layers, the lower performance possibly being due to non-sintered PTFE possessing insufficient hydrophobic character to prevent flooding. For SPEEK catalyst layers, larger SPEEK content leads to improved ESA and proton conductivity but significant mass transport limitations. EIS experiments confirmed that catalyst layers containing high SPEEK content suffer limitations due to reduced oxygen diffusion through their reduced porosity. Experimental results for SPEEK-based catalyst layers reflect that the optimum electrolyte content will depend on the electrolytes oxygen mass transport properties, water transport, platinum coverage and catalyst layer proton conductivity. It can be seen that increasing SPEEK electrolyte content decreased the specific volume of available macropores due to reduced free volume, thereby restricting the mass transport of oxygen. The poor oxygen permeability of SPEEK, and the high loading required for enhanced ESA and proton conductivity, all serve to limit mass transport of SPEEK-based catalyst layers. Development of a denser, more hydrophobic electrolyte with ideally higher conductivity may result in higher performing non-Nafion<sup>®</sup> electrolyte cathodes. For example, the use of a SPEEK block co-polymer consisting of both a hydrophobic block and hydrophilic moieties may favor a larger extent of phase separation increasing water transport and oxygen permeability in the hydrophobic environment, while maintaining suitable proton transport properties in the hydrophilic domains.

Although the SPEEK-based catalyst layers used in this study were shown to have limited oxygen permeability, proton conductivity and Pt utilization in the

cathode, the results provide insightful information on the influence of a hydrocarbon electrolyte in a working PEM fuel cell. Further studies dedicated to the design of new polymers or new microstructures in the catalyst layer, with different inherent physical and electrochemical properties to Nafion<sup>®</sup>, will aid in the development of materials and fabrication procedures with characteristics better suited for future fuel cell operation. In future work, the choice of the electrolyte in the catalyst layer must include a complete assessment of both its physical and electrochemical properties, as the dramatic differences seen in this work for SPEEK electrolyte when compared to Nafion<sup>®</sup> reveal the importance of electrolyte choice. In the design of a new electrolyte, the move towards a chemical structure utilizing a pendant side chain that allows greater phase separation to increase proton conductivity and oxygen mass transport, two parameters identified as limiting SPEEKs use, due to enhanced water transport may be advantageous.

With the complex environment of conflicting electrochemical, physical and morphological phenomena occurring in cathodes containing SPEEK electrolyte, as demonstrated in this thesis work, a future consideration is to use the experimentally determined parameters for the hydrocarbon electrolyte in a mathematical model describing fuel cell performance. By developing a model incorporating kinetic, mass transport and physical properties related to SPEEK further insight into the influence of the electrolyte can be attained, and the rate limiting processes in an operating fuel cell determined.

## REFERENCES

1. M. S. Whittingham, R. F. Savinell and T. Zawodzinski, *Chemical Reviews*, **104**, 4243 (2004).
2. M. L. Perry and T. F. Fuller, *Journal of The Electrochemical Society*, **149**, S59 (2002).
3. J. Larminie and A. Dicks, *Fuel Cell Systems Explained*, Wiley, West Sussex (2003).
4. M. A. Hickner, H. Ghassemi, Y. S. Kim, B. R. Einsla and J. E. McGrath, *Chemical Reviews*, **104**, 4587 (2004).
5. P. Costamagna and S. Srinivasan, *Journal of Power Sources*, **102**, 242 (2001).
6. D. R. Lide, *CRC Handbook of Chemistry and Physics*, CRC Press Inc., Cleveland (2002).
7. A. J. Bard and R. L. Faulkner, *Electrochemical Methods, Fundamentals and Applications*, Wiley Interscience, New York (2001).
8. K. R. Cooper, V. Ramani, J. M. Fenton and H. R. Kunz, *Experimental Methods and Data Analyses for Polymer Electrolyte Fuel Cells*, Scribner Associates Inc., North Carolina (2005).
9. J. Lipkowski and P. N. Ross., *Electrocatalysis*, Wiley, New York (1998).
10. J. P. Hoare, *The Electrochemistry of Oxygen* Interscience Publishers, New York (1968).
11. E. Yeager, *Electrochimica Acta*, **29**, 1527 (1984).
12. J. K. Nørskov, J. Rossmeisl, A. Logadottir, L. Lindqvist, J. R. Kitchin, T. Bligaard and H. Jonsson, Origin of the Overpotential for Oxygen Reduction at a Fuel-Cell Cathode, in, p. 17886 (2004).
13. K. Kinoshita, *Electrochemical Oxygen Technology*, Wiley, New York (1992).
14. B. E. Conway, H. Angerstein-Kozłowska, W. B. A. Sharp and E. E. Criddle, *Analytical Chemistry*, **45**, 1331 (1973).
15. K. L. Hsueh, D. T. Chin and S. Srinivasan, *Journal of Electroanalytical Chemistry*, **153**, 79 (1983).
16. A. Damjanovic, A. Dey and J. O. M. Bockris, *Electrochimica Acta*, **11**, 791 (1966).
17. A. Damjanovic and V. Brusic, *Electrochimica Acta*, **12**, 615 (1967).

18. A. Damjanovic, *The Journal of The Electrochemical Society*, **138**, 2315 (1991).
19. O. Antoine, Y. Bultel and R. Durand, *Journal of Electroanalytical Chemistry*, **499**, 85 (2001).
20. W. Vielstich, A. Lamm and H. A. Gasteiger, *Handbook of Fuel Cells: Fundamentals, Technology, and Applications* Wiley, Chichester, England (2003).
21. J. Appleby and R. L. Foulkes, *Fuel Cell Handbook*, Van Norstrand, New York (1989).
22. K. A. Mauritz and R. B. Moore, *Chemical Reviews*, **104**, 4535 (2004).
23. K. Prater, *Journal of Power Sources*, **29**, 239 (1990).
24. M. Eikerling, A. A. Kornyshev, A. M. Kuznetsov, J. Ulstrup and S. Walbran, *The Journal of Physical Chemistry B*, **105**, 3646 (2001).
25. K. D. Kreuer, S. J. Paddison, E. Spohr and M. Schuster, *Chemical Reviews*, **104**, 4637 (2004).
26. W. Y. Hsu and T. D. Gierke, *Journal of Membrane Science*, **13**, 307 (1983).
27. H. L. Yeager and A. Steck, *Journal of The Electrochemical Society*, **128**, 1880 (1981).
28. A. Z. Weber and J. Newman, *Journal of The Electrochemical Society*, **150**, A1008 (2003).
29. J. Divisek, M. Eikerling, V. Mazin, H. Schmitz, U. Stimming and Y. M. Volfkovich, *Journal of The Electrochemical Society*, **145**, 2677 (1998).
30. K. D. Kreuer, *Journal of Membrane Science*, **185**, 29 (2001).
31. K. D. Kreuer, *Solid State Ionics*, **136-137**, 149 (2000).
32. K. D. Kreuer, *Solid State Ionics*, **94**, 55 (1997).
33. B. S. Pivovar, *Polymer*, **47**, 4194 (2006).
34. B. S. P. M. A. Hickner, The Chemical and Structural Nature of Proton Exchange Membrane Fuel Cell Properties, in, p. 213 (2005).
35. L. Jörissen, V. Gogel, J. Kerres and J. Garche, *Journal of Power Sources*, **105**, 267 (2002).
36. O. Savadogo, *Journal of Power Sources*, **127**, 135 (2004).
37. M. Rikukawa and K. Sanui, *Progress in Polymer Science*, **25**, 1463 (2000).
38. R. Jiang, H. R. Kunz and J. M. Fenton, *Journal of Power Sources*, **150**, 120 (2005).

39. S. Kaliaguine, S. D. Mikhailenko, K. P. Wang, P. Xing, G. Robertson and M. Guiver, *Catalysis Today*, **82**, 213 (2003).
40. B. Yang and A. Manthiram, *Electrochemical and Solid State Letters*, **6**, A229 (2003).
41. B. Smitha, S. Sridhar and A. A. Khan, *Journal of Membrane Science*, **225**, 63 (2003).
42. C. Ma, L. Zhang, S. Mukerjee, D. Ofer and B. Nair, *Journal of Membrane Science*, **219**, 123 (2003).
43. L. Zhang, C. Ma and S. Mukerjee, *Electrochimica Acta*, **48**, 1845 (2003).
44. D. J. Jones and J. Roziere, *Journal of Membrane Science*, **185**, 41 (2001).
45. D. J. Jones, F. Grasset, M. Marrony, J. Rozière and X. Glipa, *Fuel Cells Bulletin*, **2005**, 12 (2005).
46. D. J. Jones and J. Rozière, *Journal of Membrane Science*, **185**, 41 (2001).
47. D. J. Jones, J. Rozière, M. Marrony, C. Lamy, C. Coutanceau, J.-M. Léger, H. Hutchinson and M. Dupont, *Fuel Cells Bulletin*, **2005**, 12 (2005).
48. Y. Fu, A. Manthiram and M. D. Guiver, *Electrochemistry Communications*, **8**, 1386 (2006).
49. M. Aoki, Y. Chikashige, K. Miyatake, H. Uchida and M. Watanabe, *Electrochemistry Communications*, **8**, 1412 (2006).
50. E. Antolini, *Journal of Applied Electrochemistry*, **34**, 563 (2004).
51. E. Antolini, L. Giorgi, A. Pozio and E. Passalacqua, *Journal of Power Sources*, **77**, 136 (1999).
52. E. Passalacqua, F. Lufrano, G. Squadrito, A. Patti and L. Giorgi, *Electrochimica Acta*, **43**, 3665 (1998).
53. S. Litster and G. McLean, *Journal of Power Sources*, **130**, 61 (2004).
54. Z. Qi and A. Kaufman, *Journal of Power Sources*, **113**, 37 (2003).
55. E. B. Easton, Z. Qi, A. Kaufman and P. Pickup, *Electrochemical and Solid State Letters*, **4**, A59 (2001).
56. S. Mukerjee and S. Srinivasan, *Journal of Electroanalytical Chemistry*, **357**, 201 (1993).
57. A. S. Arico, A. Stassi, E. Modica, R. Ornelas, I. Gatto, E. Passalacqua and V. Antonucci, *Journal of Power Sources*, **178**, 525 (2008).
58. V. R. Stamenkovic, B. Fowler, B. S. Mun, G. Wang, P. N. Ross, C. A. Lucas and N. M. Markovic, *Science*, **315**, 493 (2007).

59. H. A. Gasteiger, S. S. Kocha, B. Sompalli and F. T. Wagner, *Applied Catalysis B: Environmental*, **56**, 9 (2005).
60. E. B. Easton, T. D. Astill and S. Holdcroft, *Journal of The Electrochemical Society*, **152**, A752 (2005).
61. Y. S. Kim, M. Sankir, J. Chlistunoff, J. McGrath and B. Pivovar, in *209th ECS Meeting Abstract #1089*, C. Bock, I. Fritsch, B. Marsan and M. Mench Editors (2006).
62. S. v. Kraemer, M. Pucher, P. Jannasch, A. Lundblad and G. Lindbergh, *Journal of The Electrochemical Society*, **153**, A2077 (2006).
63. A. B. Beleke, K. Miyatake, H. Uchida and M. Watanabe, *Electrochimica Acta*, **53**, 1972 (2007).
64. S. K. Sambandam and V. Ramani, *ECS Transactions*, **11**, 105 (2007).
65. V. Ramani, S. Swier, M. T. Shaw, R. A. Weiss, H. R. Kunz and J. M. Fenton, *Journal of The Electrochemical Society*, **155**, B532 (2008).
66. H. Y. Jung, K. Y. Cho, K. A. Sung, W. K. Kim and J. K. Park, *Journal of Power Sources*, **163**, 56 (2006).
67. H. Y. Jung, K. Y. Cho, K. Sung, W. K. Kim, M. Kurkuri and J.-K. Park, *Electrochimica Acta*, **52**, 4916 (2007).
68. K. Scott, W. M. Taama and P. Argyropoulos, *Journal of Membrane Science*, **171**, 119 (2000).
69. J. Goldstein, D. Newbury, P. Echlin and D. Joy, *Scanning Electron Microscopy and X-Ray Microanalysis*, Kluwer Academic, New York (2003).
70. P. Gode, F. Jaouen, G. Lindbergh, A. Lundblad and G. Sundholm, *Electrochimica Acta*, **48**, 4175 (2003).
71. E. W. Washburn, *Physical Review*, **17**, 273 (1921).
72. F. Rouquerol, J. Rouquerol and K. Sing, *Adsorption by Powders and Porous Solids*, Academic Press, Cambridge (1999).
73. Z. Zhang, L. Qu and G. Shi, *Journal of Materials Chemistry*, **13**, 2858 (2003).
74. B. He, N. A. Patankar and J. Lee, *Langmuir*, **19**, 4999 (2003).
75. Y. Sutjiadi-Sia, P. Jaeger and R. Eggers, *Journal of Colloid and Interface Science*, **320**, 268 (2008).
76. T. Young, *Philosophical Transactions of the Royal Society of London (1776-1886)*, **95**, 65 (1805).
77. V. Basura, P. Beattie and S. Holdcroft, *Journal of Electroanalytical Chemistry*, **458**, 1 (1998).

78. A. Parthasarathy, S. Srinivasan, A. J. Appleby and C. R. Martin, *Journal of The Electrochemical Society*, **139**, 2530 (1992).
79. A. Parthasarathy, S. Srinivasan, A. J. Appleby and C. R. Martin, *Journal of The Electrochemical Society*, **139**, 2856 (1992).
80. M. I. Montenegro, M. A. Queiros and J. Daschbach, *Microelectrodes: Theory and Applications*, Kluwer Academic Publishers, London (1991).
81. C. P. Winlove, K. H. Parker and R. K. C. Oxenham, *Journal of Electroanalytical Chemistry*, **170**, 293 (1984).
82. R. N. Carter, S. S. Kocha, F. Wagner, M. Fay and H. A. Gasteiger, *ECS Transactions*, **11**, 403 (2007).
83. P. Ferreira-Aparicio, *Chemical Materials*, **19**, 6030 (2007).
84. E. Barsoukov and J. R. Macdonald, *Impedance Spectroscopy Theory, Experiment, and Applications*, Wiley-Interscience, New Jersey (2005).
85. M. Eikerling and A. A. Kornyshev, *Journal of Electroanalytical Chemistry*, **475**, 107 (1999).
86. A. Havranek and K. Wippermann, *Journal of Electroanalytical Chemistry*, **567**, 305 (2004).
87. J. K. Lee, W. Li and A. Manthiram, *Journal of Power Sources*, **180**, 56 (2008).
88. S. M. J. Zaidi, S. D. Mikhailenko, G. P. Robertson, M. D. Guiver and S. Kaliaguine, *Journal of Membrane Science*, **173**, 17 (2000).
89. C. Hasiotis, V. Deimede and C. Kontoyannis, *Electrochimica Acta*, **46**, 2401 (2001).
90. L. Zhang, C. Hampel and S. Mukerjee, *Journal of The Electrochemical Society*, **152**, A1208 (2005).
91. A. Parthasarathy, C. R. Martin and S. Srinivasan, *Journal of The Electrochemical Society*, **138**, 916 (1991).
92. A. Parthasarathy, B. Dave, S. Srinivasan, A. J. Appleby and C. R. Martin, *Journal of The Electrochemical Society*, **139**, 1634 (1992).
93. F. N. Buchi, M. Wakizoe and S. Srinivasan, *Journal of The Electrochemical Society*, **143**, 927 (1996).
94. P. D. Beattie, V. I. Basura and S. Holdcroft, *Journal of Electroanalytical Chemistry*, **468**, 180 (1999).
95. V. I. Basura, C. Chuy, P. D. Beattie and S. Holdcroft, *Journal of Electroanalytical Chemistry*, **501**, 77 (2001).
96. L. Zhang, C. Ma and S. Mukerjee, *Journal of Electroanalytical Chemistry*, **568**, 273 (2004).

97. S. Mitsushima, N. Araki, N. Kamiya and K. i. Ota, *Journal of The Electrochemical Society*, **149**, A1370 (2002).
98. K. Lee, A. Ishihara, S. Mitsushima, N. Kamiya and K.-i. Ota, *Journal of The Electrochemical Society*, **151**, A639 (2004).
99. K. Ota, Y. Inoue, N. Motohira and N. Kamiya, *Journal of New Materials for Electrochemical Systems*, **3**, 193 (2000).
100. M. Rodgers, *An Investigation of Structure-property Relationships in Several Categories of Proton Exchange Membranes*, Simon Fraser University, Burnaby (2007).
101. U. Kohei, O. Kentaro and K. Hideaki, *Journal of Electroanalytical Chemistry*, **287**, 163 (1990).
102. P. D. Beattie, F. P. Orfino, V. I. Basura, K. Zychowska, J. Ding, C. Chuy, J. Schmeisser and S. Holdcroft, *Journal of Electroanalytical Chemistry*, **503**, 45 (2001).
103. J. Giner, *Journal of The Electrochemical Society*, **111**, 376 (1964).
104. S. Mikhailenko, M. Zaidi and S. Kaliaguine, *Catalysis Today*, **67**, 225 (2001).
105. T. Kobayashi, M. Rikukawa, K. Sanui and N. Ogata, *Solid State Ionics*, **106**, 219 (1998).
106. P. Xing, G. P. Robertson, M. D. Guiver, S. D. Mikhailenko, K. Wang and S. Kaliaguine, *Journal of Membrane Science*, **229**, 95 (2004).
107. P. C. Lee and M. A. J. Rodgers, *Journal of Physical Chemistry* **88**, 4385 (1984).
108. D. R. Lawson, L. D. Whiteley, C. R. Martin, M. N. Szentirmay and J. I. Song, *Journal of The Electrochemical Society*, **135**, 2247 (1988).
109. A. Damjanovic and M. A. Genshaw, *Electrochimica Acta*, **15**, 1281 (1970).
110. M. Uchida, Y. Aoyama, N. Eda and A. Ohta, *Journal of The Electrochemical Society*, **142**, 463 (1995).
111. J. Fournier, G. Faubert, J. Y. Tilquin, R. Cote, D. Guay and J. P. Dodelet, *Journal of The Electrochemical Society*, **144**, 145 (1997).
112. L. Giorgi, E. Antolini, A. Pozio and E. Passalacqua, *Electrochimica Acta*, **43**, 3675 (1998).
113. V. A. Paganin, E. A. Ticianelli and E. R. Gonzalez, *Journal of Applied Electrochemistry*, **26**, 297 (1996).
114. S. J. Lee, S. Mukerjee, J. McBreen, Y. W. Rho, Y. T. Kho and T. H. Lee, *Electrochimica Acta*, **43**, 3693 (1998).
115. Z. Poltarzewski, P. Staiti, V. Alderucci, W. Wieczorek and N. Giordano, *Journal of The Electrochemical Society*, **139**, 761 (1992).

116. Z. Xie, T. Navessin, K. Shi, R. Chow, Q. Wang, D. Song, B. Andraus, M. Eikerling, Z. Liu and S. Holdcroft, *Journal of The Electrochemical Society*, **152**, A1171 (2005).
117. M. Watanabe, M. Tomikawa and S. Motoo, *Journal of Electroanalytical Chemistry*, **195**, 81 (1985).
118. M. Watanabe, K. Makita, H. Usami and S. Motoo, *Journal of Electroanalytical Chemistry*, **197**, 195 (1986).
119. K. R. Cooper and M. Smith, *Journal of Power Sources*, **160**, 1088 (2006).
120. H. Xu, E. L. Brosha, F. H. Garzon, F. Uribe, M. Wilson and B. Pivovar, *ECS Transactions*, **11**, 383 (2007).
121. S. Gottesfeld, I. D. Raistrick and S. Srinivasan, *Journal of The Electrochemical Society*, **134**, 1455 (1987).
122. T. J. Schmidt, H. A. Gasteiger and R. J. Behm, *Journal of The Electrochemical Society*, **146**, 1296 (1999).
123. M. C. Lefebvre, R. B. Martin and P. G. Pickup, *Electrochemical and Solid-State Letters*, **2**, 259 (1999).
124. T. E. Springer, M. S. Wilson and S. Gottesfeld, *Journal of The Electrochemical Society*, **140**, 3513 (1993).
125. R. Makharia, M. F. Mathias and D. R. Baker, *Journal of The Electrochemical Society*, **152**, A970 (2005).